MASTERARBEIT / MASTER’S THESIS

Titel der Masterarbeit / Title of the Master’s Thesis

"The evolution of atomically-cooled primordial haloes"

verfasst von / submitted by
Anna Schrenk, BSc

angestrebter akademischer Grad / in partial fulfillment of the requirements for the degree of
Master of Science (MSc)

Wien 2022 / Vienna, 2022

Studienkennzahl lt. Studienblatt / degree programme code as it appears on the student record sheet:	UA 066 861
Studienrichtung lt. Studienblatt / degree programme as it appears on the student record sheet:	Masterstudium Astronomie
Betreut von / Supervisor:	Univ.-Prof. Dipl.-Phys. Dr. Bodo Ziegler
Mitbetreut von / Co-Supervisor:	

Acknowledgements

First and foremost, I would like to thank Daniel Whalen for his supervision and for sharing his extensive knowledge. He patiently took on the task of remote supervision, in itself a challenging task and made infinitely more difficult during a worldwide pandemic, successfully guiding me through the struggles of writing a thesis.

Many thanks go to Sam Patrick, who provided the initial data set that stands as the ground pillar of this thesis and who offered invaluable insight into cosmological simulations with their data processing.

I would also like to extend my deepest gratitude to Bodo Ziegler, who managed to build a nurturing environment that offered insight into research and a place for open scientific discussion.

Chris Jessop was my knight in shining armor, a hero without a cape, who deserves only the highest praise. He did not hesitate to offer advice and help when needed, while at the same time soothing my frayed mind when I was doubting my own sanity.

Special thanks go to the Sciama HPC support team and especially to Toby Maule, who answered all my questions with infinite patience and lightning speed.

This thesis would not have been possible without the support and love of two amazing women: Carina Heinreichsberger and Arijane Sommeregger. Our weekly mental health breakfasts/brunches always gave me enough fuel to power through yet another week. It was reassuring to connect on so many fronts, experiencing the same fears and struggles and to know that I was not alone in them.

Another incredible woman I want to thank is Martina Koppitz, who understood me like no other when it came to the perversity of inanimate objects - Sciama - and who regularly offered different vantage points.

I would further like to extend my gratitude to all my friends "from the field", we pushed through together to get this far and we will make it even further. Thank you for having the guts to ask the uncomfortable questions, namely "How is your thesis going?" and for motivating me by insinuating a guilty conscience. A shout out goes to all my other friends, who had the misfortune of spending time with my stressed out self and who were able to bear it gracefully.

Words are not able to describe how wholeheartedly grateful I am to my family for their profound belief in my abilities and for always having my back.

Numerical computations were done on the Sciama High Performance Compute (HPC) cluster which is supported by the ICG, SEPNet and the University of Portsmouth.

Computations described in this work were performed using the publicly-available `Enzo` code[1],

---

[1] http://enzo-project.org

which is the product of a collaborative effort of many independent scientists from numerous institutions around the world. Their commitment to open science has helped make this work possible. (Bryan et al. (2014))
Analysis has been realized with `yt` [2]. Thank you for being this useful! (Turk et al. (2011))

---

[2] https://yt-project.org

Abstract

Seeds for the first super-massive quasars in our Universe are thought to have formed in atomically-cooled haloes subjected to immense Lyman Werner (LW) UV backgrounds, as they are able to form objects high enough in mass by suppressing star formation and fragmentation in their centers until reaching the super-massive regimes. Such unusually high LW backgrounds are needed to completely destroy H_2 and therefore prevent the fragmentation and formation of smaller structures. However, such exotic conditions would have been very rare in the early Universe. Therefore, this thesis aims to study the evolution of atomically-cooled haloes immersed in a $10^5 J_{21}$ LW background with enabled H_2 self-shielding, as intermediate LW backgrounds that allow H_2 to survive in halo centers would have been more common in the early Universe.

We perform cosmological zoom-in simulations with the grid-based hybrid adaptive mesh refinement code `Enzo` (Bryan et al. (2014)) on the high-performance computing cluster `SCIAMA` at the ICG Portsmouth, UK. Initial conditions are generated by `MUSIC` (Hahn and Abel (2011)) and are laying the base on which subsequently eight designated haloes are evolved from z = 200 until 2 - 5 Myr after their catastrophic baryon collapse. A top grid resolution of 256^3 is enforced, with three additional nested grids (256^3 each) on a target halo, for 15 levels of refinement. H_2 self-shielding is calculated with the Sobolev-like approximation from (Wolcott-Green et al. (2011)). Data is then processed using the community developed, open source code `yt` Turk et al. (2011).

We find that H_2 is able to self-shield against the highest LW backgrounds, surviving in halo centers. There it surrounds a hot central core that is cooled through Lyα, while itself being embedded in a hot, atomically-cooled medium. Accretion rates are somewhat lower than for pristine Lyα cooled haloes, having average values of 0.026 - 0.1 $\mathrm{M}_{\odot} yr^{-1}$ with peaks of up to 1.78 $\mathrm{M}_{\odot} yr^{-1}$. The total accumulated masses inside the 0.136 pc tally sphere lie between 0.5 - 3 $\times 10^5 \mathrm{M}_{\odot}$, leading to the formation of two types of stars with masses between $10^3 - 10^5$ $\mathrm{M}_{\odot}$, either compact, blue supergiants or cool, red super-massive stars. Depending on the specific accretion history, they might not be the progenitors of the most massive quasars at z > 7, yet potentially present a new population of intermediate mass black holes.

Kurzfassung

Die Entdeckung supermassereicher Quasare bei einer Rotverschiebungen von z > 7 (Mortlock et al. (2011); Bañados et al. (2018); Matsuoka et al. (2019); Yang et al. (2020); Wang et al. (2021)), stellt einige Fragen in Bezug zu ihrer Entwicklung auf. Ein mögliches Entstehungs Scenario sind durch atomaren Wasserstoff gekühlte Haloes die einer hohen Lyman Werner (LW) UV Strahlung ausgesetzt sind. Derartige Bedingungen unterdrücken die Bildung von kleineren Strukturen, unter anderem Sterne, bis die Haloes genug Masse aufbauen können um supermassereiche Objekte zu formen in dem sie molekularen Wasserstoff H_2 komplett unterdrücken bzw zerstören. Diese exotischen Bedingungen waren im frühen Universum jedoch wahrscheinlich sehr selten. Daher hat diese Masterarbeit das Ziel, die Entwicklung von atomar gekühlten Halos die einer LW Hintergrundstrahlung von $10^5 J_{21}$ ausgesetzt sind, zu untersuchen. Des Weiteren, wird H_2-Selbstabschirmung mit hinzugenommen um realistischere Ergebnisse zu erzielen.

Wir führen kosmologische Zoom-in-Simulationen mit dem gitterbasierten hybrid adaptiven Netz-Verfeinerungscode (AMR) `Enzo` (Bryan et al. (2014)) auf dem High-Performance-Computing-Cluster `SCIAMA` am ICG Portsmouth, UK durch. Anfangsbedingungen werden von `MUSIC` (Hahn and Abel (2011)) bestimmt. Anschließend werden acht Halos von z = 200 bis 2 - 5 Millionen Jahre nach ihrem katastrophalen Baryonenkollaps entwickelt. Für 15 Verfeinerungsstufen wird eine maximale Rasterauflösung (grid resolution) von 256^3 eingesetzt, mit drei zusätzlich Überlagerten nested grids (je 256^3) auf einem Ziel-Halo. H_2 Selbstabschirmung wird mit der Sobolev-ähnlichen Näherung aus (Wolcott-Green et al. (2011)) berechnet. Simulationsdaten werden dann mit dem Open-Source-Code `yt` Turk et al. (2011) visualiziert und erforscht.

Unsere Ergebnisse zeigen, das H_2 bei genügend großen Dichten in der Lage ist, sich selbst vor sogar extremer LW Strahlung zu schützen und in Halo Zentren zu überleben. Dort umgibt das H_2-reiche Gas einen heißen zentralen Kern, der durch Lyα gekühlt wird, während es selbst in ein heißes, atomar gekühltes Medium eingebettet ist. Die von uns berechneten Akkretionsraten sind etwas geringer als bei rein Lyα-gekühlten Halos, mit Durchschnittswerten von 0.026 - 0.1 $\mathrm{M}_\odot yr^{-1}$ und Maxima von bis zu 1.78 $\mathrm{M}_\odot yr^{-1}$. Die insgesammt hierbei akkumulierten Massen innerhalb der approximierten 0.136pc Kugel liegen zwischen 0.5 - 3 $\times 10^5$ $\mathrm{M}_\odot$, was zur Bildung von zwei Arten von Sternen mit Massen zwischen $10^3 - 10^5$ $\mathrm{M}_\odot$ führt. Zum einen sind das kompakte, blaue massive Sterne und zum anderen rote, kalte supermassereiche Sterne. In Abhängigkeit von der spezifischen Akkretionsgeschichte sind sie wahrscheinlich nicht die Vorläufer der super-massiven Quasare mit $10^9 \mathrm{M}_\odot$ bei z > 7, stellen jedoch möglicherweise eine neue Population von schwarzen Löchern mittlerer Masse dar.

Contents

Table of Abbreviations

Abbreviation	*Definition*	*Abbreviation*	*Definition*
e^-	Electron	$h\nu$	Photon
m_p	Proton mass	μ	Mean molecular weight
G	Gravitational constant	k_B	Boltzmann constant
H	Atomic hydrogen	H_2	Molecular hydrogen
N_{H2}	H_2 column density	eV	Electron Volt $\simeq 1.6 \times 10^{-19} J$
M$_\odot$	Solar mass $1.98847 \times 10^{30} kg$	$R_\odot$	Solar radius $6.96342 \times 10^8 m$
pc	Parsec = $3.09 \times 10^{16} m$	AU	Astronomical Unit $\simeq 1.496 \times 10^{11} m$
BB	Big Bang	z	Redshift
CMB	Cosmic Microwave Background	Pop I, II, III	Population I, II, III
DM	Dark Matter	ΛCDM	Λ Cold Dark Matter
SF	Star Formation	ISM	Inter Stellar Medium
M_J	Jeans-mass	λ_J	Jeans-length
VMS	Very Massive Star	SMS	Super Massive Star
SN	Super Nova	SED	Spectral Energy Distribution
LW	Lyman- Werner	J_{21}	$10^{-21} ergs^{-1} cm^{-2} Hz^{-1} sr^{-1}$
J_{crit}	Critical LW flux	f_{esc}	LW photon escape fraction
f_{sh}	Self-shielding factor	UV	Ultra Violet
BH	Black Hole	IMBH	Intermediate Mass Black Hole
SMBH	Super Massive Black Hole	DCBH	Direct Collapse Black Hole
GR	General Relativistic	AMR	Adaptive Mesh Refinement
HPC	High-performance computing	MPI	Message-passing interface
HD	Hydrodynamic	MHD	Magnetohydrodynamic
EOS	Equation of state	PPM	Piecewise parabolic method
HLL	Haarten-Lax-van Leer	HLLC	HLL with contact discontinuity
HLLD	HLL with multiple discontinuities	LLF	Local Lax-Friedrichs
CIC	Cloud-in-cell	LPT1	First-order Lagrangian perturbation theory
LPT2	Second-order Lagrangian perturbation theory	FFT	Fast Fourier Transform
GW	Gravitational wave	TDE	Tidal disruption event
NIR	Near infrared	JWST	James Webb Space Telescope
ELT	Extremely- large Telescope	RST	Roman Space Telescope
LISA	Laser Interferometry Space Antenna		

Chapter 1

Introduction

Over 200 quasars have been discovered at redshifts $z > 6$, with nine at $z > 7$ (Mortlock et al. 2011; Bañados et al. 2018; Matsuoka et al. 2019; Yang et al. 2020; Wang et al. 2021), when the Universe was ~ 800 Myr old. How 10^9 $\mathrm{M}_\odot$ supermassive black holes (SMBHs) appeared by $z > 6$ remains one of the outstanding problems in astronomy. Three main channels have been proposed for their formation. The first is Population III (Pop III) stars with masses of a few tens to hundreds of $\mathrm{M}_\odot$, which were fairly common in the early universe. More massive Pop III stars that grew to a few thousand $\mathrm{M}_\odot$ via runaway collisions in dense nuclear clusters are the second proposed path. The leading contenders, however, are supermassive stars (SMSs) forming in atomically cooled primordial haloes at high redshifts, $z \sim 15-20$. Those halos would have been exposed to either unusually strong Lyman-Werner (LW) UV fluxes or highly supersonic baryon streaming motions that prevented star formation (SF) in them until they grew to $\sim 10^7$ $\mathrm{M}_\odot$ and reached virial temperatures of $\sim 10^4 K$. This led to the formation of cool, red SMSs that later collapsed to $100,000-250,000$ $\mathrm{M}_\odot$ BHs (direct collapse BHs, or DCBHs) (Hosokawa et al. (2013); Umeda et al. (2016); Woods et al. (2017); Haemmerlé et al. (2018); Woods et al. (2021); Herrington et al. (2022)).

Latif et al. (2022) recently found that 40,000 $\mathrm{M}_\odot$ seeds for SMBHs form in primordial halos at the intersection of turbulent cold accretion flows without any need for streaming motions or LW radiation. Supersonic turbulence driven by the flows prevents star formation in the halo until it reaches high enough masses to trigger catastrophic baryon collapse and form SMSs, which later collapse to DCBHs. Thereby lifting the weight from atomically cooling haloes as a means for SMBH formation and letting it stand on its own scientific feet. And standing it does, although often times called exotic, it pushes the understanding of the primordial Universe forward while revealing processes otherwise hidden.

Numerical simulation of collapse in atomically-cooled haloes have come a long way. Initially they were relying on idealized conditions or semi-analytic calculations and are currently balancing between the best resolution and time ratio. More often than not, due to limited computational power and storage, one has to decide between in depth studies or the evolutional time-steps of an object. The starting point is usually defined by cosmological initial conditions. Simulations then either follow the forming protostar without the accretion disk on parsec scales or the other way around, growing the accretion disk for a few dynamical times, yet not capturing the forming star in its core (e.g., Wise et al. (2008); Regan and Haehnelt (2009a,b)). However, it was later found that high infall rates could reach down to star-like sizes. Precise results were though missing as the simulations did not evolve the objects for long enough times (Latif et al. (2013a); Regan et al. (2014)). Follow up high resolution simulations revealed that this was indeed true. Large accretion rates were able to sustain to very small sizes and survive for a few tens of kyr. Those simulations additionally made use of sink particles and pressure floors (Latif et al. (2013b); Regan and Downes (2018b)). Subsequently Chon et al. (2018) and Regan and Downes (2018b) studied the centers of atomically-cooled haloes with implemented radiative feedback and simple evolution from the forming star. Following the progress for 100kyr and 250kyr, they found that accretion on to the star was not hampered by radiation. Furthermore it was discovered that gas on AU scales in the halo core was susceptive to fragmentation, potentially allowing the formation of multiple SMSs. Yet, again the studies failed to evolve the haloes for long enough to determine whether multiple stars were able to form or not due to the clumps merging with the central object. High resolution studies on scales of $\sim 0.1pc$ from Suazo et al. (2019) were able to follow the central object until a DCBH would form, coming also close to determining masses of those SMSs. Trading high resolution for longer evolution times paid in this case off. Latif and Khochfar (2020); Regan et al. (2020b) and Patrick et al. (2020) examined the infall rates and evolution of gas in the halo center for million of years until a DCBH would have been able to form. They were able to determine masses and infall rates for potential SMSs. In particular Latif and Khochfar (2020) observed that an accretion disk can fragment into binaries and clusters of SMSs in the pc range. The caveat being, that they investigated only a small number of haloes on the upper and lower limit of spin parameters. Patrick et al. (2020) focused on determining the impact of halo formation history and spin parameter on SMS masses and number, finding that SMSs did form in binaries or small cluster systems in atomically-cooled haloes. Room for improvement was left, as they modeled the upper LW background limit without any H_2 and purely isothermal collapse.

However, implementing H_2 into simulations can yield some difficulties. J_{crit} itself, the flux necessary to completely suppress H_2 star formation, is a difficult to determine value. LW photons reside in 78 lines between 11.18-13.6 eV, which can be shifted into and out of line center due to turbulent motions of the gas. Calculations of line transport with Lorentz boosts have to be carried out in order to attain realistic results of H_2 photo-dissociation rates and account for Doppler shifts (Ricotti et al. (2001)). Additionally the escape fractions of LW photons f_{esc} from their parent haloes have to be determined (Schauer et al. (2015, 2017)) . Both are not easy feats especially in cosmological simulations. The go-to solution is to implement a uniform LW background as has been done by e.g.,Machacek et al. (2001); Yoshida et al. (2003); O'Shea and Norman (2007). For more realistic results self-shielding of H_2 inside haloes against outside radiation is calculated with semi-analytic functions, which has been done by e.g.Draine and Bertoldi (1996); Shang et al. (2010); Wolcott-Green et al. (2011, 2021). Another tool comes in the form of the TREECOL algorithm (Clark et al. (2012)) that determines through the calculation of Doppler shifted lines from velocity gradients the column densities of 3D simulations. Those revealed that self-shielding is underestimated by a factor of two in cases of Jeans approximations, as there is a strong dependence on the direction in which the H_2 column density is measured, which is impossible to determine with a simple 1D approach (Hartwig et al. (2015)). Hartwig et al. (2015) furthermore found, that with their higher self-shielding the number density of DCBHs in the early Universe increases by a factor of 32. Still, even this higher number density does not account for the vast number of SMBHs at $z < 6$ considering solely the isothermal direct collapse scenario.

As an effective source of LW radiation for quenching later Pop III star formation, the first semi-analytic studies deemed the first generation of stars adequate. They are able to produce modest LW backgrounds of $J_{crit} \sim 1J_{21}$ (Haiman et al. (1997, 2000); Glover and Brand (2001)). However, subsequent studies revealed that their effect can be diminished by turbulence as it moves fluid elements away from the line center (Ripamonti and Abel (2004)). Further on, an increased value of $J_{crit} \gtrsim 10J_{21}$ was found by Wise and Abel (2007). Collisional ionization caused by mergers with other haloes could increase the number of free electrons and thus boost the formation of H_2 through H^-. In return this would raise the value of J_{crit} required to supress H_2 star formation. Sources of UV radiation could increase local LW fluctuations to $J_{crit} > 10^4 J_{21}$, as has been found in simulations of Agarwal et al. (2012), indicating that the formation of primordial haloes as progenitors of DCBHs is possible. Additionally, they highlighted how Pop III stars would have been unable to generate the necessary flux. This is due to their limited number and lifetime. Most of the flux is therefore believed to come form Pop II stars, in a sufficient distance to the designated halo. Distance is needed as to not ionize the halo and evaporate it before it even has the chance to start atomic cooling. (Johnson et al. (2014); Regan et al. (2017))
Therefore, the value of J_{crit} was in most studies based on simple blackbody spectra of Pop III or Pop II stars. Temperatures of the second generation of stars Pop II are believed to be of order $10^4 - 10^5 K$ (Schaerer (2003); Leitherer et al. (1999)), hence assuming the blackbody temperature T_{bb} as $T_{bb} = 10^5 K$ or $10^4 K$. However, for a more realistic approach spectral energy distributions (SED) have to be taken into account as J_{crit} varies depending on their shape. A softer SED will lead to a lower J_{crit} by two orders of magnitude than a harder shape. The softer SED is mainly driven by the suppression of H_2 through photo-detachment of H^-, whereas its counterpart the hard SED is dominated by direct dissociation of H_2 (see equation 2.14 and 2.13) (Omukai (2001); Shang et al. (2010); Johnson et al. (2013a); Latif et al. (2014a)). Estimating J_{crit} based on 3D simulations using realistic SEDs yields $20,000 - 50,000 J_{21}$, which is one order of magnitude larger than values of J_{crit} based on one-zone models. Extensive studies additionally showed that the critical LW flux can be correctly calculated based on the ratio of the disscociation rates of H^- to H_2, with $T_{bb} = 10^4 - 10^5 K$, as J_{crit} only marginally depends on the specifics of star formation, including age, metallicity and bursty or continuous formation mode. Those studies utilized the stellar synthesis code *STARBURST99* from Leitherer et al. (1999) for their SED calculations. (Sugimura et al. (2014); Agarwal et al. (2016); Latif et al. (2015); Patrick et al. (2021))

This thesis aims to investigate the initially deemed most probable formation path for SMBH, atomically cooled haloes. Detailed descriptions of the respective formation paths are going to be outlined below. Chapter 2.1 will delve into the formation of the first objects in the early universe. Subsequently followed by runaway stellar collisions in chapter 2.2. Atomically cooled haloes will be described in chapter 2.3 and chapter 2.3.1 will showcase LW radiation and inlying H_2 self-shielding. This will be followed with a detailed numerical description of the used methods in chapter 3. Chapter 4 presents the results of the study and is concluded in chapter 5.

Chapter 2

The Early Universe

2.1 First Stars and Population III Black Holes

Before discussing the formation of the first stars, Pop III, a theoretical framework has to be established pertaining the evolution of our Universe, starting with the Big Bang (BB). In this case the framework is defined through the standard cosmological model, the Λ cold dark matter (CDM) scenario, in which the Universe underwent hierarchical structure formation and consists today roughly of 68% Dark Energy, 27% Dark Matter and 5% ordinary Matter. The cosmology therein can be described through six independent parameters. Those parameters are fitted to correspond to observational results regarding the anisotropies of the Cosmic Microwave Background (CMB), the expanding Super Novae (SN) Type Ia light curves and large-scale structures to name a few. This framework makes it possible to describe the early stages of our Universe, when our technology does not yet suffice to explore those parts and possibly never will.

2.1.1 Initial conditions

The infant stage of the Universe is thought to be a time of an extremely hot, dense, nearly homogeneous photon-matter plasma. An epoch of accelerated expansion - cosmic inflation - increases the size of the Universe exponentially. At this time, vacuum quantum fluctuations give rise to primordial density fluctuations that are still imprinted on the CMB. Cosmic inflation stops once the size of the Universe increased by order 10^{40}. Remaining energy, that before drove the inflation, is now poured into reheating the Universe and expansion progresses at a slower pace. This environment allows for the pair production and annihilation[3] of proton and antiprotons, neutrons - antineutrons and electrons and positrons. Formation of subatomic particles continues until the Universe cools down to 1 trillion Kelvin, with the exception of electrons that are less massive and are able to form down to cooler temperatures. Shortly thereafter with temperatures of $\sim 10^9$K, first nuclei are able to form in the Big Bang Nucleosynthesis as the probability of destruction by photons decreases significantly. Deuterium, Helium, Lithium and Beryllium start to form approximately three minutes after the Big Bang, culminating in a ratio of $\sim 75\%$ Hydrogen and $\sim 25\%$ Helium. The BB Nucleosynthesis stops after roughly 30 minutes due to

---

[3] a particle-antiparticle pair collides to form a pair of photons

a temperature smaller than 10^8K and a hence decreased reaction rate. At this point, matter is completely ionized, leaving electrons unbound. Photons scatter on those free electrons and cannot travel through the surrounding ionized gas. This picture changes 380000yr after the BB once the Universe is able to cool further down to $\sim$ 3000K, this process is also known as *Recombination*. Electrons bind themselves to nuclei forming neutral atoms and leaving room for photons to travel unscattered. Photons and baryons are furthermore no longer strongly coupled. Thomson scattering is able to slightly delay Recombination. Looking back through time we describe this period as the Dark Ages, as no stars have been formed yet, implying that the only light is emitted by hydrogen through radio waves. Only at $z \sim 6 - 20$ the first stars rise to reionize the Universe again. (Loeb (2006); Weigert et al. (2010))

2.1.2 Density contrast

The conditions for a star to form, however, are established long before recombination. They require slight fluctuations in the matter distribution, which thankfully our Universe fulfills. Already the young Universe, at 380000yr after the BB, shows anisotropies. Those anisotropies stem from primordial quantum fluctuations that are depicted to this day on the power spectrum of the 2.7K CMB. Photons, able to travel mostly unscattered due to recombination, carry that information back to us.

Those small inhomogenities are directly tied to the gravitational field and baryon density of that time. The gravitational field was dominated by non-baryonic matter, dark matter (DM). Dark matter has the characteristics of being unaffected by radiation and is therefore able to assemble way before normal baryonic matter, forming dark matter potential wells. Those accumulations act as attractive gravitational fields into which normal matter later on collapses. Baryons are able to collapse once photon pressure falls away after recombination. Before that, they are subjected to repulsive forces of photon pressure working against gravity trying to pull them into potential wells. This is due to the phenomenon that increasing the density leads to increased pressure.

Photons, while escaping those potential wells have to work against gravity. This results in a shift in frequency which is correlated to a shift in temperature visible in the CMB. Applying this to the grand scheme of the Universe leads to the freckled picture we have of the CMB. Regions of high density, where the potential wells are located, imprint as cold spots and regions of lower densities show as warm spots on the CMB map. Initially the discrepancies are only of order $\Delta T/T \sim 10^{-5}$, however, grow with cosmic expansion. They can be described with the density contrast δ ,

$$\delta := \frac{\rho - \bar{\rho}}{\bar{\rho}}, \tag{2.1}$$

where $\bar{\rho}$ denotes the average cosmic matter density. A region of average density will yield $\delta = 0$ whereas an overdensity region requires $\delta > 0$ and an underdensity $\delta < 0$. In the early Universe the density contrast must have been $|\delta| \ll 1$ and only after recombination the density contrast of baryonic matter was high enough to form structures. With time density fluctuations grow due to their self-gravity, proceeding in this manner as long as the self-gravity remains small. Expansion is able to extend those regions until an overdensity reaches $\delta > 1$, where the local gravitational field is able to overpower it. It slows the pace of the expansion or even reverses its effect by triggering gravitational collapse. Gravitational collapse is triggered when an overdensity region accumulates enough mass so that its self-gravity is able to defeat the pressure forces working against it. After recombination that pressure arises from high densities originating in infalling gas. The first objects are believed to have formed in overdense environments and its resulting instabilities. Those can be approximated through the Jeans-criterion, which is going to be described below. (Weigert et al. (2010); Schneider (2006))

2.1.3 Gravitational collapse and cooling

Initial density perturbations will grow linearly until they reach high enough masses for self-gravity to trigger gravitational collapse. Those dark matter accumulations will be bound together by gravity to form the first haloes. They continue to grow by accreting mass and/or merging with other haloes, as the ΛCDM model favors a bottom up structure formation.
Aforementioned, baryonic matter will be attracted to those structures and settle into them. Dark matter then helps to overcome thermal and radiative pressure forces working against a collapse and allowing for the first stars to form. J.Jeans deduced from this the *Jeans criterion* and with it the Jeans-length λ_J

$$\lambda_J = \sqrt{\frac{\pi k_B T}{G \rho \mu m_P}} \tag{2.2}$$

and Jeans-massM_J

$$M_J = \frac{\pi}{6} \rho \lambda_J^3, \tag{2.3}$$

where T is the temperature of the gas cloud, ρ its baryonic density, k_B the Boltzman constant, G the gravitational constant, μ the mean molecular weight and m_p the proton mass.
They define a critical mass and length that when it is reached will trigger runaway contractions. A primordial gas cloud is in this picture assumed as spherical, homogenous, isothermal and non-rotating. In addition to the gravitational collapse, gas has to get rid of its kinetic energy and cool to be able to form stars, as infalling gas will be shock heated. (Weigert et al. (2010))

How does one get rid of kinetic energy and cool to form objects? The early Universe had not much going on in regards of cooling agents, lacking the metals we find in the solar environment today and no dust grains to act as catalysts for molecular formation. Various cooling processes surrounding the primordial chemical composition operate at different temperatures and densities. The main cooling processes are collisional in nature, acting between the gas particles and depending thus on the density squared. Although compression of the gas raises pressure forces it likewise increases the efficiency of cooling. Kinetic energy of a gas can then be radiated away while the potential energy grows, enabling runaway collapse that is only stopped once infalling matter gets to dense and cold. Initially Pop III stars were believed to be very massive, as H_2 chemistry was not well understood leaving atomic hydrogen as the main coolant. This would lead to an adiabatic heat up of the collapsing gas cloud as H is a very inefficient radiator and operates at higher temperatures. Such a gas cloud would increase its temperature until it triggers at $\sim 10^4$K Lyα cooling through collisional ionization. The resulting high Jeans-Mass M_J lead to the question of how stellar like structures could fragment in such an environment. A solution presented itself through H_2 chemistry which was first pointed out by McDowell (1961). He found that at densities present in H clouds the important processes for molecular hydrogen formation will be the *radiative attachment*

$$H + e^- \rightarrow H^- + h\nu \tag{2.4}$$

and the *associative detachment*

$$H^- + H \rightarrow H_2 + e^-, \tag{2.5}$$

where electrons e^- as leftover from Recombination, work as catalyst. The slow process of radiative attachment and the rapid process of associative detachment in equation 2.4 and 2.5 are the main reactions responsible for forming H_2. Further, the formation channel through *radiative association*

$$H + H^+ \rightarrow H_2^+ + h\nu \tag{2.6}$$

subsequently followed by *charge transfer*

$$H_2^+ + H \rightarrow H_2 + H^+ \tag{2.7}$$

contributes to the increase in H_2, although only slightly. In sufficiently high gas densities $\gtrsim 10^8 cm^{-3}$, H_2 can be additionally formed through three-body reactions

$$H + H + H \rightarrow H_2 + H, \tag{2.8}$$

$$H + H + H_2 \rightarrow H_2 + H_2. \tag{2.9}$$

Even a small fraction of H_2 allows substantial cooling through the molecules collisionally excited rotational and vibrational transitions. Therefore cooling is triggered when the temperature in the center rises to 1000K, working through the channels of photo-dissocitation of hydrogen molecules and progressing until no H_2 is left. It leaves the gas at temperatures of $\sim 100 - 200$K and densities of $\sim 10^3 - 10^4 cm^{-3}$, allowing for stellar like structures to evolve. Nonetheless, they are believed to be more massive than Pop I or Pop II stars as H_2 is, compared to metals, a rather poor coolant. If the gas, however, is able to get to temperatures of 10^4K without enabling photodissociation of H_2, it cools through the earlier mentioned collisional excitation of atomic hydrogen H and emits a Lyα-photon. At 10^5K singly ionized Helium (He) is responsible for cooling and at higher temperatures Bremsstrahlung takes over the role of main coolant. (Agarwal (2018))

Once this protostellar clump collapses it further contracts to a protostar. A protostar is a compressed fragment in hydrostatic equilibirum in its center and outer collapsing regions. It continues to accrete matter and looses excessive kinetic energy through radiation. The central part increases its potential energy and by doing so heats up. Central temperatures keep building until thermonuclear fusion is ignited, denoting the birth of a star. (Weigert et al. (2010); Latif et al. (2014b); Bromm et al. (2002); Whalen et al. (2008, 2010))

2.1.4 Population III Black Holes

H_2 is, as established above compared to the metals we find in the interstellar medium (ISM) today, a very inefficient coolant leading to the first stars to be more massive. They had surface temperatures of $\sim 10^5$K and radii $\sim$ six times greater than the radius of the sun, rendering them the perfect candidates for reionizing the universe. Pop III stars lived for a few million years ending their life in different scenarios depending on their mass. Masses of $\gtrsim 20$ M$_\odot$ will trigger a complete gravitational collapse into a BH, a core-collapse SN with BHs, or neutron stars. Even if the final fate of Pop III stars are neutron stars, they can still eventually become BHs due to merger and accretion of such objects. BHs produced in those scenarios will end up having masses of $\sim 10 - 1000$ M$_\odot$, continuing their growth as long as they have enough fuel by accreting surrounding matter. (Loeb (2010a,b); Mo et al. (2010a,b))

Approximation of Black Hole growth

For Black holes to grow in mass by accreting surrounding gas, the gravitational force $F_{grav} \simeq (GMm_p)/(r^2)$ has to maintain dominance over the repulsing radiative force $F_{rad} = (L\sigma_T)/(4\pi r^2 c)$. Following this condition and equating $F_{grav} = F_{rad}$, the Eddington-Luminosity L_{edd} can be introduced as

$$L_{edd} = \frac{4\pi G c m_p}{\sigma_T} M_\bullet, \tag{2.10}$$

where $M_\bullet$ is the BH mass, σ_T the electron Thomson cross-section, L the luminosity, G the gravitational constant, m_p mass of a proton, and c the speed of light. Accretion is only possible for a luminosity L of $L < L_{edd}$ and L_{edd} is proportional to the BH mass. Conversion of infalling matter into energy happens with an efficiency ϵ that ultimately determines the on L dependent accretion rate $\dot{M}$ as

$$\dot{M} = \frac{L}{\epsilon c^2}. \tag{2.11}$$

Meassuring it in terms of the Eddington-Luminosity yields the Eddington-Accretionrate $\dot{M}_{edd}$

$$\dot{M}_{edd} = \frac{L_{edd}}{\epsilon c^2}. \tag{2.12}$$

The Eddington-Accretionrate, although an approximation using isotropic emission and spherical symmetry, sets a robust limit for the upper accretion limit of a BH. Another caveat is the absence of angular momentum and accretion disk in the calculation.

2.1.5 Population III Black Holes as progenitors of Supermassive Black Holes?

Black holes formed by typical Population III stars, with masses of $\sim 10 - 1000$ M$_\odot$, could not have maintained the high accretion rates that are required for growing to masses of $M \sim 10^9$ M$_\odot$ by $z > 7$. Estimations using the Eddington-limit accretion show that typical Pop III black holes would need an accretion time that exceeds the age of the Universe. Accretion at super-Eddington rates may solve that problem, however, only small episodes were found. Additionally to not being massive enough from the start, normal Pop III BHs are usually formed in low density environments that prevent substantial initial growth (Pelupessy et al. (2007); Alvarez et al. (2009)). Stellar feedback tends to push gas out before a BH is formed (Whalen et al. (2004); Johnson and Bromm (2007)). In case of lower mass progenitors, the central object could be ejected out of the host halo due to the explosion accompanying the final fate of the star, ultimately leading the BH

to be cut off from its fuel supply.(Whalen and Fryer (2012); Woods et al. (2018))
This leaves the other two options as progenitors for SMBHs, runaway stellar collisions in dense nuclear clusters and DCBHs formed in primordial atomic-cooling haloes. More massive initial seeds were furthermore found to come with big enough gas reservoirs to feed the central object for long periods of time (Latif et al. (2013b); Pacucci et al. (2015)).

2.2 Runaway Stellar Collisions

The early Universe provided good conditions for the formation of dense, low metallicity clusters and the therein occurring collisional processes. Clusters with radii of 0.1 pc or smaller would be able to form. Gas enriched by a single SN could lead to even denser clusters as dust grains are efficient cooling agents and can trigger fragmentation at even higher densities. Compared to the protostars forming today, the primordial environment with its higher accretion rate would have allowed for larger protostellar radii. Stellar evolution models found them to be $\sim 300 R_\odot$ (Stahler (1986); Omukai (2001); Omukai and Palla (2003)). Furthermore, very high accretion rates of order ~ 0.1 $\mathrm{M}_\odot yr^{-1}$ are able to significantly boost protostellar radii to $\sim 500 R_\odot$ for a 10 $\mathrm{M}_\odot$ star and to $> 1000 R_\odot$ for a 100 $\mathrm{M}_\odot$ star (Hosokawa et al. (2012, 2013); Schleicher et al. (2013); Haemmerlé et al. (2018); Woods et al. (2017)). Subsequently this leads to an increase in the cross section for collisions, whereas the percentage for protostars engaging in collisions in typical clusters lays between $0.1 - 1\%$ (Baumgardt and Klessen (2011)). Runaway collisions in such dense clusters then produce a central very massive star (VMS) of $\sim 400 - 1900$ $\mathrm{M}_\odot$. Those VMSs would later on collapse to BHs in the mass range of $10^2 - 10^4$ $\mathrm{M}_\odot$with at least 600 $\mathrm{M}_\odot$, which equals to $0.1 - 10\%$ of the black holes mass of a DCBH (Reinoso et al. (2018)). Although massive, this implies a formation pathway for intermediate BHs (IMBH) and not super-massive BHs. Near-Eddington accretion could theoretically lead them to build up enough mass to become super massive at $z > 7$. However, that is very unlikely as they would need enough fuel and high enough accretion efficiencies for substantial growth, which is not necessarily given in their environment. Additionally, orbital dynamics could kick out stars from the cluster and starve IMBHs. (Hirano et al. (2014, 2015); Whalen et al. (2004); Kitayama et al. (2004); Alvarez et al. (2009); Whalen and Fryer (2012); Smith et al. (2018); Latif et al. (2016); Johnson et al. (2013b); Latif and Khochfar (2020); Katz et al. (2015); Sakurai et al. (2017))

2.3 Atomically Cooled Haloes

A feasible solution for forming SMBHs are super massive stars forming in atomically-cooling primordial halos at high redshifts, $z \sim 15 - 20$. Those halos would have been exposed to either unusually strong Lyman-Werner UV fluxes or highly supersonic baryon streaming motions. In order to reach the masses needed to fuel a super massive black hole, the collapsing gas has to evade early fragmentation and efficiently rid itself of angular momentum. One efficient way is to eradicate the main coolant H_2 by either direct destruction or by neutralizing its formation channels. An environment with low gas densities and/or a large ionization background like LW radiation, leads to H_2 production hampering through *photo-dissociation* of H_2

$$H_2 + h\nu \rightarrow H + H^+, \tag{2.13}$$

where $h\nu$ denotes a photon with a certain energy $E = h\nu$. Another process is the inverse of radiative attachment, *photo-detachment*

$$H^- + h\nu \rightarrow H + e^-, \tag{2.14}$$

which operates at photon energies in the range of $E < 0.75eV$. At higher densities with temperatures of $\gtrsim 1000K$ *collisional dissociation* of H_2 becomes efficient

$$H_2 + H \rightarrow H + H + H. \tag{2.15}$$

Destroying H_2 prevents a halo from cooling gas at lower temperatures, thus enabling it to grow to higher masses. Taking a closer look at the Jeans-Mass M_J this becomes more palpable. The Jeans mass is defined in equation 2.3, hence $M_J \approx 10^6$ $\mathrm{M}_\odot(T/10^4K)^{3/2}$ for the critical H_2 density $\sim 10^4cm^{-3}$. In the case of efficient H_2 cooling the gas temperature will fall to $T \approx 100K$ leading to $M_J \approx 10^3$ $\mathrm{M}_\odot$, a Jeans-mass for which normal Pop III star formation is possible. When H_2 is missing the gas temperature is expected to be of order $T \approx 10^4K$ yielding a Jeans -mass of $M_J \approx 10^6$ $\mathrm{M}_\odot$. (Sternberg et al. (2021); McDowell (1961); Lepp and Shull (1984); Palla et al. (1983); Galli and Palla (1998); Stahler (1986); Peebles (1968))

Baryon streaming motions could have the same effect by delaying the collapse of a halo. Originating from baryonic acoustic oscillations of the decoupling of baryons and dark matter after Recombination, they later grow to acoustic waves producing oscillations between baryons and dark matter. That motion could shift baryons far enough away from potential wells to prevent early gas fragmentation. Furthermore, it is able to feed a mini-halo additional energy and angular momentum. Another possibility is the suppression of H_2 formation via supersonic baryon streaming motions. H_2 is suppressed through collisional dissociation by shocks of cold accretion flows colliding near the halo center which also heats the gas. Streaming motions decay as $1 + z$ starting from $\sim 30kms^{-1}$ at $z = 1000$ and having values of $\sim 1kms^{-1}$ at $z = 20$, implying a greater disturbance to haloes forming at higher redshifts and with lower masses. (Latif et al. (2014a); Tseliakhovich and Hirata (2010); Inayoshi and Omukai (2012); Hirano et al. (2017); Stacy et al. (2011))

Haloes subjected to such scenarios would grow to masses of 10^7 $\mathrm{M}_\odot$ and virial temperatures of $\sim 10^4$K, without having formed stars. Once a temperature of $\sim 10^4$K is reached it triggers atomic cooling through collisionally-excited hydrogen and its radiative transitions in the center of the halo. The halo collapses isothermally to a hydrogen number density of 10^6cm^{-3}, becoming later on optically thick to Lyα radiation. Stars are able to form at the center with fuel provided by infall rates of $\sim 0.1 - 1.0$ $\mathrm{M}_\odot yr^{-1}$, which are predicted by stellar evolution codes to evolve as cool, red SMSs. Usually during their thermonuclear life cycle the most massive SMS can directly collapse into black holes of $100.000 - 250.000$ $\mathrm{M}_\odot$ through the general relativistic (GR) instability (Iben (1963); Chandrasekhar (1964)). Pressure support is not able to stabilize the star against its radial pulsations and general relativity's' stronger gravity, allowing for the implosion. This arises due to the GR binding energy increasing more rapidly with density than in the Newtonian case. (Woods

et al. (2017); Fowler (1964); Umeda et al. (2016))
Such high density environments would furthermore offer enough material to sustain a substantial growth through time until the super massive regime is reached. Therefore DCBHs are the favored candidate. They form in massive, dense atomically-cooled haloes fueled even through photo-heating by X-rays. (Shang et al. (2010); Oh and Haiman (2002); Woods et al. (2018)

2.3.1 Lyman-Werner radiation

Previous chapters successfully explored the absence of the coolant H_2 and the resulting higher Jeans-mass, enabling a halo to grow to $\sim 10^7$ $\mathrm{M}_\odot$ through the channels of H cooling. In order to trigger H cooling a halo has to get rid of H_2 or prevent its formation. Ultraviolet photons in the energy range of 11.18 to 13.6 eV corresponding to the Lyman and Werner absorption bands of molecular hydrogen, and therefore called *Lyman-Werner photons*, are able to accomplish this. They can be absorbed by H_2, elevating the molecule from a ground electronic state to an excited state (Lyman or Werner). Subsequently the molecules rapidly decay through radiative decay with roughly 15% of them leading to complete dissociation into the molecules vibrational continuum. This two-step process, see equation 2.16, is known as the *Solomon process*.

$$H_2 + h\nu \rightarrow H_2^* \rightarrow 2H, \tag{2.16}$$

where H_2^* corresponds to one of the 78 LW ressonances between energies of 11.18 to 13.6 eV. Surrounding gas is heated as a result of a portion of the photons kinetic energy being transported away with remnants of the photo-dissociation and due to the other decays being radiative and/or collisional in nature. Photo-dissociation is described in equation 2.13. Collissional dissociation, the other channel in H_2 destruction operates at $> 4000K$ exiting a H_2 molecule into its ground state through the collision with atomic hydrogen as described in equation 2.15. Photo-detachment as showcased in equation 2.14, destroys H^- and therefore prevents H_2 formation via associative detachment. (Draine and Bertoldi (1996); McDowell (1961); Glover and Brand (2001); Stecher and Williams (1967))
LW photons responsible for the devastation come from a general LW background and nearby haloes that underwent fragmentation, Pop III and even Pop II SF earlier. Stars of neighbouring haloes will start their life cycle with thermonuclear fusion and emit photons. Photons are emitted in three energy bands that will affect late blooming haloes as stellar radiative feedback. Those bands are the ionizing band with $E > 13.6eV$, the LW band with 11.18 to 13.6 eV and the photo-detachment at $E < 0.75eV$. Direct dissociation of H_2 is most efficient with stars emitting a hard spectrum of $T_{rad} = 10^5 K$ and photo-detachment of H^- is most powerful through a soft spectrum of $T_{rad} = 10^4 K$ stars. As to not ionize and evaporate the collapsing halo with photons of $E > 13.6$, the atomically-cooling halo and the star bursting halo need to be in sufficient proximity and accordingly synchronized in time. Haloes forming in very close proximity, with one being the subhalo of the other, and most LW photons coming from Pop III stars are called a *synchronized pair* (Visbal et al. (2014)). (Patrick et al. (2020); Johnson et al. (2014); Regan et al. (2017))
The LW background flux necessary to quench H_2 cooling in haloes for as long as they reach enough mass to start atomic cooling, is defined as J_{crit}. J_{crit} is mostly expressed in terms of J_{21}, where J_{21} is defined as the mean intensity of the UV background in the LW band in units

of $J_{21} = 10^{-21} ergs^{-1} cm^{-2} Hz^{-1} sr^{-1}$. H_2 was found to be able to self-shield and survive in the inner most parts of the parent halo with the exception of extremely strong LW fluxes. The actual value of J_{crit} itself remains an elusive parameter as the implementation of LW backgrounds into simulation tends to be tricky.

2.3.2 H$_2$-shielding

The upper paragraphs mentioned H_2 self-shielding briefly. It is the ominous phenomenon of H_2 living in the core of an otherwise atomically cooling halo. In this scenario the inner region of H_2 rich gas can be preserved from photo-dissociation by a large column density ($> 10^{14} cm^{-2}$). H_2 in the outer part absorbs photons able to photodissociate them and therefore leads the inner medium to becoming optically thick to LW absorption line bands. It is however extremely difficult and expensive to compute self-shielding by considering a full radiative line transfer study of individual lines in the LW band. Self-shielding of H_2 is hence estimated as a function of the H_2 column density and gas temperature. In direct application self-shielding of H_2 can be taken into account while calculating the H_2 photo-dissociation rate in the LW bands. Thus, the averaged flux of the LW band is multiplied by a self-shielding factor. The form of the self-shielding factor f_{sh} is still under debate. In Draine and Bertoldi (1996) it is given as a simple power-law approximation

$$f_{sh} = min\left[1, \left(\frac{N_{H_2}}{10^{14} cm^{-2}}\right)^{-\frac{3}{4}}\right], \tag{2.17}$$

where N_{H2} denotes the H_2 column density. It is 1 for $N_{H_2} > 10^{14} cm^{-2}$ and else for $N_{H_2} > 10^{14} cm^{-2}$. The upper equation behaves unphysically for $N_{H_2} \rightarrow \infty$, as is the case at the absence of dust. Therefore Draine and Bertoldi (1996) deduced a more complicated equation to overcome this

$$f_{sh} = \frac{0.965}{(1 + \frac{x}{b_5})^{\alpha}} + \frac{0.035}{(1 + x)^{\frac{1}{3}}} \exp\left[-\frac{(1 + x)^{\frac{1}{2}}}{1180}\right]$$

or slightly rewritten

$$f_{sh} = \frac{0.965}{(1 + \frac{x}{b_5})^{\alpha}} + \frac{0.035}{(1 + x)^{\frac{1}{2}}} \exp\left[-8.5 \times 10^{-4} (1 + x)^{\frac{1}{2}}\right] \tag{2.18}$$

where $\alpha = 2$, $x = \frac{N_{H2}}{5 \times 10^{14} cm^{-2}}$, $b_5 = \frac{b}{10^5 cms^{-1}}$ and b is the Doppler Broadening parameter $b = \sqrt{2}\sigma$, with σ defining the one-dimensional velocity dispersion. The Doppler Broadening parameter is used to define the width of observed spectral lines. In Sugimura et al. (2014) b is defined as $b = \sqrt{2k_B T/2m_P}$, where m_P is the proton mass, k_B the Boltzmann constant and T the gas temperature.

f_{sh} takes a different form in the calculations of Wolcott-Green et al. (2011). They carried out 3D simulations of protogalaxies and fit f_{sh} based on post-processed data, finding that modifying equation 2.18 with $\alpha = 1.1$ produces a better fit. Yet another approach for a more accurate self-shielding factor is given by Richings et al. (2014), who also derived their formula based on equation 2.18. Richings et al. (2014) investigate the diffuse interstellar medium and how it shields against UV radiation, modifying f_{sh} to

$$f_{sh}(N_{H_2}, T_{gas}) = \frac{1 - \omega_{H_2}(T)}{(1 + \frac{x'}{b_5})^{\alpha(T)}} \exp\left[-5 \times 10^{-7}(1 + x')\right] + \frac{\omega_{H_2}(T)}{(1 + x')^{\frac{1}{2}}} \exp\left[-8.5 \times 10^{-4}(1 + x')^{\frac{1}{2}}\right] \quad (2.19)$$

with $x' = N_{H_2}/N_{crit}(T)$ and $b_5 = b/10^5 cms^{-1}$. As they are fitting their parameters to values of *CLOUDY*, they set $\omega_{H_2}(T)$, $\alpha(T)$, $N_{crit}(T)$ to be temperature dependent.

$$\omega_{H_2}(T) = 0.013 \left[1 + \left(\frac{T}{2700K}\right)^{1.3}\right]^{\frac{1}{1.3}} \exp\left[-\left(\frac{T}{3900K}\right)^{14.6}\right] \quad (2.20)$$

$$\alpha(T) = \begin{cases} 1.4 & T < 3000K \\ \left(\frac{T}{4500K}\right)^{-0.8} & 3000 \leq T < 4000K \\ 1.1 & T \geq 4000K \end{cases} \quad (2.21)$$

$$\frac{N_{crit}(T)}{10^{14} cm^{-2}} = \begin{cases} 1.3 \left[1 + \left(\frac{T}{600K}\right)^{0.8}\right] & T < 3000K \\ \left(\frac{T}{4760K}\right)^{-3.8} & 3000 \leq T < 4000K \\ 2.0 & T \geq 4000K \end{cases} \quad (2.22)$$

Furthermore Richings et al. (2014) make changes to the Doppler parameter b as LW affected by Doppler broadening can suppress self-shielding. They include turbulence and calculate b as $b = \sqrt{b_{therm}^2 + b_{turb}^2}$, where $b_{therm} = \sqrt{2k_B T/m_{H_2}}$ with T the gas temperature, k_B the Boltzmann constant and m_{H_2} the H_2 molecule mass. Their turbulence amounts to a constant velocity dispersion of $5kms^{-1}$, which translates to $b_{turb} = 7.1kms^{-1}$. This value of b_{turb} was first used by Krumholz (2012) based on data, that this equals approximately the velocity dispersion of molecular clouds in nearby galaxies.

Since it is monetary impossible to compute the column density without some approximation, accurate estimates have to be found, of which there are several. A few possibilities following Wolcott-Green et al. (2011) are described below.
The H_2 column density is approximated as

$$N_{H_2} = n(H_2)L_{char}, \quad (2.23)$$

with L_{char} being the characteristic length over which the local H_2 number density is constant. Otherwise those parameters change with time. As N_{H_2} is a non-local quantity it is generally expressed by plugging the value for the Jeans-length λ_J (see equation 2.2) into L_{char}. This approximation allows for the derivation of N_{H_2} and f_{sh} through the local parameters H_2 fraction, density and temperature. The use of the Jeans-length however does not implement temperature and velocity gradients of the gas.

Very high velocity gradients can nevertheless change the efficiency of photodisscoiation as LW photons can be shifted in and out of line center from their restframe wavelength due to turbulent motions. Very large and/or supersonic perturbations lead to a column density exceeding the effective self-shielding column density N_{eff}. This discrepancy along a line of sight then is of non negligible order. The Sobolev approximation with its characteristic Sobolev-length L_{Sob} (Sobolev (1957)) offers a solution for calculating N_{H_2}. It defines changes in the mean fluid velocity in terms of the molecular thermal velocity v_{th} as

$$L_{Sob} \equiv \frac{v_{th}}{\left|\frac{dv}{ds}\right|} \tag{2.24}$$

assuming that dv/ds is constant. This means that for a specific line of sight, L_{Sob} is the length for which absorption lines are displaced by one local linewidth. Additionally, this leads to the assumption that local fluctuations of the velocity gradient can be ignored if below L_{Sob} and shielding by molecules above L_{Sob} becomes insignificant. Since this method relies on the Doppler shift, scenarios in which it is not the dominant component could potentially underestimate self-shielding. Yet, it is a useful tool in the supersonic regime.

There are a handful of approaches in realizing the Sobolev length. A non-spherically symmetric geometry requires L_{Sob} to be defined as a single value over the mean of the Sobolev length in all directions. Three-dimensional set-ups depend on the derivation of L_{Sob} and its disscociation rate towards each line of sight individually and then take the mean of it. Another method is to use the over all directions averaged N_{H_2}. In 3D simulations the minimum Sobolev length is often used as a substitute for the magnitude of the velocity gradient.

A new scheme employing the Sobolev length in a slightly different way, was carried out by Gnedin et al. (2009). They defined L_{Sob} over the gas density gradient ρ, $L^{G09}_{Sob} \equiv \frac{\rho}{|\Delta\rho|}$. This characterizes a length above which optical depth is insignificant and for which the gas density is diminished, contributing negligibly to shielding. Though they applied it to a different problem, the usage is interesting and delivers on a rather accurate value of the integrated column density.

Another approximation directly computes N_{H_2} by integrating the H_2 profile along six sightlines. Those lines of sight are parallel to the Cartesian axes. It was used by Yoshida et al. (2003, 2007) and Glover and Mac Low (2007a,b) and although fairly accurate, it is computationally very expensive.

Hartwig et al. (2015) calculated their column densities based on the aforementioned *TREECOL* algorithm from Clark et al. (2012). This approach computes column densities of 3D simulations by determining Doppler shifted lines from velocity gradients of the gas. It is a realistic approach as in a collapsing gas cloud spectral lines are Doppler shifted due to relative velocities between infalling particles. H_2 can then only self-shield when the relative velocity is smaller than the thermal velocity.

Different treatment of self-shielding leads to different values of J_{crit}. Especially a lower critical flux would result in more haloes forming with suppressed H_2 cooling, ultimately leading to a higher probability of producing sites environmentally friendly towards DCBHs and then further on SMBHs. Sugimura et al. (2014) conducted a study by comparing the different approaches mentioned above from Draine and Bertoldi (1996); Wolcott-Green et al. (2011) and Richings et al. (2014). They compared J_{crit} for different blackbody spectra with radiation temperatures

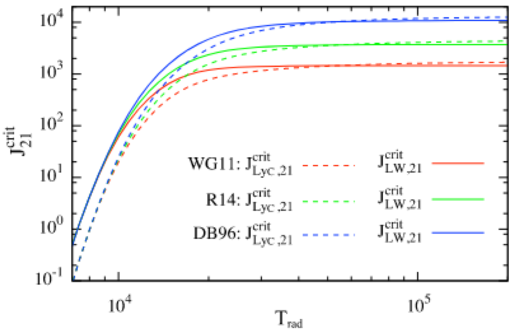

Figure 2.1: Figure 3 from Sugimura et al. (2014) depicting J_{crit} for for different blackbody spectra with T_{rad} and different f_{sh}. Data is taken from Draine and Bertoldi (1996); Wolcott-Green et al. (2011), and Richings et al. (2014) corresponding to DB96, WG11, and R14 in the graph.

T_{rad} and f_{sh} in their figure 3, here figure 2.1, were critical LW flux ist denoted with ’LW’.
They found that J_{crit} is affected by different treatment of f_{sh} mainly towards higher temperatures. In the $T_{rad} = 10^4 K$ regime, dominated by suppression of H_2 formation through H^- photodissociation, J_{crit} yields almost the same results for all approaches. Suppression of H_2 through H^- photodissociation is independent of self-shielding. Reaching towards higher temperatures of $T_{rad} = 10^5$, where H_2 photodissociation and its strength play a key role, discrepancies in J_{crit} are considerable. For instance, J_{crit} derived by means of Wolcott-Green et al. (2011) is up to an order of magnitude smaller than what Draine and Bertoldi (1996) found, hereby showcasing the importance of the implementation and treatment of f_{sh}. Additionally, Hartwig et al. (2015) found that the simple Jeans approximation of N_{H_2} and therefore of f_{sh} leads to an underestimation of a factor 2.
Results in figure 2.1 are not that surprising as f_{sh} from Draine and Bertoldi (1996) is only valid in cases of low density or cold gas. Wolcott-Green et al. (2011) adapted their study by $\alpha = 1.1$ in favor of dense gas for all important temperatures. Furthermore, other discrepancies may arise from the usage of different chemical reactions and cooling functions. Moreover, Richings et al. (2014) calculated f_{sh} for a 1D plane-parallel gas fragment whereas Wolcott-Green et al. (2011) concentrated on 3D simulations of a static gas fragment. (Patrick et al. (2021); Shang et al. (2010); Sugimura et al. (2014); Wolcott-Green et al. (2011); Draine and Bertoldi (1996); Hartwig et al. (2015))

2.3.3 Hybrid cooling

For haloes to grow significantly in mass, not all H_2 has to be destroyed. Yet, the presence of H_2 in atomically cooling haloes brings in new interesting dynamics diverging from the ones in pristine atomically cooled haloes. It is thought to produce a new path of Pop III star formation, hybrid molecular - atomic cooling. In this scenario a halo undergoes collapse by Lyα cooling in its outer parts, while cooling through self-shielded H_2 in its center. Accretion disks turn out to be smaller and infall rates lower than in haloes with pure atomic-cooling gas.
Studies have been conducted to better understand and describe that scenario. Employing resolu-

tions of roughly 300AU, Latif et al. (2020) studied six atomically cooling haloes. They followed them for up to 900kyr in Lyman-Werner backgrounds of $100J_{21}$ and $500J_{21}$. The haloes are spanning masses from a few 10^6 $\mathrm{M}_{\odot}$ to 10^7 $\mathrm{M}_{\odot}$. The results showcase how the core of a given halo is temperature wise dominated by H_2 cooling through self-shielded H_2 with mass fractions of 10^{-3}. Outer parts of the same halo are cooled through atomic hydrogen. Infall rates in such haloes have values of $0.005 - 0.02\mathrm{M}_{\odot}yr^{-1}$. Those environments are able to produce stars of a few thousand solar masses $\mathrm{M}_{\odot}$, due to the accretion rates exceeding normal H_2 sites. However, infall rates are smaller than for purely atomic-cooled haloes. Results are consistent with Suazo et al. (2019) and Regan et al. (2020a) who furthermore found, that this implies a third mode of Pop III star formation in the primordial universe. Moderate LW backgrounds lead to halos atomically cooling in their outer parts while sustaining a H_2 rich core. Virial temperatures are close to the peak of the H_2 cooling curve, few thousand K, yielding higher cooling rates than for smaller haloes. Nonetheless, $Ly\alpha$ cooling rates are not reached. (Patrick et al. (2021))

Therefore this study is going to investigate the collapse of atomically-cooled haloes at a higher LW background implementing self-shielding. Haloes, spanning a range of different properties in order to represent realistic structures, are evolved to up to 5Myrs. This time frame is chosen to accommodate the potential birth of DCBHs even if infall rates are smaller than for purely atomic cooling haloes.

Chapter 3

Numerical Methods

The aim of this chapter is to provide an overview of the tools used for simulating the formation and evolution of atomically-cooling haloes and their visualization. Furthermore the code for generating initial conditions is shortly described.

3.1 Enzo

`Enzo`[4] is an open-source adaptive mesh refinement (AMR), grid-based hybrid (hydrodynamics and N-body) code developed by Bryan et al. (2014) for a variety of astrophysical and cosmological problems. It works in co-moving coordinates, implementing important physical effects like self-gravity, magnetohydrodynamics, and radiative cooling. The code is written in `C + +` and `Fortran77` and parallelization is achieved using the message-passing interface (MPI), putting out data in the cross platform supporting format HDF5 (Bryan et al. (2014)). This provides `Enzo` with the necessary resources required for operating on high-performance computing (HPC) clusters. On `SCIAMA`[5], an HPC cluster in Portsmouth UK, `Enzo` is executed with the `SLURM`[6] job scheduler by submitting batch job scripts. HPC cluster come in various forms and shapes, spanning a wide range of numbers of computer cores and allocated memory per core. Typical clusters have between hundreds and thousands of computer cores with several GB memory per core. `SCIAMA`, supported by the Institute of Cosmology and Gravitation, SEPNet and the University of Portsmouth, consists of 4 288 cores and is spread over 179 compute nodes having a `Lustre`[7] file storage space of 1.8PB. Compute nodes are distributed over different partitions/queues, displayed in table 3.1, and have to be specified in the submitted batch script along with the required time.

---

[4] https://enzo-project.org/

[5] http://www.sciama.icg.port.ac.uk/

[6] https://slurm.schedmd.com/overview.html

[7] https://www.lustre.org/

Queue Name	Nr of Nodes	Cores/Node	Memory/Node	Memory/Core
sciama2.q	95	16	64 GB	4 GB
sciama3.q	48	20	64 GB	3.2 GB
sciama4.q	12	32	192 GB	6 GB
sciama4-12.q	16	32	384 GB	12 GB
sciama4-4.q	4	128	1 TB	
himem.q	1	16	512 GB	
hicpu.q	1	128	125 GB	
gpu.q	2		1 TB	

Table 3.1: Following the `SCIAMA` website, the table displays the number of compute nodes, cores per node, allocated memory per node, and memory per core of the used HPC cluster.

3.1.1 Physical equations

`Enzo` established itself as a very handy tool in astronomical fluid dynamics, finding solutions to the Eulerian equations of ideal magnetohydrodynamics (MHD). Equations being solved by `Enzo` are in co-moving coordinates, following the cosmological expansion and are given, as described in Bryan et al. (2014), as

$$\frac{\partial \rho}{\partial t} + \frac{1}{a}\nabla \cdot (\rho \mathbf{v}) = 0, \tag{3.1}$$

$$\frac{\partial \rho \mathbf{v}}{\partial t} + \frac{1}{a}\nabla \cdot \left(\rho \mathbf{v}\mathbf{v} + \mathbf{I}p^{*} - \frac{\mathbf{B}\mathbf{B}}{a}\right) = -\frac{\dot{a}}{a}\rho \mathbf{v} - \frac{1}{a}\rho \nabla \phi, \tag{3.2}$$

$$\frac{\partial E}{\partial t} + \frac{1}{a}\nabla \cdot \left[(E + p^{*})\mathbf{v} - \frac{1}{a}\mathbf{B}(\mathbf{B}\cdot \mathbf{v})\right] = -\frac{\dot{a}}{a}\left(2E - \frac{B^2}{2a}\right) - \frac{\rho}{a}\mathbf{v}\cdot \nabla \phi - \Lambda + \Gamma + \frac{1}{a^2}\nabla \cdot \mathbf{F}_{cond}, \tag{3.3}$$

$$\frac{\partial \mathbf{B}}{\partial t}\frac{1}{a}\nabla \times (\mathbf{v} \times \mathbf{B}) = 0, \tag{3.4}$$

with E the co-moving total fluid energy density, ρ the co-moving gas density, $\mathbf{B}$ the co-moving magnetic field strength, and $\mathbf{v}$ the peculiar velocity. a is the cosmological expansion parameter and $\mathbf{I}$ denotes the identity matrix. Radiative cooling Λ and heating Γ, as well as the flux corresponding to the thermal heat conduction $\mathbf{F}_{cond}$ are introduced on the right side of equation 3.3.

Equations 3.1, 3.2, 3.3 define the conservation of mass, conservation of momentum, and the conservation of total fluid energy (kinetic, thermal, and magnetic), while in addition representing the first, second, and third moment of the Boltzmann equation. The magnetic induction equation is described with equation 3.4. For a purely hydrodynamic (HD) regime, which this study is,

$\mathbf{B} = 0$ and equation 3.4 as well as the magnetic component of the fluid energy fall away.
The co-moving total fluid energy density E can be calculated as

$$E = e + \frac{\rho v^2}{2} + \frac{B^2}{2a}, \tag{3.5}$$

where e denotes the co-moving thermal energy density. The total co-moving isotropic pressure p^* including the thermal pressure p is

$$p^* = p + \frac{B^2}{2a}, \tag{3.6}$$

with $\mu_0 = 1$. The equation of state (EOS) for an ideal gas with specific heat γ and Poisson's equation for the gravitational potential ϕ are given as

$$e = \frac{p}{(\gamma - 1)}, \tag{3.7}$$

$$\nabla^2 \phi = \frac{4\pi G}{a}(\rho_{total} - \rho_0), \tag{3.8}$$

where $\rho_{total} = \rho_{gas} + \rho_{DM} + \rho_{stars}$, and ρ_0 is the mean density. Note, that the gravitational potential is derived through the total mass density contrast.
Parameters following the cosmological expansion of a smooth, homogeneous background are the expansion parameter $a \equiv 1/(1 + z)$ and the only on time t dependent redshift z. The universal expansion is removed from the coordinate system by determining all spatial derivatives with respect to the co-moving position $\mathbf{x} \equiv \mathbf{x}'/a$, where $\mathbf{x}'$ denotes the position in proper coordinates. Time evolution of the expansion parameter $a(t)$ is followed with the second Friedmann equation. It reads for an expanding, spatially homogeneous and isotropic universe

$$\frac{\ddot{a}}{a} = -\frac{4\pi G}{3a^3}\left(\rho_0 + \frac{3p_0}{c^2}\right) + \frac{\Lambda_c c^2}{3}, \tag{3.9}$$

where p_0 is the co-moving background pressure contribution, Λ_c the cosmological constant and ρ_0 denotes the mean co-moving mass density consisting of baryonic and dark matter. This system holds for the non-relativistic limit and assumes curvature effects negligible, which is true for simulated regions as long as they are small in regards to the radius of curvature and the Hubble length c/H. Here $H = \dot{a}/a$ is the Hubble constant and c the speed of light.
Newton's equations in co-moving coordinates are

$$\frac{d\mathbf{x}}{dt} = \frac{1}{a}\mathbf{v}, \tag{3.10}$$

$$\frac{d\mathbf{v}}{dt} = -\frac{\dot{a}}{a}\mathbf{v} - \frac{1}{a}\nabla\phi. \tag{3.11}$$

They describe the dynamics of collisionless particles, like DM, stars, and BHs, which are modeled as N-body particles. Their contribution to the gravitational potential is governed through Poisson's equation.

Furthermore, `Enzo` is able to solve mass conservation equations for up to 12 chemical species (H, H^+, He, He^+, He^{++}, e^-, H^-, H_2, H_2^+, HD, D^+) with

$$\frac{\partial n_i}{\partial t} + \frac{1}{a}\nabla \cdot (n_i\mathbf{v}) = \sum_j k_{ij}(T)n_i n_j + \sum_j \Gamma_j^{ph} n_j, \tag{3.12}$$

where n_i is the co-moving number density and k_{ij} the rate coefficients for two-body reactions, which are mostly functions of only temperature. Γ_j^{ph} implements the destruction and creation rates due to photo-ionization and/or photo-dissociation. Additionally the advection of one or more co-moving metal density fields is monitored, as they can play a role in radiative cooling and in SF.

Radiation can be implemented either as a homogeneous background or as an inhomogenous radiation field. `Enzo` is able to track the inhomogenous field by directly solving the radiative transfer equation along rays or by calculating momentum equations from the radiation field and solving them. (Bryan et al. (2014))

3.1.2 Adaptive Mesh Refinement

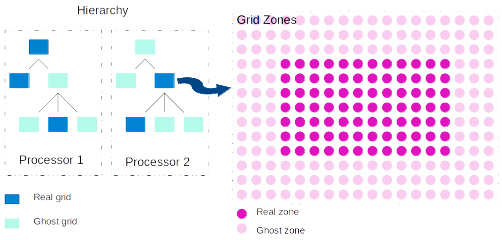

Figure 3.1: Grid schematics based on Figure 1 of Bryan et al. (2014) displaying a grid hierarchy on the left and a $2-D$ grid example on the right.

The `Enzo` AMR is based on the structured adaptive mesh refinement (SAMR) technique on a Cartesian mesh from Berger and Colella (1989). AMR efficienlty adjusts grid sizes, overlaying the base grid with sub-grids whenever a cell is flagged for refinement due to critical processes in need of higher resolution. A single root grid over the whole computational space works as the basis on which subgrids (child grid) are placed for further refinement. This forms a tree like structure to which subgrids of subgrids can be added and so on as to cover the necessary resolution. Therefore a child grid can become a parent to another higher resolution child. `Enzo` then enforces certain grid conditions to maintain efficiency. Thus, restricting high-resolution child grids to be completely enveloped by its parent and requiring its edges to align with the cell edges of its parent. Cells are accumulated into grids. Additionally, all grids are forced to align with the main axes x, y, z. The mesh spacing ratio between a parent and child grid is for cosmological simulations usually set to 2.

Refinement is estimated by a variety of criteria, including baryon and DM overdensities, shocks, Jeans length and cell cooling time. Refinement can take place anywhere in the simulation and/or in a specified region. Subgrids can also be fixed over a subvolume of a simulation in order to start with a higher initial resolution. Figure 3.2 showcases how AMR increases the resolution of certain parts of a simulation by overlaying it with more grids. Figure 3.1 shows simplified schematics of the hierarchical grid structure and a $2-D$ example grid distribution.

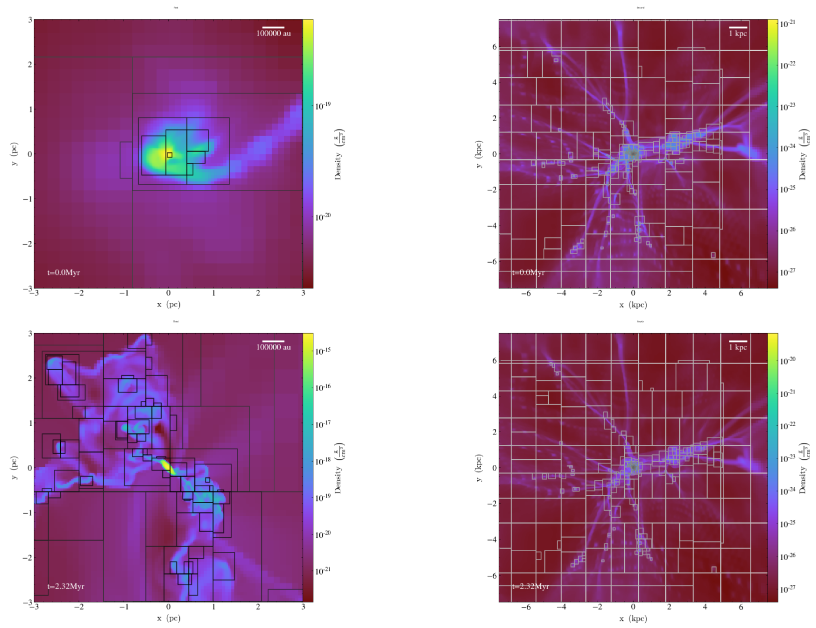

Figure 3.2: Grids displayed for Halo 2 in a Slice-Plot. The upper row displays the time at the onset of atomic cooling and the lower row at 2.32Myr. The columns display the grids for a slice size of 6pc on the left and 15kpc on the right.

`Enzo` uses grid patches as a primary data structure, storing information about field variables and particle data in each patch. They are treated as individual objects, organized into a dynamic and distributed hierarchy. A simple dynamic load-balancing is used to spread the workload uniformly over all used processors. Grids are distributed as real grids embedded in surrounding ghost zones. Ghost zones store temporary data from a processor not allocated to it, whereas real grids are allocated to a certain processor and store its field values. A grid can therefore only be a real grid on one processor and a ghost grid on all others. Ghost zones are needed to store data from hydro-solvers, gravity solvers and PPM to only name a few. For instance the hydro-solver needs a three layer thick ghost zone to contain its input, similar to the simplified view in figure 3.1. (Bryan et al. (2014))

Timesteps

Timesteps, in which physical equations are solved, are determined hierarchically level-by-level by identifying the biggest timestep that satisfies certain criteria. Calculations proceed in a time subcycling way starting with the lowest level 1 and progressing all grids on that level by one timestep Δt. Once this step is taken, another one follows on all grids to $l+1$ at the next refinement level, iterating this process until the finest level is resolved and then advancing until the level above is reached. Once this is achieved, the finest level is synchronised to the one above and progressed by one additional timestep. Grid information is shared after every Δt, updating adjacent ghost zones by interpolating from a parent and/or sharing data with neighbouring grids.

Furthermore, it is analyzed which parts are in need of refinement subsequently upending the gird hierarchy to accommodate the new requirements. This is done for every level of refinement allocated to the simulation. Each level l determines its own timestep size progressing all grids on the same level by it, invoking the condition of not exceeding the timestep of $l-1$. (Bryan et al. (2014))

Some of the timestep criteria following Bryan et al. (2014) and displaying the 1D version for simplicity, are

$$\Delta t_{hydro} = min\left(\kappa_{hydro}\frac{a\Delta x}{c_s + |v_x|}\right)_L, \tag{3.13}$$

$$\Delta t_{DM} = min\left(\kappa_{DM}\frac{a\Delta x}{v_{DM,x}}\right)_L, \tag{3.14}$$

$$\Delta t_{accel} = min\left(\sqrt{\frac{\Delta x}{|\mathbf{g}|}}\right)_L, \tag{3.15}$$

$$\Delta t_{rad} = min\left(\sqrt{\frac{\Delta x}{|\mathbf{a}_{rad}|}}\right)_L, \tag{3.16}$$

$$\Delta t_{exp} = f_{exp}\left(\frac{a}{\dot{a}}\right), \tag{3.17}$$

where $(...)_L$ denotes that this value is taken for all cells or particles on a level L and the minimum value is calculated as the timestep.

Refinement Criteria

`Enzo` has a variety of criteria that mark a cell for refinement using physical parameters. Depending on the scientific question, 19 different methods can be employed, which are refinement by slope, baryon mass, shocks, particle mass, Jeans length, cooling time, and metallicity to only name a few. Cosmological simulations usually require cells to be flagged based on the baryon mass and particle mass.

A cell is flagged for refinement by *baryon mass* if the baryonic mass of the cell exceeds a specified value.

$$M_g > \rho_{flag}\,(\Delta x_{root})^d\, r^{\epsilon_l l}, \tag{3.18}$$

with $M_g = \rho(\Delta x)^d$ the baryonic cell mass. Here r is the refinement factor, l the refinement level, ρ_{flag} is the needed density of the rood grid for refinement and Δx_{root} the root grid cell spacing. Additionally ϵ_l specifies super-Lagrangian or sub-Lagrangian refinement as this refinement factor tries to work similarly to a Lagrangian method and sustain a fixed mass resolution.

Refine by *particle mass* focuses on refining based on dark matter and stellar density. It works similarly like the baryon mass flag with the difference that it uses gridded particle densities.

The flag for the *Jeans length* refinement is based on the Truelove criterion (Truelove et al. (1997)). It forces `Enzo` to refine the Jeans length by a fixed specified number of cells in order to account for artefacts. Cells are flagged when

$$\Delta x < \left(\frac{\gamma \pi k_B T}{N_J^2 G \rho \mu m_H} \right)^{\frac{1}{2}}, \tag{3.19}$$

where N_J is the manually specified number with which the Jeans length has to be resolved, and Δx the cell length. (Bryan et al. (2014))

3.1.3 Overview of Hydrodynamics, Gravity and N-body dynamics

`Enzo` utilizes four different (M)HD methods with one of them being the hydrodynamic-only piecewise parabolic method (PPM) based on the code from Woodward and Colella (1984) and extended to cosmology by Bryan et al. (1995). It is an explicit, higher-order accurate version of the Godunov PPM method, developed for solving ideal gas dynamics using a spatially third-order accurate piecewise parabolic monotonic interpolation and capturing shocks with a nonlinear Riemann solver. Bryan et al. (1995) furthermore implemented modifications for usage in hypersonic flows, as the thermal energy e is extremely small in regards to the total energy E which can cause otherwise large numerical inaccuracies. This *DualEnergyFormalism* is implemented for stability and accuracy in the hyper-Machian range and can be switched on and off manually.

Currently, a variety of Riemann solvers have been introduced to `Enzo`. To be accurate, five approximate Riemann solvers take on the job of calculating the Riemann problem in `Enzo`, as finding an exact solution would be tremendously costly. Those Riemann approximations are a two-shock scheme (Toro (1997)), the Harten-Lax-van Leer (HLL; Toro (1997)) solver, HLL with a contact discontinuity (HLLC; Toro (1997)), HLL with multiple discontionuities (HLLD; Miyoshi and Kusano (2005)), and the Local Lax-Friedrichs (LLF) solver. A Riemann solver fallback is employed for the PPM method when negative densities or energies are calculated in high-order solutions, falling back on a more diffusive HLL Riemann solver for the erring cell. This fallback can be switched on and off manually.

Self-gravity is introduced in `Enzo` by first distributing massive (DM, stars) particles onto the grid using a second-order cloud-in-cell (CIC) interpolation technique, secondly calculating Poisson's equation on the root grid on each time step with the fast Fourier technique from Hockney and Eastwood (1988), and lastly the Dirichlet boundary conditions of the potential on each subgrid are solved using a multigrid relaxation technique. Accelerations are found by determining the potential and subsequently interpolating it back to particles. This scheme allows for fast and accurate periodic and isolated boundary conditions of gravity, self-consistently computing the gravitational potential emerging from baryon fields and particles.

A particle-mesh N-body method is utilized in `Enzo` to compute the dynamics of collisionless systems following the standard drift-kick-drift technique of Hockney and Eastwood (1988). Modeled with particles, collisionless matter (DM,stars, BH) is set to interact with baryons only through gravity, their dynamics calculated following trajectories of a sample of particles. They are not adaptively refined as they follow the collapse of structures and are thus allocated the highest level of refinement available at their position, encountering the same time step and gravitational pull as a grid cell of that level. In order to avoid unphysicalities to the gravitating mass field,

contributions from higher level particles are smoothed over a spherical region centering on each particle's position.
Bryan et al. (2014) provide a more in depth description.

3.1.4 Chemistry

`Enzo` allows for the implementation of up to 12 species, utilizing a non-equilibrium chemical network. That was initially based on work done by Abel et al. (1997) and Anninos et al. (1997) and update with reaction rates from McGreer and Bryan (2008) and Turk (2009). This is controlled by the *Multispecies* parameter, which when turned to 0 means off, 1 works with six species $(H, He, e^-, H^+, He^+, He^{2+})$, set to 2 includes nine species adding H^-, H_2, H_{2+} which are important for the gasphase molecular hydrogen formation, and set to 3 utilizes 12 species including D, D^+, and HD . The code monitors the total density, the ionization states of Hydrogen and Helium as well as cooling and heating of each species. Rate equations are calculated, keeping stability in mind, with one Jacobi iteration of an implicit Euler time discretization. 29 kinetic and radiative processes stemming from nine kinetic equations for the 12 species are solved (see Table 2 and 3 of Bryan et al. (2014)). Those are then sub-cycled within one hydrodynamic timestep in order to maintain accuracy. Radiative heating and cooling due to atomic and molecular line excitation, recombination, collisional excitation, free-free transitions, Compton scattering of the CMB, as well as models for UV backgrounds that are heating the gas via photo-dissociation and photo-ionization are calculated in `Enzo` and updated either at the same hydrodynamical timestep or within the same sub-cycle. (Bryan et al. (2014))

Cooling

`Enzo` is able to directly compute the cooling and heating rates of H and He attributed to the processes of collisional excitation and ionization, recombination, free-free emission, Compton scattering of the CMB, and photoheating from a UV background. By setting *Multispecies = 2* and enabling H_2 chemistry, the code furthermore solves ro-vibrational transitions (Glover and Abel (2008); Galli and Palla (1998)), heating and cooling from H_2 formation and destruction (Turk et al. (2009)), and collision-induced emission (Ripamonti and Abel (2004)). *Multispecies = 3* additionally allows for the calculation of the rotational transitions of HD (Galli and Palla (1998); Lepp and Shull (1984)). Those mechanisms are further controlled through the *RadiativeCooling* parameter.
Cooling through metals can be introduced into `Enzo` in three ways, the simpler pathway is through an analytic cooling function from Sarazin and White (1987), the second one being tables of multidimensional cooling and heating rates calculated with the photo-ionization code *CLOUDY* Ferland et al. (1998, 2013, 2017), and through outputs of a Raymond-Smith code of Cen et al. (1995) that calculates cooling rates for $T > 10^4 K$.

Radiation

Most of the radiation fields interacting with the cooling and heating routines in `Enzo` use fits for the H, He and He^+ ionizing and photo-ionization heating rates of the form, as described in Bryan et al. (2014),

$$rate = k_0(1+z)^{\alpha} \exp\left(\frac{\beta(z-z_0)^2}{1+\gamma(z+z_1)^2}\right), \tag{3.20}$$

with literature values for the constant coefficients α, β, γ, z_0, and z_1. They are controlled by the parameter *RadiationFieldType*, which subsequently sets up one of nine different approaches for calculation. For instance *RadiationFieldType = 1* imposes a homogenous radiation background based on Haardt and Madau (1996) with a quasar spectra slope of $q_\alpha = 1.5$, whereas *RadiationFieldType = 9* implements a constant molecular H_2 photo-dissociation rate. Molecular hydrogen dissociation rates can be normalized using the *RadiationSpectrumNormalization* parameter, which is multiplied to the rate. Approximate radiative shielding is introduces by the *RadiationShield* parameter and shields when set to 1 H and He, and when set to 2 it follows the Sobolev-like approximation of Wolcott-Green et al. (2011) for H_2 shielding.

Radiation transport through ray tracing in `Enzo` follows the approach from Wise and Abel (2011). Another radiation transport solver is field-based and coupled to the gas energy and chemical number density. It focuses on a flux-limited diffusion approximation for cosmological radiative transfer, a problem encountered on uniform grids.

3.2 Cosmological Initial Conditions

Initial conditions set the ground work for successful simulations, laying down the appropriate grids and physics for numerical studies to evolve from. This is usually done by starting from redshifts $z = 150 - 200$, which cover the description of the Universe with a linear power spectrum and describe matter fluctuations with Gaussian distributions. Cosmological initial conditions are not generated by `Enzo` itself and have to be set up with other packages like `MUSIC`, `inits`, or `mpgrafic`. The initially used code was `inits`, however, the most commonly used today is probably `MUSIC`, which computes uniform or zoom-in initial conditions with multiple levels of refinement for hierarchical sets of nested regions.

`MUSIC`, short for MUlti-Scale Initial Conditions, was developed by Hahn and Abel (2011) and build upon work by Pen (1997); Bertschinger (2001) and Sirko (2005). Hahn and Abel (2011) are making use of an adaptive convolution of Gaussian white noise with a real-space transfer function kernel and an adaptive multi-grid Poisson solver to compute velocity fields and particle displacements at the first- and second-order Lagrangian perturbation theory (LPT1, LPT2). Their usage of a hybrid Poisson solver, implementing an adaptive multi-grid algorithm for the hierarchy of grids and a Fast Fourier Transform (FFT) for grids on the highest level, leads to a good reproduction of small-scale perturbations without their suppression. The algorithm initializes Gaussian primordial density fluctuations based on a set of random seeds, that can be drawn with a random number generator or specified as wished, which subsequently determines the large scale structure and noise refinement. Those have to be specified in an input file together with other quantities like the simulation box size, the starting redshift, cosmological parameters, the input transfer function, refinement levels, the number of nested grids, and their extent over the simulation volume. Random seeds create a unique environment and changing even a single digit will alter a whole simulation run, hence for investigating the same structures random seeds have to stay fixed. `MUSIC` then proceeds to put out a grid-set up and a parameter file, that has to be adjusted with more physical parameters as well as control parameters for `Enzo`. Once this is done, a simulation run can be started. (Hahn and Abel (2011); Surace (2020))

3.3 Data Analysis

Data analysis and visualization of astrophysical simulations can be quite challenging, pushing worktools like `yt`[8] (Turk et al. (2011)) into focus. This tool is a community developed, open source code, which is written mainly in `Python`[9] and has some routines coded in `C`. `yt` can be used in `Python` as a module or imported as a library, while itself depending on `NumPy`[10] (Harris et al. (2020)). It was originally developed for `Enzo` outputs and updated to handle data from *Orion*, *RAMSES*, *FLASH*, and *CASTRO* to name a few. The code focuses on analyzing and visualizing important physical quantities instead of quantities put out by simulations. `yt` is able to calculate important physical quantities, make multi-dimensional profiles and visualize them in 2-D and 3-D slice plots or projections from reading the simulations (`Enzo`) mesh and fluid information. Information about the AMR grids and cells itself, like cell edges or grid overlays, can be called by the code. Analysis is made easier by enabling defined simulation field variables to be called at leisure and by defining physical quantities like the angular momentum vector as data objects (*quantities.angular_momentum_vector()*), which `yt` is self-consistently able to calculate when called. Furthermore, it is able to sift through a simulation box to find the location and value of maxima and/or minima with a *find_max()/find_min()* command, setting it as the plotting center if required. An important quantity used is the *find_max('density')*, which is used to find the most massive halo centers in this studies zoom-in simulations. Another useful application is the *quantities.total_quantity*() command, which calculates the total amount of a field (e.g. mass) in a specified area when asked by defining for example a sphere over a certain region with *ds.sphere(location, radius)*, where ds denotes the read-in simulation data. `Enzo` puts out quantities in code units that can be easily converted into real values with `yt`, by setting *.in_units()* or *.set_unit()* to the desired magnitude (e.g. Msun; 'HM_Density','g/cm**2'). Simulation time and real time are likewise tracked with `yt`. Additionally, different sub-scripts of `yt` are for instance able to identify haloes in cosmological simulations and build hierarchies of merger trees (`ytree`; (Smith and Lang (2018))). Other `Python` packages used in this work are `matplotlib`[11] (Hunter (2007)), `pandas`[12] (pandas development team (2020); Wes McKinney (2010)), and `NumPy`. (Turk et al. (2011); Bryan et al. (2014))

3.4 Simulating atomically-cooled Haloes

Initial conditions for the 8 simulated haloes were provided by Patrick et al. (2020), where they identified and choose haloes of different formation histories and spin parameters. Those haloes are then simulated in a $10^5 J_{21}$ LW background.

The earlier explained `Enzo` AMR cosmology code is used for this study. Characteristic parameters used are the piecewise parabolic method for hydrodynamics (PPM; Woodward and Colella (1984);

---

[8] https://yt-project.org/

[9] http://www.python.org/

[10] https://numpy.org/

[11] https://matplotlib.org/

[12] https://pandas.pydata.org/

Bryan et al. (1995)) and the HLLC scheme. The HLLC scheme provides enhanced stability for strong shocks and rarefaction waves (Toro et al. (1994)). Evolution of Dark Matter is traced through an N-body adaptive particle-mesh scheme. Dynamics of collisionless particles are calculated following trajectories of a sample of particles (Efstathiou et al. (1985); Couchman (1991); Bryan and Norman (1997); Hockney and Eastwood (1988)). The adaptive particle-mesh scheme is self-consistently linked to the nonequilibrium primordial gas chemistry and gas flows (Anninos et al. (1997); Glover and Abel (2008)). Furthermore, $Multispecies = 2$ is used, implementing nine species $(H, He, e^-, H^+, He^+, He^{2+}, H^-, H_2, H_{2+})$. Additionally collisional excitational and ionizational cooling thorugh H and He , H_2 cooling, cooling through Bremsstrahlung, recombination cooling as well as inverse cooling by the CMB are utilized. Self-shielding of H_2 against the LW background is calculated following the Sobolev-like approximation of Wolcott-Green et al. (2011).

3.4.1 Simulation Setup

The starting point for the 8 simulations is a redshift z of $z = 200$ and a comoving simulation box size of 1.5Mpc h^{-1}. Simulations initialize between 27503288 (halo 12), 28293672 (haloes: 2, 8, 19, 20) and 29142800 (haloes: 1, 10, 16) particles, showcasing designated haloes in the center of the box.
Initial conditions are generated by `MUSIC` (Hahn and Abel (2011)), as was described in section 3.2, implementing the second-year *Planck* cosmological parameters: $\Omega_M = 0.308$, $\Omega_\Lambda = 0.691$, $\Omega_b h^2 = 0.0223$, $\sigma_8 = 0.816$, $h = 0.677$, $n = 0.968$.(Planck Collaboration (2016))
Simulations have a top grid resolution of 256^3. Additional three nested grids with a resolution of 256^3 each, are centered on the targeted halo enclosing 20% of the simulation. This adds up to a DM mass resolution of 28 $M_\odot$ and baryon mass resolution of 34 $M_\odot$. A maximum physical resolution of 0.014pc is reached by employing 15 levels of refinement. Refinement on baryon and particle mass as super-Lagrangian is implemented from the beginning. Baryon or DM overdensities exceeding eight times the mean density ($\delta\rho/\overline{\rho} > 8.0$) lead to grids being marked for refinement.
The Simulation is stopped for the first time at z=30, were refinement on the Jeans length is turned on manually to ascertain physical matter clumping. 32 cells are set to cover the Jeans length in order to resolve important physical processes, like the formation of turbulent structures, and the Truelove criterion (Truelove et al. (1997)). Otherwise contamination by artificial fragmentation due to a violation of the Jeans criterion would diminish the reliability of the results (Truelove et al. (1997); Latif et al. (2013a)). Numerical artifacts are further avoided by smoothing DM particles at the tenth level of refinement, as baryons dominate the collapse below pc scales and can unphysically heat and accelerate surrounding gas if higher resolutions lack enough DM particles. This is equivalent to a comoving resolution of 5.72pc.
The simulation is then stopped for a second time at the onset of the atomically-cooled halo collapse, when the maximum refinement level is reached. To stabilize the collapse on the smallest scales a pressure floor is activated manually by setting a minimum temperature in the highest refined cells following the approach of Machacek et al. (2001). Additionally Cells are kept Jeans stable and are prevented from collapsing on scales below the maximum resolution, which could cause artificial fragmentation and non-angular momentum conservation. Data is set to be put

	z_{col}	mass ($M_\odot$)	spin	mergers
Halo 1	16.7	3.68e7	0.0389	1
Halo 2	14.5	8.47e7	0.0388	0
Halo 8	20.4	1.15e7	0.0321	0
Halo 10	17.3	2.60e7	0.0500	1
Halo 12	16.80	1.93e7	0.0471	0
Halo 16	16.5	2.91e7	0.0258	3
Halo 19	13.9	2.12e7	0.0072	0
Halo 20	17.7	3.56e7	0.0199	0

Table 3.2: Properties of the eight designated haloes from Patrick et al. (2020) at the onset of atomic cooling.

out every 10kyr to capture accretion rates and the gravitational collapse. A collapsing halo is followed for up to 5 Myrs (Patrick et al. (2021)).

3.4.2 Halo Properties

The data for the eight haloes simulated in this thesis is provided by Patrick et al. (2020). They performed initial DM only runs in order to identify potential candidates through spin parameters and accretion history at the onset of atomic cooling. Subsequently they selected a scientific sample based on various spin parameters and evolution history (accretion, major merger and or both). Major mergers are defined there as the collision between two haloes of a mass ratio of at least 1/5. The spin parameter λ is defined as (Peebles (1969);Bullock et al. (2001))

$$\lambda = \frac{|L|\sqrt{|E|}}{GM^{\frac{5}{2}}} = \frac{|L|}{\sqrt{2GRM^3}}, \tag{3.21}$$

where L denotes the angular momentum, R the virial radius, M the virial mass of the halo and G the gravitational constant. Properties are taken from Patrick et al. (2020) and listed in table 3.2. They include the collapse redshift z_{col}, mass and spin λ at the onset of atomic cooling as well as merger history. Initial haloes were identified through *ROCKSTAR* (Behroozi et al. (2013)), which determined the position, mass and velocity of each halo. Merger trees were then build using `ytree` (Smith and Lang (2018)) on the previously output data from *ROCKSTAR*. They follow the haloes from z=25 until z=15 in Δz=0.5 steps.

Halo assembly histories therefore vary. Halo 16 evolved through three major mergers where as halo 2 has zero major mergers in its history and grew mostly through accretion. Halo 1 and halo 10 encounter a major merger each while evolving. Halo 10 also has the highest spin parameter, followed closely by halo 12. Halo 12, however, did not live through a major merger accumulating its high spin through accretion of matter. Halo 19 grew mostly through accretion and halo 8 and 20 are products of minor mergers and accretion. The common factor being low-mass ancestor haloes in the merger tree (see figure 1 Patrick et al. (2020)). For greater detail on assembly histories in the no-H_2 runs, consult Patrick et al. (2020).

3.4.3 LW Backgrounds

Haloes are evolved in a LW background of $10^5 J_{21}$. This value is set to build on results from Patrick et al. (2021) in order to map the upper limit of J_{21} and better approximate the total destruction of H_2 and isothermal cooling in haloes. We estimate, that it will probably walk the edge between isothermal and H_2 cooling. The LW backgound is modeled as a constant molecular H_2 photo-dissociation rate (*RadiationFieldType = 9*) multiplied by the set value of J_{21}, here $10^5 J_{21}$ (*RadiationSpectrumNormalization = 1.0e-16*). H^- photodetachment continuum photons with energies $< 0.755 eV$ are not included, as their effects are most likely covered by the LW backgrounds implemented. In general, however, disregarding photodetachment photons can lead to overestimations of H^- mass fractions in the center of haloes, where they could potentially cool it to $\sim 5000K$(O'Shea and Norman (2007)). Those temperatures lie below of what is achievable by $Ly\alpha$ cooling and are almost perfect for the formation of H_2 through H^-. This effect including higher densities due to the lower temperatures, could result in an overestimation of H_2 mass fractions and self-shielding in halo cores of this study.

Self-shielding of H_2 against the LW background is computed following the Sobolev-like approximation of Wolcott-Green et al. (2011) (*RadiationShield = 2*).

Chapter 4

Results and Discussion

In this section results for the simulations of a $10^5 J_{21}$ LW background are presented. The disk evolution and accretion rates for each halo are described in detail. Initial time $t = 0.0$ is defined as the time of the onset of the rapid gas collapse when the densest cell of the simulation reaches the maximum refinement level 15 for the first time. Table 4.1 shows the summarized data from the simulations of Patrick et al. (2020), Patrick et al. (2021) and this work. It displays the redshifts at collapse corresponding to the different LW backgrounds. Results from Patrick et al. (2020) and Patrick et al. (2021) are included for comparison purposes and better understanding.

4.1 Early Beginnings

Onset of atomic cooling (here t=0.0) occurs at different redshifts for the different haloes simulated in this work, ranging from $z \sim 14.11$ for halo 19 to $z \sim 20.89$ for halo 8. Tabel 4.1 shows the different collapse redshifts in which halo 1 collapses at z=16.89, halo 2 at z=14.60, halo 8 at 20.89, halo 10 at z=17.74, halo 12 at z=16.98, halo 16 collapses at z=17.16, halo 19 at z=14.11, and halo 20 at z=18.03. Temperature profiles against radius at t = 0.0 are displayed in figure 4.1, where they show a similar trend for all simulated haloes. Temperatures of $\sim 10^3$ K are found in the halo center and rise to $\sim 10^4 K$ between 1pc and 10pc outwards, followed by a plateau which drops rather rapidly towards larger radii of $\sim 10^2 - 10^3$ pc. Halo 2 has the largest and boxiest plateau of the sample, while halo 8, the first to collapse, shows the sharpest and smallest peak in temperature. The lower temperatures towards the halo center are due to self-shielded H_2 cooling through its collisionally excited rotational and vibrational transitions, whereas the higher temperatures of $\sim 10^4$ K correspond to atomic H cooling. Halo 2's boxier shape might be attributed to the fact that it has a companion halo at a distance of 200 pc, which is more pronounced in figure 4.2 (b). Figure 4.2 (b) features a bump at 10^2 pc in the number density, corresponding to the neighbouring halo of halo 2 (see also C.1). Otherwise figure 4.2 displays a similar trend for all simulated haloes, with a peak of the number density in the center and a falling slope towards larger radii. Additionally, the steepness of the slope is comparable for all haloes. Furthermore, the radial profiles show good agreement to radial profiles from earlier studies of high and intermediate LW backgrounds and self-shielded H_2 (e.g. Patrick et al. (2020, 2021); Regan and Downes (2018a); Suazo et al. (2019)).

	no H_2	$10^5 J_{21}$	$10^4 J_{21}$	$10^3 J_{21}$	$10^2 J_{21}$
Halo 1	16.7	16.89	17.4	18.5	30.0
Halo 2	14.5	14.60	15.5	18.9	28.9
Halo 8	20.4	20.89	22.1	22.7	33.3
Halo 10	17.3	17.74	17.9	18.4	28.4
Halo 12	16.80	16.98	-	-	-
Halo 16	16.5	17.16	-	19.0	27.1
Halo 19	13.9	14.11	14.7	15.3	21.1
Halo 20	17.7	18.03	-	-	-

Table 4.1: Redshifts of Halo collapse corresponding to different LW backgrounds. Data for the no H_2 column has been taken from Patrick et al. (2020) and for $J_{21} = 10^4, 10^3, 10^2$ from Patrick et al. (2021). Values for $10^5 J_{21}$ are the work of this thesis.

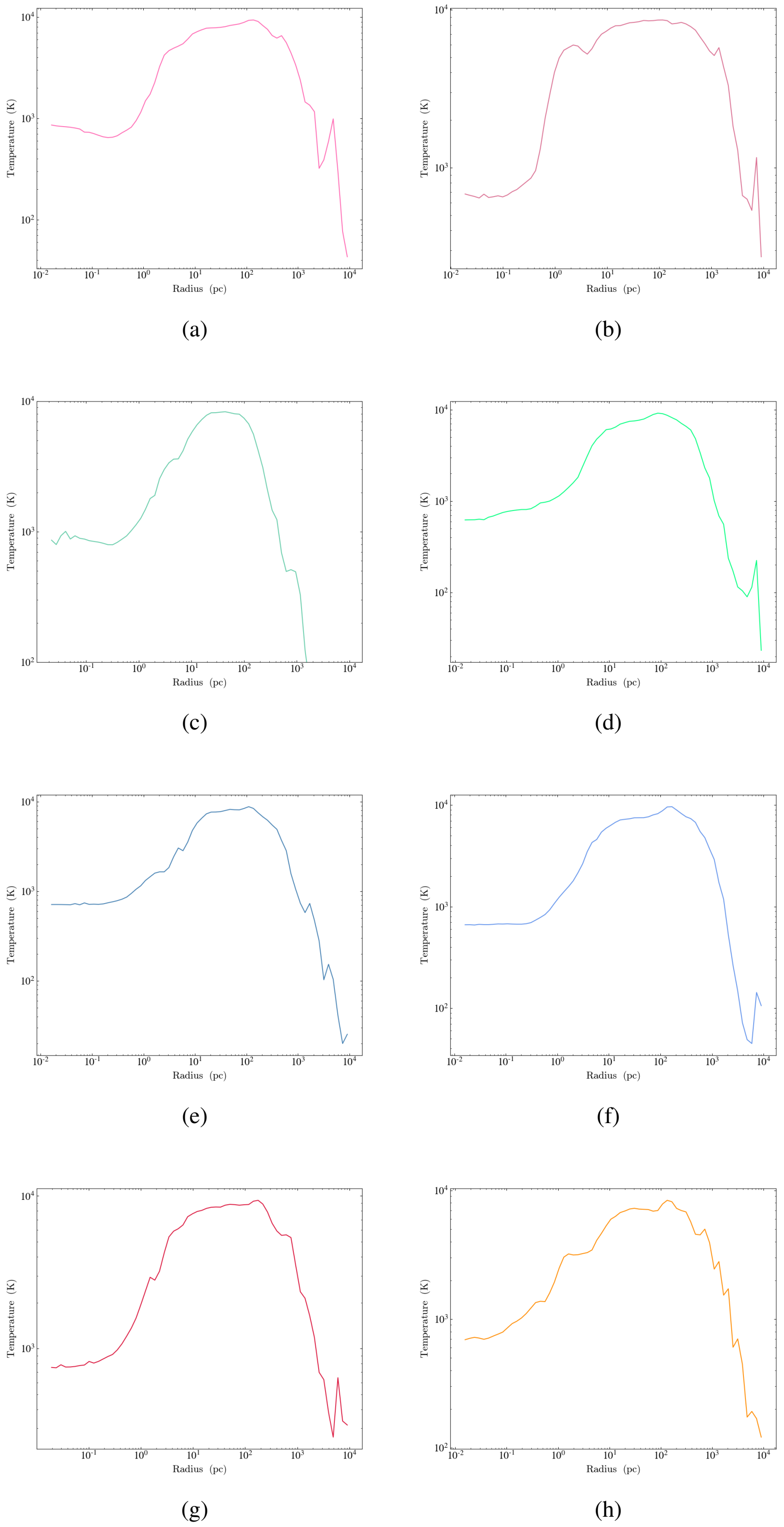

(a) (b)

(c) (d)

(e) (f)

(g) (h)

Figure 4.1: 1-D temperature against radius profiles at the beginning (t=0.0) of catastrophic baryon collapse for the simulated haloes 1, 2, 8, 10, 12, 16, 19, and 20 displayed in subfigures (a), (b), (c), (d), (e), (f), (g), and (h) respectively.

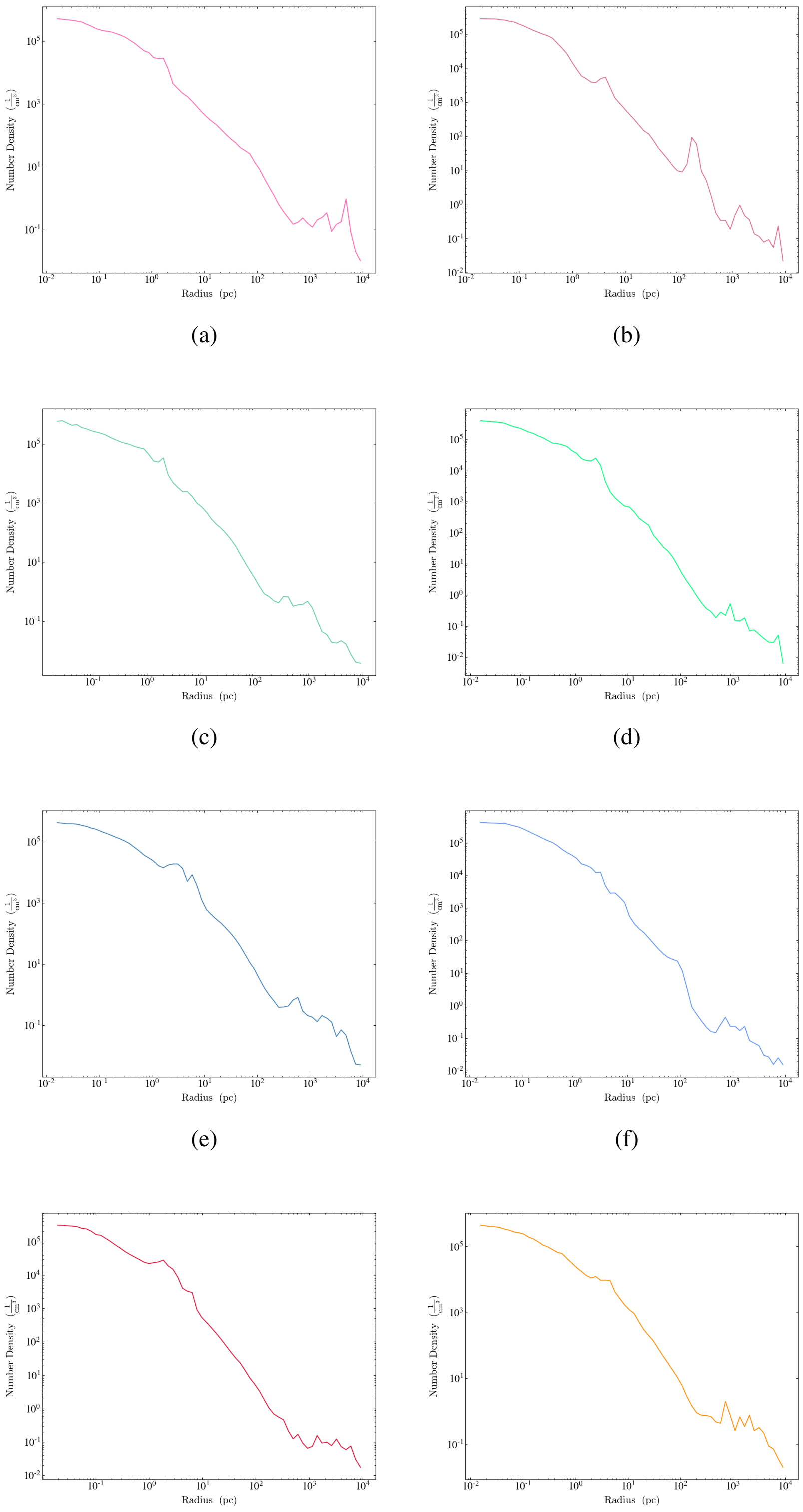

(a) (b)

(c) (d)

(e) (f)

(g) (h)

Figure 4.2: 1-D number density against radius profiles at the beginning (t=0.0) of catastrophic baryon collapse for the simulated haloes 1, 2, 8, 10, 12, 16, 19, and 20 displayed in subfigures (a), (b), (c), (d), (e), (f), (g), and (h) respectively.

4.2 Disk Evolution

Once catastrophic baryon collapse is triggered, a dense spherical core is formed which is surrounded by an accretion disk. The gas is flattened around the core due to rotation and at $\sim 0.5 - 0.7 Myr$ after the collapse a bar instability creates spiral arms. Due to the increase in angular momentum with infalling matter, the spherical center gets more elongated/ellipsoid over time. Temperatures tend to be of order $\sim 10^4$K in the center of the disk, while surrounded by cooler 10^3K H_2 rich gas. Some haloes showcase the trend of a small, cool H_2 core surrounded by hot 10^4K gas, which is embedded in a larger self-shielded H_2 environment. H_2 fractions rise over time, corresponding to the disks getting denser. H_2 manages to self-shield against LW radiation in all simulated runs, however, Lyα cooling is still the dominant process.

Halo 1 starts to form a dense, cold core that starts cooling through the channels of H_2 to $\sim 10^2$K at around 0.228Myr. The clump grows in density and size, until at $\sim$ 0.47Myr atomic cooling is triggered. At roughly ~0.5Myr after the collapse a smaller cold, dense clump forms in a 1pc distance to the core and is accreted at 0.625Myr. The halo then proceeds to cool trough Lyα in the center and isothermally on the outer parts. This is shown in figure 4.3 where the temperature plots in the middle display a red small structure cooling at $10^4 K$ surrounded by gas of cooler temperatures in green. Lower plots of figure 4.3 show the H_2 mass fraction which corresponds to this picture, where a region with very low H_2 density exists close to the central object. Halo 1 proceeds to evolve in this manner until the end of the simulation at 2.08Myr. Spiral arms get more distinct and develop cold dense H_2 rich clumps, which then fall into the center. The central hot region grows in size, while being devoid of H_2.

Halo 2 evolves in a similar fashion as halo 1, starting with a dense core which triggers atomic cooling at around ~0.575Myr after the rapid baryon collapse. At first the $10^4 K$ region is very small, however, after another dense clump falls into the center at ~0.7Myr its size receives a substantial boost. Cooling with temperatures of $10^4 K$ dominates the central part with H_2 cooling around it, embedded in a hot medium as is shown in figure 4.4. As time evolves more gas fragments along the spiral arms and falls into the hot center. Those fragments, as can be seen in picture two and three of the middle panel in figure 4.4, vary between being cold, dense and hot, H_2 poor. The clumps display the same trend as the center, a H_2 bare area developing close to the hot central region. Halo 2 shows more fragmentation along spiral arms than halo 1, yet not as much as halo 8. This scenario persist until the end of the simulation at 2.83Myr.

Halo 8 is the first of the sample that undergoes rapid baryon collapse, at $z \sim 20.89$. The central dense clump collapses as nearby another dense clump is forming at ~0.2Myr. This clump spirals around the center and gets accreted shortly after, at $\sim$ 0.25Myr. However, earlier at ~0.23Myr when the clump is close by the central region, yet not fully swallowed, atomic cooling is triggered. In addition, around this time a H_2 poor region around the center develops. For this halo the H_2 void is especially pronounced, a H_2 void ringed by cold, dense H_2 gas. Larger fragments also show this behaviour. This picture persist until the end of the simulation at 2.18Myr with the shape of the material outside the H_2 void slightly changing due to the spiral arms and angular momentum. Halo 8 shows more fragmentation than the previous haloes, which showcases itself in a clumpier accretion mode. Snapshots of the simulation regarding halo 8 can be seen in figure 4.5.

Atomic cooling in halo 12 is triggered at $\sim 0.253 Myr$ after catastrophic baryon collapse. Shortly after at $\sim 0.417 Myr$, a second clump that cools at 10^4K falls into the main disk, expanding the atomically cooling center. At $\sim 0.592 Myr$ a third, very dense and hot clump merges with the main disk. Subsequently, more and more clumps fall into the center with time, some being hot, close to 10^4K, while others have temperatures between 10^2K and 10^3K. Some fragments orbit the main disk several times before being accreted, coming close to the center before being ejected into another round-about. This is illustrated in the middle row of figure 4.6, which captures the moment of a clump coming close to the center before being send on another rotation. A remarkably dense and hot clump fly's by the main disk at $\sim 2.6 Myr$ before merging with it at $\sim 2.74 Myr$, causing massive turbulence that ejects material in tidal tails outwards. This turbulence further boosts the formation of H_2 and very cold spiral arms, that can be still seen in the third row of figure 4.6. The center of halo 12 shows a similar cooling mode as the other haloes, where a small, hot 10^4K Lyα cooled bubble of H_2 devoid gas is surrounded by a cooler H_2 self-shielded 10^3K environment. The hot region is distinguished by its low H_2 fraction, which is in agreement with density, temperature, and H_2-fraction plots.
Halo 16 starts cooling though the channels of Lyα in its center at $\sim$ 0.237Myr. The atomically cooling region expands slowly and at $\sim$ 0.431Myr another clump crashes into it, after forming at a distance of $\sim$ 1pc for about 100Myr. Halo 16 proceeds to evolve due to turbulent flows without as much clumpy accretion and fragmentation as halo 8 or halo 12, accreting cooler clumps of temperatures between 10^2K to 10^3K. Fragmentation increases with time, where at $\sim$ 2.26K a hot clump merges with the main disk. The clump formed at $\sim$ 1.88Myr orbits the center until finally crashing into it, which can be seen in the middle row of figure 4.7. Halo 16 exhibits distinct spiral arms that harbor H_2, which is showcased by cold temperatures like in the last column of figure 4.7. It further depicts the scenario of a H_2 devoid core, surrounded by colder, H_2 gas that sits in an environment of atomically cooled gas.
Halo 19 is the last of our sample to undergo catastrophic baryon collapse at z = 14.11. Atomic cooling is triggered in its central core at $\sim$ 0.57Myr. The disk of halo 19 is prone to fragmentation, accretion therefore proceeds in a clumpy manner. Bigger and smaller clumps are accreted by the center, with some of them reaching temperatures of 10^4K in their cores. This is in agreement with pictures of the H_2-fraction, as hot Lyα cooled regions are almost devoid of H_2. Some bigger clumps fall into the center at 0.717 Myr, and at 1.36 Myr. Around 2.08 Myr a clump forms in the vicinity of the central disk and proceeds to orbit it. At $\sim$ 2.31 Myr the clump completes a flyby accompanied by mass exchange, which places its orbit closer to the disk until it is fully accreted at 2.42 Myr. Subsequently, the disk is rattled by turbulence that triggers H_2 cooling in the spiral arms and ejects material in tidal waves outwards. This is depicted in the middle column of figure 4.8, were cold, H_2 rich regions are blue in the temperature plot. Afterwards, the disk stabilizes a little and other fragments start to fall in again. Another hot, big clump that orbits the main core and performs close flybys forms at roughly 3.07 Myr, continuing its revolution until the end of our simulation at 3.39 Myr. Spiral arms seem to form somewhat later than for the other haloes at around 0.678Myr, which can be seen in the first column of figure 4.8. It furthermore shows the scenario of a central H_2 poor region, surrounded by a denser H_2 rich gas that is embedded in a Lyα cooled medium.

Disk evolution for halo 20 is showcased in figure 4.9. Atomic cooling in its central core is triggered at ~ 0.54 Myr. Initial stages resemble those of halo 8, where a filamentary structure is present, enabling clumps of various sizes to migrate onto the central clump and for relatively smooth mass accretion. The accretion of big, hot clumps leads to turbulence induced H_2 cooling in spiral arms, as well as mass ejection in tidal waves. This is depicted through the cold, blue regions in the middle panel of figure 4.9. After a massive clump crashes onto the center at ~ 1.67 Myr, accretion proceeds in a clumpy manner until the end of the simulation at 3.09 Myr. The central core of halo 20 displays the same trend as the other simulated haloes, namely a hot atomically cooled core surrounded by cooler H_2 rich gas that again is embedded in a hot 10^4K medium. H_2-fraction plots support this idea, demonstrating a clear H_2 void corresponding to a hot Lyα cooled region in the central core.

Some haloes, (e.g. halo 10), form multiple disks that survive for long enough times before merging with the central core to potentially form supermassive binaries. Whether these smaller systems would be able to cool enough to form stars is unclear, as it would require a higher resolution than has been enforced here.

All simulated haloes further show the trend of turbulence enhancing local densities. These in turn boost H_2 formation and cooling through the channels of H^- and H_2^+, which can be seen as cool regions in the temperature plots around the disks where most turbulence occurs. Although implementing a high LW background of $10^5 J_{21}$, H_2 preserves in all haloes, setting a limit to the efficiency of atomic cooling. This is affirmed by the H_2 fraction plots that depict the evolution of H_2. Higher densities coincide with higher H_2 fractions and the denser the medium gets, the more it self-shields against external radiation, cooling it down to ~ 100 - 200K with the exception of the Lyα cooling central cores that are almost devoid of H_2. This is also showcased in the 1D-Profile plots in figures B.5, B.6, and B.7, were the H_2-fraction is calculated against the radius for three different timesteps. The first timestep is the onset of catastrophic baryon collapse, followed by the start of atomic cooling in the central core, and lastly figure B.7 displays the fractions at the end of each halos simulation. They rise with time to up to 10^{-2} for halo 8 and halo 16, otherwise staying in the range of $10^{-4} - 10^{-3}$. Figures of the onset of Lyα cooling depict yet again the trend, of a hot central core as the graphs exhibit a dip there and rise towards larger radii. Subfigure B.7 (e) shows an interesting dip at 10^{-1} pc, which is consistent with figure 4.7 as halo 16 has at that distance hot atomically cooling companion clumps.

4.3 Accretion Rates

The accretion rate defined here is the change in mass from output to output divided by the time between outputs. Therefore, accretion rates are calculated by centering a sphere with a radius of 0.136pc on the densest cell at the center of the halo disk. The mass in a 0.136pc sphere is calculated for each data output and then divided by 10kyr, which is the time of the output intervals, to get the dimension of $\mathrm{M}_{\odot} yr^{-1}$. A radius of 0.136pc was chosen in order to keep the approximated sphere resolved by at least 10 cells and to exclude mass from spiral arms, as their artificial input would falsify the rates. Initial time t = 0.0 is defined as the time of the onset of the rapid gas collapse when the densest cell of the simulation reaches the maximum refinement level 15 for the first time. Accretion rates are displayed in Figure 4.10 and summarized for their

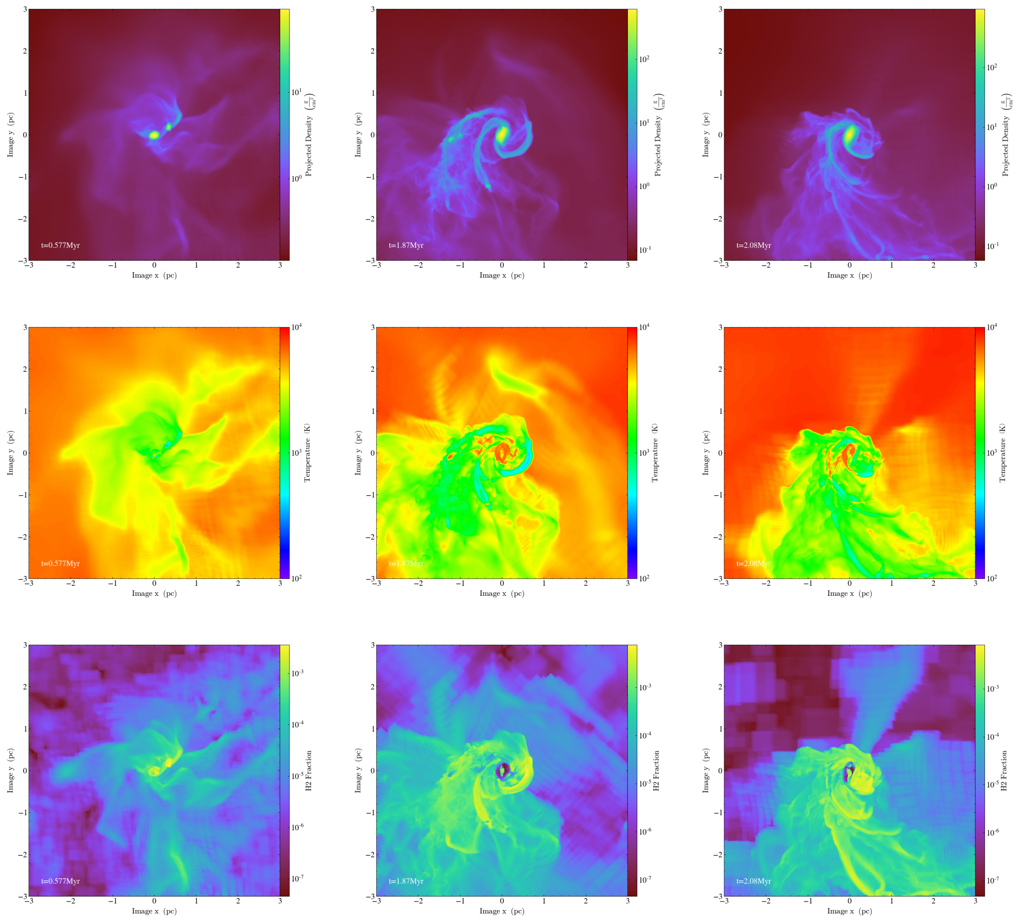

Figure 4.3: Snapshots of the evolution of the disk in halo 1 in a LW background of $10^5 J_{21}$. The top row displays the projected densities at 0.577Myr (left), 1.87Myr (middle) and at 2.08Myr (right) after the onset of atomic cooling. In the middle panel the temperatures corresponding to the densities are shown and in the bottom row the H_2 mass fractions. Snapshots are 6pc in diameter.

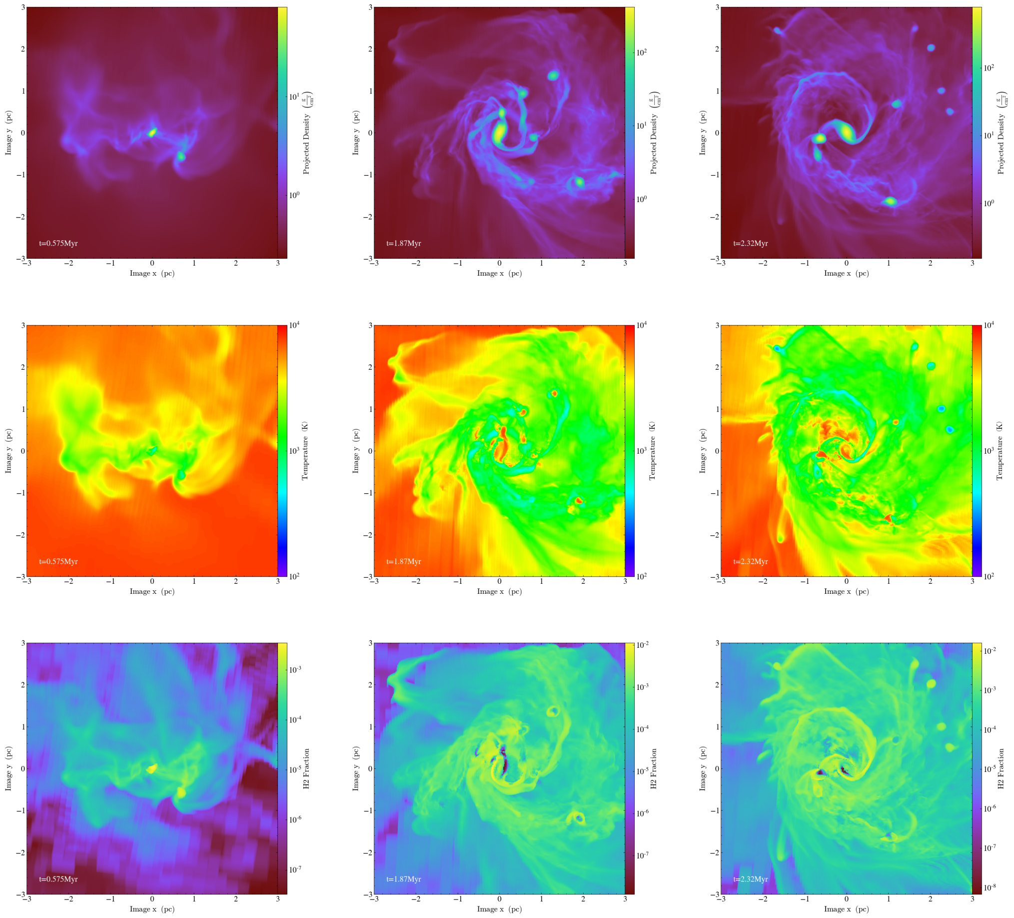

Figure 4.4: Snapshots of the evolution of the disk in halo 2 in a LW background of $10^5 J_{21}$. The top row displays the projected densities at 0.575Myr (left), 1.87Myr (middle) and at 2.32Myr (right) after the onset of atomic cooling. In the middle panel the temperatures corresponding to the densities are shown and in the bottom row the H_2 mass fractions. Snapshots are 6pc in diameter.

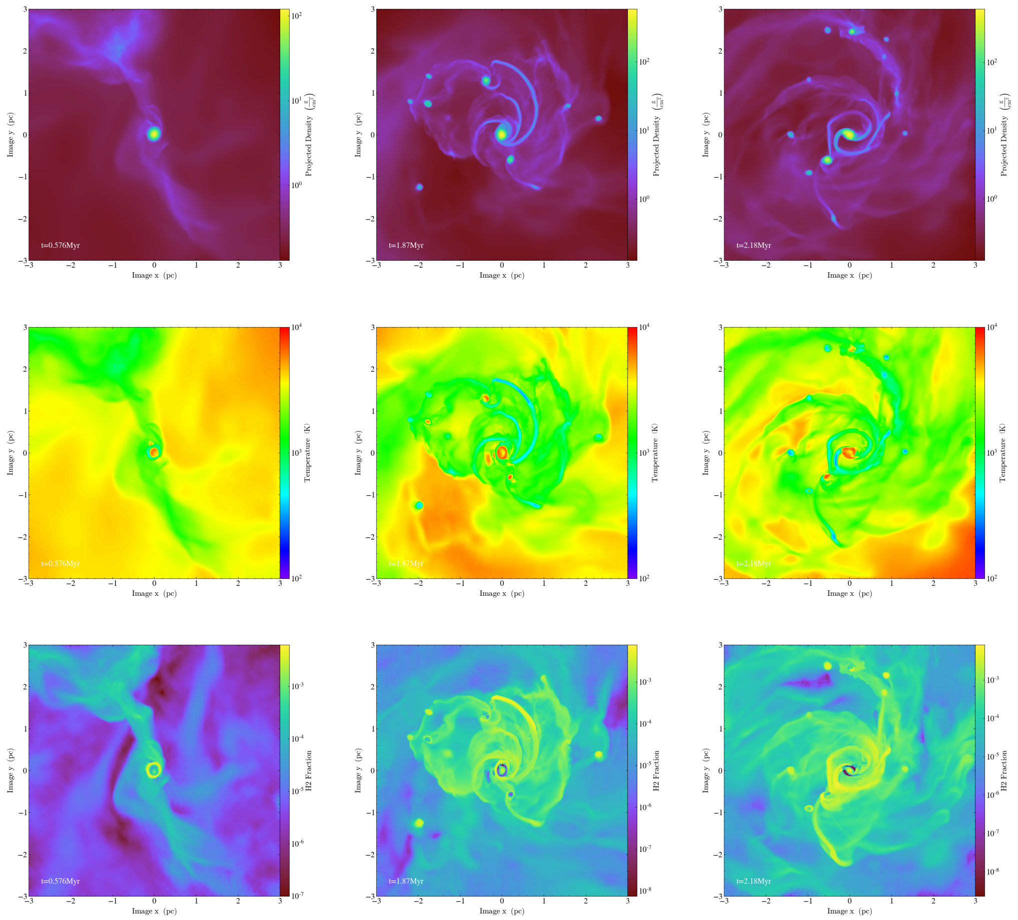

Figure 4.5: Snapshots of the evolution of the disk in halo 8 in a LW background of $10^5 J_{21}$. The top row displays the projected densities at 0.576Myr (left), 1.87Myr (middle) and at 2.18Myr (right) after the onset of atomic cooling. In the middle panel the temperatures corresponding to the densities are shown and in the bottom row the H_2 mass fractions. Snapshots are 6pc in diameter.

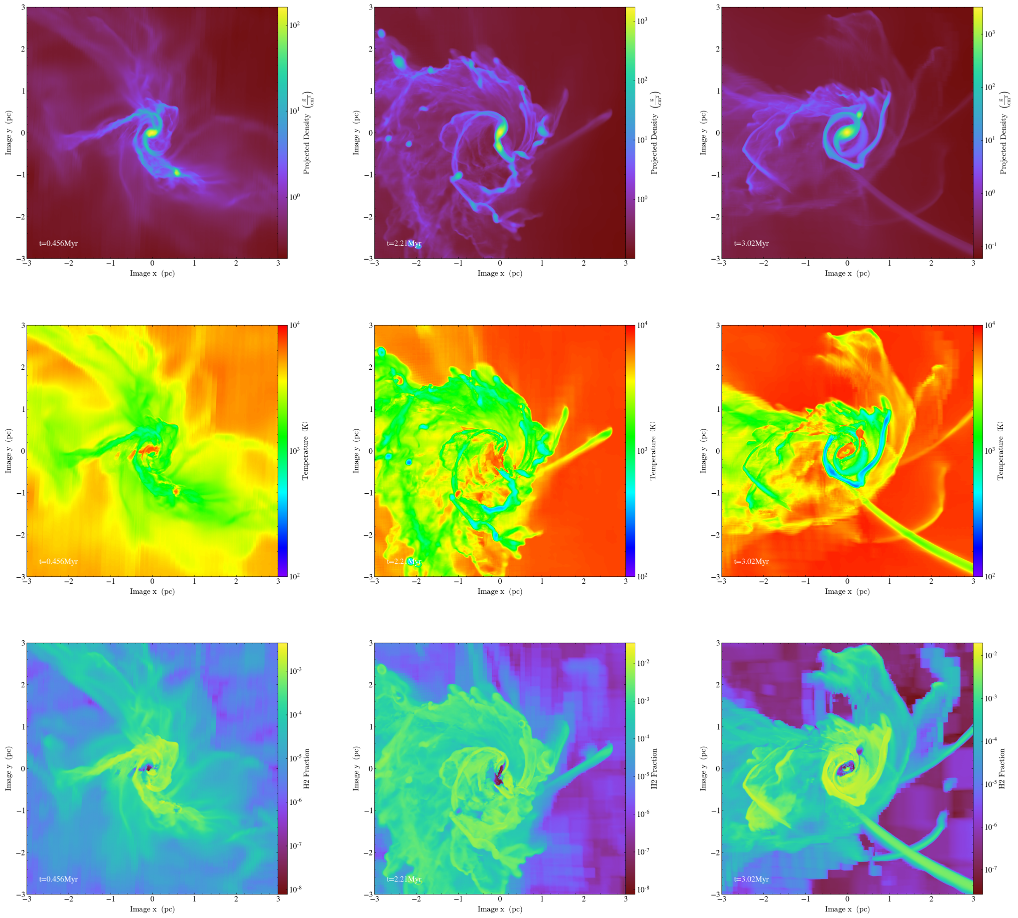

Figure 4.6: Snapshots of the evolution of the disk in halo 12 in a LW background of $10^5 J_{21}$. The top row displays the projected densities at 0.456Myr (left), 2.21Myr (middle) and at 3.02Myr (right) after the onset of atomic cooling. In the middle panel the temperatures corresponding to the densities are shown and in the bottom row the H_2 mass fractions. Snapshots are 6pc in diameter.

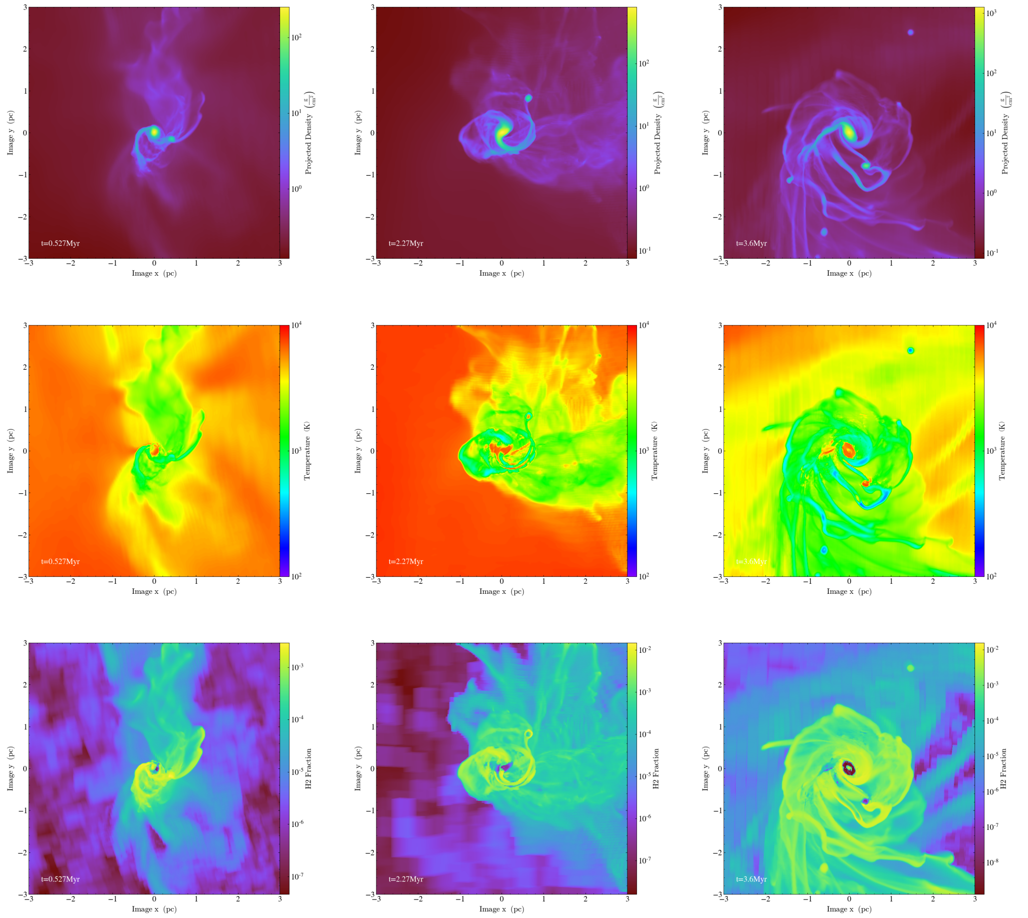

Figure 4.7: Snapshots of the evolution of the disk in halo 16 in a LW background of $10^5 J_{21}$. The top row displays the projected densities at 0.527Myr (left), 2.27Myr (middle) and at 3.6Myr (right) after the onset of atomic cooling. In the middle panel the temperatures corresponding to the densities are shown and in the bottom row the H_2 mass fractions. Snapshots are 6pc in diameter.

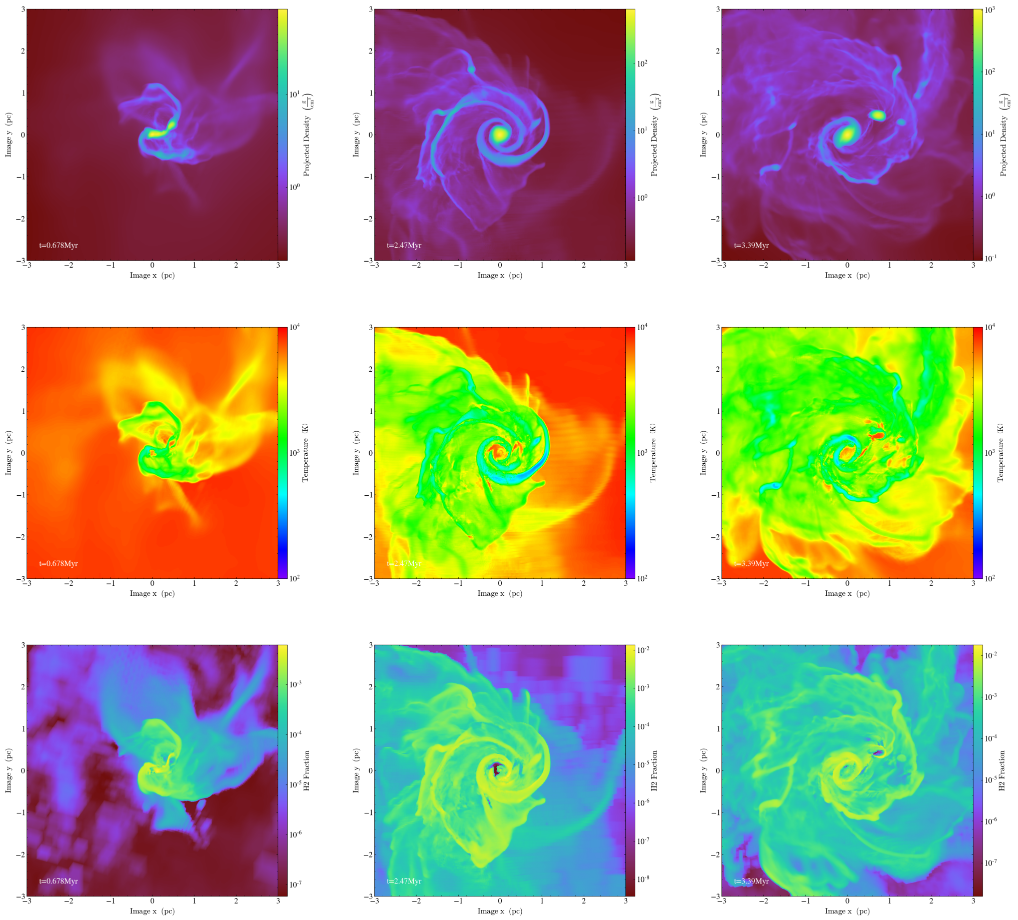

Figure 4.8: Snapshots of the evolution of the disk in halo 19 in a LW background of $10^5 J_{21}$. The top row displays the projected densities at 0.678Myr (left), 2.47Myr (middle) and at 3.39Myr (right) after the onset of atomic cooling. In the middle panel the temperatures corresponding to the densities are shown and in the bottom row the H_2 mass fractions. Snapshots are 6pc in diameter.

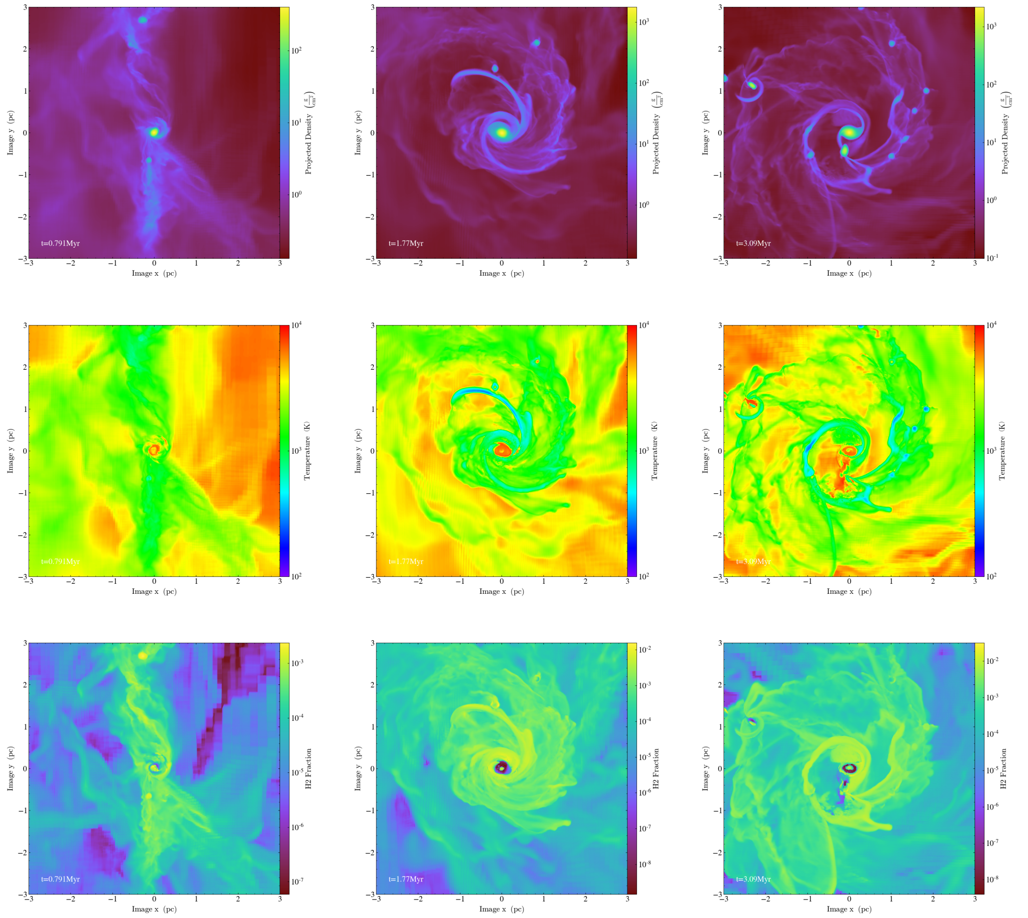

Figure 4.9: Snapshots of the evolution of the disk in halo 20 in a LW background of $10^5 J_{21}$. The top row displays the projected densities at 0.791Myr (left), 1.77Myr (middle) and at 3.09Myr (right) after the onset of atomic cooling. In the middle panel the temperatures corresponding to the densities are shown and in the bottom row the H_2 mass fractions. Snapshots are 6pc in diameter.

average, maximum, and minimum as well as for the total accumulated mass in table 4.2.
Each halo shows an initial jump in the accretion rate that corresponds to the formation of the dense core of the main disk, lasting for ~200 - 500 kyr. The initial jump is of order 0.05 - 0.075 $M_\odot yr^{-1}$ for halo 2, halo 8, and halo 16 and $\sim$ 0.02 $M_\odot yr^{-1}$ for halo 1, halo 12, and halo 19. These rates lie between the ones calculated by Patrick et al. (2020) for very high LW backgrounds without H_2 self-shielding, and for H_2 self-shielding in backgrounds of 10^2, 10^3, 10^4 J_{21} from Patrick et al. (2021). Patrick et al. (2020) found initial jump rates of $\sim$ 0.3 - 1 $M_\odot yr^{-1}$, whereas Patrick et al. (2021) found rates of order 0.003 - 0.06 $M_\odot yr^{-1}$. Furthermore, the formation of the core is faster than in lower LW backgrounds (500 - 750kyr; Patrick et al. (2021)), coinciding for some haloes with the timeline from pristine atomically cooled haloes (200 - 300kyr; Patrick et al. (2020)). Due to self-shielded H_2 in the halo cores and its less efficient cooling, rates never reach the efficiency of pristince Lyα cooling but manage to be way higher than for normal Pop III star formation in minihaloes. Once the core is formed, rates slightly fall as the disk stabilizes with the conservation of angular momentum. Accretion proceeds in a clumpy manner for halo 2, halo 8, halo 12, halo 19 and halo 20 due to fragmentation of the main disk and subsequent collision of those fragments with the center. Halo 1 and halo 16 display a smooth accretion mode, as fragmentation of the disk only slightly occurs and mostly towards higher evolution times. The rates have average values of 0.026 - 0.1 $M_\odot yr^{-1}$, with peaks reaching 0.18 - 0.59 $M_\odot yr^{-1}$ and as high as 1.78 $M_\odot yr^{-1}$ for halo 12. Yet again, these rates are between the calculated accretion rates of pristine atomically cooled haloes and normal Pop III forming minihaloes, cooling through the channels of H_2.
The accretion rate graph for halo 1 displays a steadily increasing slope, that is mostly due to turbulent motions. Its central core evolves as a dense, cold clump, cooling through H_2 at $\sim 10^2 - 10^3$K until atomic cooling is triggered at 0.47 Myr and causes the peak around 0.5 Myr in the accretion rate graph. That is followed by a small infalling clump, accompanied by another rise in the rate. At $\sim$ 1.84 Myr another atomically cooling fragment crashes into the center, causing more turbulence that ejects mass outwards and induces H_2 cooling in the spiral arms. Other than that, the peaks and dips in the accretion rate are due to episodes of smooth mass accretion.
Peaks in the accretion rate for halo 2 are mostly due to the accretion of small, hot clumps and from fragmentation of the disk and subsequent collisions of those fragments with the center. The central core starts to cool through Lyα at 0.575 Myr, coinciding with the first peak of the graph. It is followed by the stabilization of the disk and almost constant accretion as matter continues to smoothly fall into the center accompanied by smaller clumps. At 1.29 Myr a bigger atomically cooling clump crashes into the disk, causing the accretion rate to jump to roughly $0.2M_\odot yr^{-1}$. This peak is followed with a slightly larger peak at $\sim$ 1.7 Myr due to another hot fragment colliding with the center, subsequently resulting in a negative rate. Around 2.2 Myr a large dip followed by the maximum of $\sim 0.6M_\odot yr^{-1}$ is caused by a hot clump interacting with the center. The clump proceeds to orbit the center with a flyby and mass exchange responsible for the negative rate before completely merging at 2.34 Myr.
Halo 8 showcases a clumpy accretion history, with pronounced peaks and valleys in its rate graph. It starts to atomically cool at its core around 0.218 Myr and accretes at 0.257 Myr another atomically cooling clump, that ultimately leads to the initial peak in the accretion rate. The disk subsequently stabilizes due to conservation of angular momentum, resulting in a fall in the graph.

At 0.663 Myr a clump forms in a 2 pc distance, growing in mass and density so that Lyα cooling is triggered, before merging with the main core at 1.16 Myr. This is depicted in the accretion rate as the ~ 0.16 $M_\odot yr^{-1}$ maxima, followed by turbulent motions that induce H_2 formation and subsequent H_2 cooling in the spiral arms. Dips and slight rises before this event are due to the mass exchange between those two clumps. A third distinguished clump starts to form at 1.05 Myr and keeps orbiting the center, while reaching temperatures of 10^4K. Then at 1.71 Myr it performs a close flyby with a massive mass exchange with the central core, before falling into the disk at 1.81 Myr. The accretion rate at this point in time, therefore, displays two closely followed peaks, with the first one corresponding to the flyby and mass exchange, whereas the second maximum of 0.18 $M_\odot yr^{-1}$ is due to the complete accretion of the revolving clump. Thereafter, the center experiences turbulence and disk fragmentation that triggers H_2 cooling and mass ejection.

Halo 12 accretes at the beginning two smaller clumps, which correspond to the two small peaks in the accretion rate, followed by the accretion of a more massive clump that is responsible for the larger peak at around 0.592 Myr. Accretion proceeds smoother for the next 1 Myr as only small fragments fall into the center of the main disk. This changes at around 1.74 Myr as denser and more massive clumps start to crash into the main disk. At around 2.74 Myr a satellite, orbiting the main disk and cooling at 10^4K, causes mass exchange and a negative rate before crashing into the center with a peak value of ~ 1.78 $M_\odot yr^{-1}$. Turbulence caused due to this event ejects tidal tails outward, which are depicted in the negative accretion rate and figure 4.6. Subsequently, the disk starts to stabilize again, resulting in positive rates.

The initial dense core of halo 16 forms at ~ 0.237 Myr after the catastrophic baryon collapse, when atomic cooling is triggered and which corresponds to the first small peak in the accretion rate graph. This small peak is followed by a slight dip and another peak, that is due to a small fragments being accreted at 0.556 Myr. Smooth mass accretion is then the dominant process in the evolution of halo 16, with modest contributions from accreted disk fragments. The maximum in halo 16s accretion rate plot at around 2.26 Myr arises from the accretion of a clump that managed to reach high enough temperatures to trigger Lyα cooling. It forms at ~ 1.87 Myr close to the center and proceeds to orbit the disk. That causes mass exchange between the two, resulting in negative accretion rates, before being completely accreted. After 2.8 Myr disk fragmentation occurs more frequently, causing more and more fragments to subsequently fall into the center. Close to the end of the simulation at 3.4 Myr, a large fragment crashes into the disk. It triggers turbulent motions, a peak in H_2 cooling in the spiral arms, and induces ejection of mass from the center before the disk is able to stabilize again.

Halo 19 exhibits a clumpy accretion mode. The first rise of the accretion rate at ~ 0.5 Myr depicts the start of Lyα cooling in its center, followed by a larger peak at around 0.717 Myr that is due to a larger clump being accreted. This is followed by the accretion of two bigger clumps at 0.929 Myr and 1.36 Myr interspersed with infalling smaller fragments. Around 2.08 Myr after the start of the catastrophic baryon collapse, a clump forms close to the main disk and proceeds to evolve, while orbiting the center. It performs a flyby with mass exchange at ~ 2.31 Myr, which is depicted as a dip in the accretion rate and that subsequently puts it into closer orbit. The hot 10^4 K satellite merges with the center at 2.42 Myr, which is preceded by a mass exchange and negative accretion rate. Once it falls into the center, causing the peak in the rate, it triggers turbulence and mass ejection that is showcased in a negative rate. Subsequently, the main disk stabilizes again for a short period of time, before it accretes another big clump at 2.97 Myr, producing the maximum and minimum of halo 16. That event is foreshadowed by yet another close flyby with a massive mass exchange and followed by H_2 inducing turbulence accompanied by mass ejection in tidal tales. Halo 16 afterwards produces another interacting satellite, that orbits the main disk until the end of our simulation at 3.39 Myr.

Halo 20 displays a clumpy accretion mode, that is driven by a mixture of small, cold and big, hot infalling clumps. The first rise of the rate in figure 4.10 at $\sim$ 0.5 Myr is due to the start of central Lyα cooling, shortly followed by the accretion of smaller clumps. A filamentary structure allows for other clumps to migrate onto the central core, producing the two big spikes in halo 20 rate plot. The first big spike located at $\sim$ 1.23 Myr arises from a 10^4 K hot clump first interacting with the main clump before merging with it. Subsequently, at around 1.67 Myr another hot, big clump travels through the filament towards the main center and is shortly after accreted, causing the maximum of 1 $\mathrm{M}_{\odot} yr^{-1}$ and subsequent trubulence with slight mass ejection. Halo 20 proceeds, until the end of our simulation at 3.09 Myr, to accrete only small fragments, leading to a small rise in its rate.

Figure 4.10 shows negative accretion rates for almost all haloes. They arise from mass exchange with other disks during close encounters or are due to gas being ejected out of the center by turbulence. A star forming in the center of the disk, however, would only experience a temporary stop in its accretion flow as the gas stripping occurs on much larger scales. Accretion rates computed here are in good agreement with previous studies of high and intermediate LW backgrounds (e.g. Patrick et al. (2020, 2021); Regan and Downes (2018a); Suazo et al. (2019)). They walk the edge between hybrid H_2 cooling and pristine atomic cooling. Dominated by central Lyα cooling at 10^4 K, a limit is set to the accretion rate as H_2 is able to survive in all runs and hinders them from reaching values as high as for pristine atomic cooling haloes, which show average rates of $\sim$ 0.1 - 0.5 $\mathrm{M}_{\odot} yr^{-1}$ and can peak up to 2 $\mathrm{M}_{\odot} yr^{-1}$ (Patrick et al. (2020)). Yet, central accretion rates are about 10 to 100 times higher than for LW backgrounds of $10^2 J_{21}$, $10^3 J_{21}$, and $10^4 J_{21}$ from Patrick et al. (2021). In summary, accretion is driven through atomic cooling with an upper limit set due to self-shielded H_2 in the center.

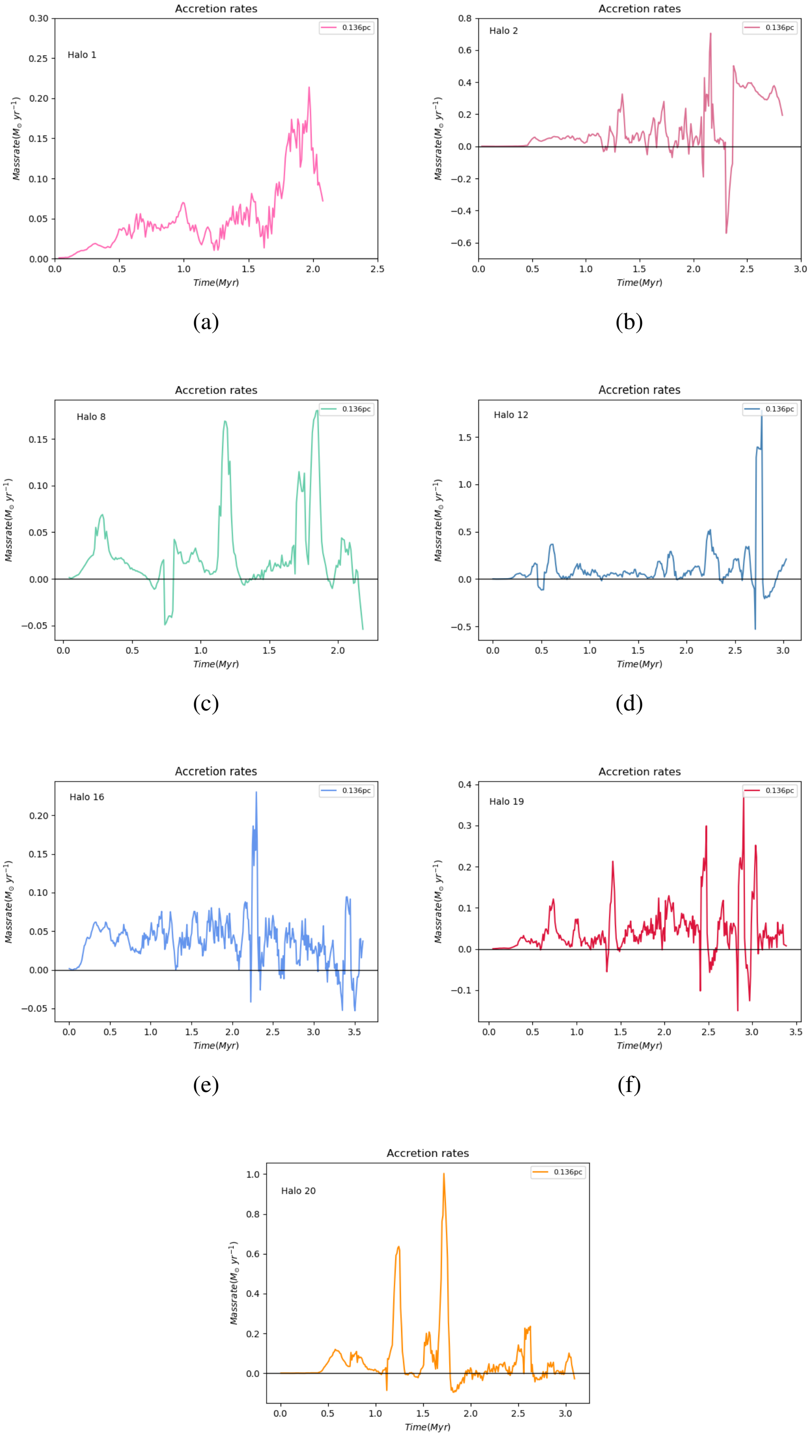

(a) (b) (c) (d) (e) (f) (g)

Figure 4.10: Accretion rates for all simulated haloes in a $10^5 J_{21}$ LW background. Rates are calculated with regard to the center of the main disk, displaying halo 1 in (a), halo 2 in (b), halo 8 in (c), halo 12 in (d), halo 16 in (e), halo 19 in (f), and halo 20 in (g).

4.3.1 Accreted Mass

Figure 4.11 displays the total accumulated mass over time for the central 0.136 pc of the designated haloes. The total accreted mass lies in the range between 0.5 - 3 $\times 10^5$ $M_\odot$, which is consistent with the results of Patrick et al. (2020) and Patrick et al. (2021), coming closer to the rates of pristine atomically cooled haloes than to those of cooling predominantly through H_2. They are about 10 times greater than the rates calculated by Patrick et al. (2021) for smaller LW backgrounds and about 2 times smaller than those in Patrick et al. (2020) for pristine atomic cooling. Graphs further yield similar results to the accretion rates, highlighting individual halo evolution. Highest peaks from figure 4.10 coincide with steep increases in the accumulated masses of figure 4.11 and occasional dips equal negative accretion rates. Halo 1 and halo 16 depict smooth, constant mass accumulation as is likewise the case for their accretion mode. Halo 16, halo 19, and halo 20s graphs show a left falling orientation towards the end of the simulation with a flattening in its slope. The other haloes display a preference for a right rising orientation. Non of them seem to have reached their accretion limit, which is the case in the LW backgrounds of $10^2 J_{21}$, $10^3 J_{21}$, and $10^4 J_{21}$ from Patrick et al. (2021). Halo 8 and halo 20 depict a highly unruly evolution in mass, which corresponds to their clumpy accretion process, with several mass exchanges. Note worthy is further the dip and jump in halo 12s graph at around 2.7 Myr. It matches the negative accretion rate at this point, due to mass exchange and the subsequent accretion of the clump, followed by another dip caused by the ejection of mass. Halo 19 likewise depicts its highest accretion peaks in small increased bumps in the accumulated mass graph. Halo 20s distinct jumps and bumps further correspond to it's accretion history of hot, dense clumps and staggering phases of mass increase, when only accreting smaller fragments.

Simulations were run for at least 2.08 Myr and up to 5 Myrs, making sure that haloes build up masses of several 10^5 $M_\odot$. This covers the evolution of normal Pop III stars with masses of $10^3 - 10^4$ $M_\odot$ and lifetimes of ≤ 2 Myr, as well as more massive and supermassive stars as they have shorter lifespans. The simulations follow central accretion rates beyond the stars progression into BHs. Stars born in environments with accretion rates ≥ 0.04 $M_\odot yr^{-1}$ (Woods et al. (2017)) are found to directly collapse into BHs through the GR instability during central H-burning. Accretion rates below that fuel stars that collapse after the depletion of hydrogen or helium.

Stars with infall rates below ~ 0.02 $M_\odot yr^{-1}$ (Herrington et al. (2022); Haemmerlé et al. (2018)) are predicted by stellar evolution codes to produce compact, blue supergiants. Those hot, blue stars could ionize the surrounding medium and hamper subsequent accretion (Latif et al. (2021)). In comparison, infall rates of 0.1 - 1.0 $M_\odot yr^{-1}$ are thought to produce cool, red SMS. Haloes exposed to LW backgrounds of $10^5 J_{21}$ and average accretion rates of 0.026 - 0.1 $M_\odot yr^{-1}$, like in this study, would most likely produce both, compact, blue supergiants and cool, red SMS of a few tens of thousands to hundred thousands $M_\odot$ (Woods et al. (2017)).

4.3.2 Multiple Systems

All simulated haloes display some sort of fragmentation and companion clumps or satellites. Throughout the simulation those clumps will, after a certain amount of time, crash into the center or get torn apart. Massive satellites tend to interact with the main disk through mass exchanges that are depicted as negative accretion rates in figure 4.10. Furthermore, the most

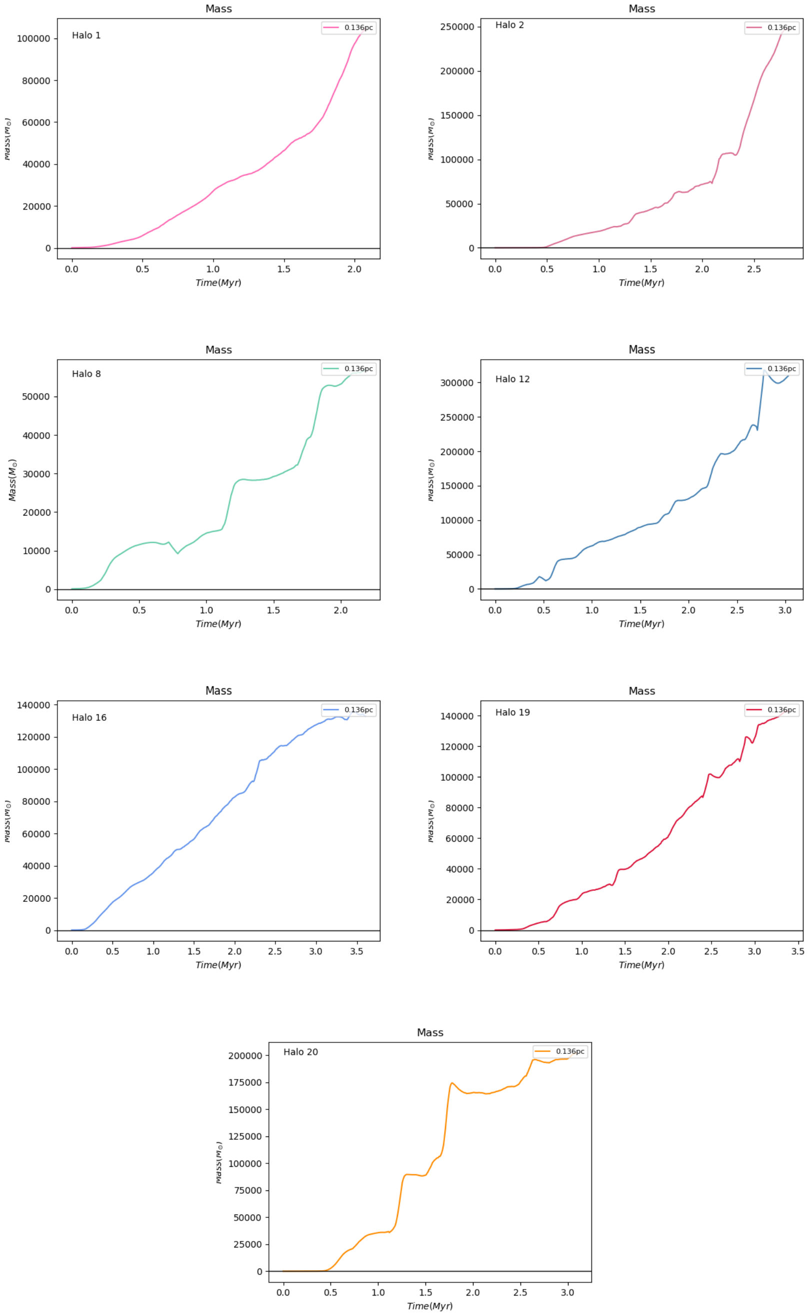

Figure 4.11: Accreted masses for all simulated haloes in a $10^5 J_{21}$ LW background. Masses are calculated with regard to the center of the main disk and observed for the whole simulation,displaying halo 1 in (a), halo 2 in (b), halo 8 in (c), halo 12 in (d), halo 16 in (e), halo 19 in (f), and halo 20 in (g).

massive companions eventually trigger temperatures of $10^4 K$ in their centers. Their lifetimes vary between 0.15 Myr and up to 1 Myr, long enough for stars to potentially form in them and form binaries or multiples. However, the simulations resolution is not high enough to capture whether cooling would be able to form stars inside them.

	Mean ($M_\odot yr^{-1}$)	**Max** ($M_\odot yr^{-1}$)	**Min** ($M_\odot yr^{-1}$)	M_{tot} ($M_\odot$)
Halo 1	0.05	0.21	0.00095	1×10^5
Halo 2	0.086	0.589	-0.153	2.5×10^5
Halo 8	0.026	0.18	-0.054	0.56×10^5
Halo 12	0.1	1.78	-0.53	3×10^5
Halo 16	0.037	0.23	-0.053	1.3×10^5
Halo 19	0.042	0.38	-0.15	1.4×10^5
Halo 20	0.065	1.00	-0.096	2×10^5

Table 4.2: Detailed Accretion rate and accumulated Mass table for the simulated haloes. The table features the average accretion rate, maximum, and minimum value for each halo as well as the total accumulated mass M_{tot} at the end of the run for a 0.136 pc sphere.

Chapter 5

Conclusio

Our Simulations were run for 2.08 - 5 Myr, long enough times to allow for the formation, evolution, and death of a star. SMS are found to have lower lifetime thresholds of ~ 30 - 100 kyr for extreme accretion rates in pristine atomically cooled haloes and typical values of ~ 1 - 2 Myr for lower rates (Woods et al. (2020)).
Haloes subjected to external UV fluxes are able to grow to higher masses and temperatures compared to normal Pop III star forming minihaloes, before collapsing. This study of a $10^5 J_{21}$ LW background with enabled H_2 self-shielding shows, that H_2 is able to self-shield even against the strongest external UV radiation. It survives in halo centers embedded in hot 10^4K gas, growing in density with time and surrounding a hot, atomically cooling core. This hybrid cooling mode sets an upper limit for the accretion rates compared to pristine Lyα cooled haloes, as H_2 cooling is more efficient, while still being way higher than in normal Pop III star forming minihaloes or in intermediate LW backgrounds.
Patrick et al. (2020) found for high LW backgrounds without enabled self-shielding average accretion rates of 0.1 - 0.5 $M_{\odot} yr^{-1}$ with peaks of up to 2 $M_{\odot} yr^{-1}$, whereas the $10^2 J_{21}$, $10^3 J_{21}$, and $10^4 J_{21}$ backgrounds from Patrick et al. (2021) yield average rates of a few $10^{-3} - 10^{-2}$ $M_{\odot} yr^{-1}$. Our simulations found average values of 0.026 - 0.1 $M_{\odot} yr^{-1}$ with peaks of up to 1.78 $M_{\odot} yr^{-1}$. The total accumulated masses inside the 0.136 pc tally sphere lie between 0.5 - 3 $\times 10^5 M_{\odot}$, leading to the formation of two types of stars. Lower accretion rates of up to ≤ 0.02 $M_{\odot} yr^{-1}$ form stars that evolve as compact, blue supergiants that are able to ionize the surrounding medium and hamper accretion. To account for such an event, calculations of radiative transport including stellar feedback have to be carried out, otherwise overestimating accretion rates and/or stellar masses. Overestimation's may, however, be slight ones as our rates are consistent with Latif et al. (2020), who performed simulations with implemented radiative transfer calculations. The second type of Pop III stars to form are cool, red SMS with accretion rates of 0.1 - 1.0 $M_{\odot} yr^{-1}$, which do not reach temperatures high enough to alter their accretion history. Their masses are therefore self-consistent, as the stars would not be able to produce sufficient ionizing UV flux that could suppress accretion (Latif et al. (2021)).
Comparing our final masses and accretion rates to values from Woods et al. (2017) and Woods et al. (2020), we estimate that stars accreting at rates of ≥ 0.04 $M_{\odot} yr^{-1}$ will collapse through the GR instabillity during hydrogen burning into DCBHs, while rates below that will drive collapse

through the photodisintegration instability (Heger and Woosley (2002)) or hydrogen exhaustion. Subsequently, those may be the seeds for less luminous, intermediate mass quasars rather than the most massive SMBH that reach 10^9 $M_\odot$ by z ≥ 6 - 7, as Smidt et al. (2018) found that their seeds have to be ≥ 10^5 $M_\odot$ by z ∼ 20. Yet, the DCBH, Pop III VMS and Pop III SMS formation rate is plagued by large uncertainties making it quite difficult to estimate their likelihood (Valiante et al. (2017)). Moreover, less luminous and massive primordial quasars are awaiting their discovery.

However, since our values yet again walk the edge between several scenarios, it is important to note that the here calculated rates should be taken as upper limits. As the main focus lay on self-consistent accretion flows for long enough times, resolution does not reach down to AU scales. Thus, calculations could potentially miss sub-fragmentation with inlying star formation in which case not all of the accreted mass falls onto one single star. Fragmentation in itself is most likely overestimated, as effects due to magnetic fields are not taken into account. Magnetic fields would be able to stabilize disks and thus quash fragmentation.

We furthermore show that the formation of binary and multiple SMS systems is indeed possible, for a variety of halo assembly histories. Almost all haloes show fragmentation and the development of companion clumps that after orbiting the main disk collide with its center. Satellites could potentially host stars, appearing both during the life time of the central massive star and its progression to a BH. Subsequently, this could lead to stellar collisions with the formation of more massive stars or the collision of DCBH and their resulting gravitational waves (GW). As was previously discussed, this result remains somewhat ambiguous as the resolution of this study is not high enough to capture sub-fragmentation on AU scales.

The probability of ground-based and/or space-based telescopes detecting stars in the mass range calculated in our simulations remains low. Although very massive, they are not bright enough to be observed with the wide fields of telescopes like the James Webb Space Telescope, the extremnely-large telescope (ELT), *Euclid*, or the Roman Space Telescope (RST), as Surace et al. (2018, 2019) showed that slightly more luminous stars are on the fringe of detectability at z ∼ 6 - 8. They further found that at higher redshifts SMS have a slim chance of being observed by JWST, if they are caught in its narrow field. Vikaeus et al. (2022) recently found that lensing by galaxy clusters and massive galaxies may extend the threshold for observability up to z ∼ 10 - 15 for the wide fields of JWST, *Euclid* and the RST. Since we expect the stars to end up collapsing into BHs, there would be no bright explosions to observe.

Environments hosting the formation of multiple stars around a central very massive or super massive star tend to be prone to tidal disruption events that produce near infrared (NIR) signatures, unique to those events and that could therefore be observed.

Our DCBHs themselves have a minimal chance of being detected by JWST, *Euclid* and RST, as yet again already way more massive DCBHS are barely observable even with a boost by lensing. The same applies to the radio range, leaving room for the detection of GW up to z ∼ 15 - 20 with the Laser Interferometry Space Antenna (LISA; Hartwig et al. (2018)) resulting from the earlier mentioned collisions between binaries. Since mergers of normal BHs occur at later times sporting different masses, GWs from our calculated DCBHS should be easily distinguishable. (Patrick et al. (2020, 2021))

In summary we conclude, that H_2 self-shields in the highest LW backgrounds, promoting hybrid H_2 - Lyα cooling in halo centers that is forging the way for yet undetected populations of lower mass DCBHs and SMS. Those could have been fairly common in the early Universe and therefore only await their detection. Although calculations show that observability today is unlikely, it leaves room for future technologies to do better and for hope to blossom for an eureka find.

List of Figures

Bibliography

T. Abel, P. Anninos, Y. Zhang, and M. L. Norman. Modeling primordial gas in numerical cosmology. New A, 2(3):181–207, Aug 1997. doi: 10.1016/S1384-1076(97)00010-9.

B. Agarwal. Primordial Gas Collapse in The Presence of Radiation: Direct Collapse Black Hole or Population III star? *arXiv e-prints*, art. arXiv:1807.08499, Jul 2018.

B. Agarwal, S. Khochfar, J. L. Johnson, E. Neistein, C. Dalla Vecchia, and M. Livio. Ubiquitous seeding of supermassive black holes by direct collapse. MNRAS, 425(4):2854–2871, Oct. 2012. doi: 10.1111/j.1365-2966.2012.21651.x.

B. Agarwal, B. Smith, S. Glover, P. Natarajan, and S. Khochfar. New constraints on direct collapse black hole formation in the early Universe. MNRAS, 459(4):4209–4217, Jul 2016. doi: 10.1093/mnras/stw929.

M. A. Alvarez, J. H. Wise, and T. Abel. Accretion onto the First Stellar-Mass Black Holes. ApJ, 701(2):L133–L137, Aug. 2009. doi: 10.1088/0004-637X/701/2/L133.

P. Anninos, Y. Zhang, T. Abel, and M. L. Norman. Cosmological hydrodynamics with multi-species chemistry and nonequilibrium ionization and cooling. New A, 2(3):209–224, Aug. 1997. doi: 10.1016/S1384-1076(97)00009-2.

E. Bañados, B. P. Venemans, C. Mazzucchelli, E. P. Farina, F. Walter, F. Wang, R. Decarli, D. Stern, X. Fan, F. B. Davies, J. F. Hennawi, R. A. Simcoe, M. L. Turner, H.-W. Rix, J. Yang, D. D. Kelson, G. C. Rudie, and J. M. Winters. An 800-million-solar-mass black hole in a significantly neutral Universe at a redshift of 7.5. Nature, 553(7689):473–476, Jan 2018. doi: 10.1038/nature25180.

H. Baumgardt and R. S. Klessen. The role of stellar collisions for the formation of massive stars. MNRAS, 413(3):1810–1818, May 2011. doi: 10.1111/j.1365-2966.2011.18258.x.

P. S. Behroozi, R. H. Wechsler, and H.-Y. Wu. The ROCKSTAR Phase-space Temporal Halo Finder and the Velocity Offsets of Cluster Cores. ApJ, 762(2):109, Jan. 2013. doi: 10.1088/0004-637X/762/2/109.

M. J. Berger and P. Colella. Local Adaptive Mesh Refinement for Shock Hydrodynamics. *Journal of Computational Physics*, 82(1):64–84, May 1989. doi: 10.1016/0021-9991(89)90035-1.

E. Bertschinger. Multiscale Gaussian Random Fields and Their Application to Cosmological Simulations. ApJS, 137(1):1–20, Nov. 2001. doi: 10.1086/322526.

V. Bromm, P. S. Coppi, and R. B. Larson. The Formation of the First Stars. I. The Primordial Star-forming Cloud. ApJ, 564(1):23–51, Jan 2002. doi: 10.1086/323947.

G. L. Bryan and M. L. Norman. A Hybrid AMR Application for Cosmology and Astrophysics. *arXiv e-prints*, art. astro-ph/9710187, Oct. 1997.

G. L. Bryan, M. L. Norman, J. M. Stone, R. Cen, and J. P. Ostriker. A piecewise parabolic method for cosmological hydrodynamics. *Computer Physics Communications*, 89(1-3):149–168, Aug. 1995. doi: 10.1016/0010-4655(94)00191-4.

G. L. Bryan, M. L. Norman, B. W. O'Shea, T. Abel, J. H. Wise, M. J. Turk, D. R. Reynolds, D. C. Collins, P. Wang, S. W. Skillman, B. Smith, R. P. Harkness, J. Bordner, J.-h. Kim, M. Kuhlen, H. Xu, N. Goldbaum, C. Hummels, A. G. Kritsuk, E. Tasker, S. Skory, C. M. Simpson, O. Hahn, J. S. Oishi, G. C. So, F. Zhao, R. Cen, Y. Li, and Enzo Collaboration. ENZO: An Adaptive Mesh Refinement Code for Astrophysics. ApJS, 211(2):19, Apr. 2014. doi: 10.1088/0067-0049/211/2/19.

J. S. Bullock, A. Dekel, T. S. Kolatt, A. V. Kravtsov, A. A. Klypin, C. Porciani, and J. R. Primack. A Universal Angular Momentum Profile for Galactic Halos. ApJ, 555(1):240–257, July 2001. doi: 10.1086/321477.

R. Cen, H. Kang, J. P. Ostriker, and D. Ryu. Background X-Ray Emission from Hot Gas in CDM and CDM+ Lambda Universes: Spectral Signatures. ApJ, 451:436, Oct. 1995. doi: 10.1086/176232.

S. Chandrasekhar. The Dynamical Instability of Gaseous Masses Approaching the Schwarzschild Limit in General Relativity. ApJ, 140:417, Aug. 1964. doi: 10.1086/147938.

S. Chon, T. Hosokawa, and N. Yoshida. Radiation hydrodynamics simulations of the formation of direct-collapse supermassive stellar systems. MNRAS, 475(3):4104–4121, Apr. 2018. doi: 10.1093/mnras/sty086.

P. C. Clark, S. C. O. Glover, and R. S. Klessen. TreeCol: a novel approach to estimating column densities in astrophysical simulations. MNRAS, 420(1):745–756, Feb. 2012. doi: 10.1111/j.1365-2966.2011.20087.x.

H. M. P. Couchman. Mesh-refined P 3M: A Fast Adaptive N-Body Algorithm. ApJ, 368:L23, Feb. 1991. doi: 10.1086/185939.

B. T. Draine and F. Bertoldi. Structure of Stationary Photodissociation Fronts. ApJ, 468:269, Sept. 1996. doi: 10.1086/177689.

G. Efstathiou, M. Davis, S. D. M. White, and C. S. Frenk. Numerical techniques for large cosmological N-body simulations. ApJS, 57:241–260, Feb. 1985. doi: 10.1086/191003.

G. J. Ferland, K. T. Korista, D. A. Verner, J. W. Ferguson, J. B. Kingdon, and E. M. Verner. CLOUDY 90: Numerical Simulation of Plasmas and Their Spectra. PASP, 110(749):761–778, July 1998. doi: 10.1086/316190.

G. J. Ferland, R. L. Porter, P. A. M. van Hoof, R. J. R. Williams, N. P. Abel, M. L. Lykins, G. Shaw, W. J. Henney, and P. C. Stancil. The 2013 Release of Cloudy. Rev. Mex. Astron & Astrophys, 49:137–163, Apr. 2013.

G. J. Ferland, M. Chatzikos, F. Guzmán, M. L. Lykins, P. A. M. van Hoof, R. J. R. Williams, N. P. Abel, N. R. Badnell, F. P. Keenan, R. L. Porter, and P. C. Stancil. The 2017 Release Cloudy. Rev. Mex. Astron & Astrophys, 53:385–438, Oct. 2017.

W. A. Fowler. Massive Stars, Relativistic Polytropes, and Gravitational Radiation. *Reviews of Modern Physics*, 36:545–554, Apr. 1964. doi: 10.1103/RevModPhys.36.545.

D. Galli and F. Palla. The chemistry of the early Universe. A&A, 335:403–420, Jul 1998.

S. C. O. Glover and T. Abel. Uncertainties in H_2 and HD chemistry and cooling and their role in early structure formation. MNRAS, 388(4):1627–1651, Aug. 2008. doi: 10.1111/j.1365-2966.2008.13224.x.

S. C. O. Glover and P. W. J. L. Brand. On the photodissociation of H_2 by the first stars. MNRAS, 321(3):385–397, Mar. 2001. doi: 10.1046/j.1365-8711.2001.03993.x.

S. C. O. Glover and M.-M. Mac Low. Simulating the Formation of Molecular Clouds. I. Slow Formation by Gravitational Collapse from Static Initial Conditions. ApJS, 169(2):239–268, Apr. 2007a. doi: 10.1086/512238.

S. C. O. Glover and M.-M. Mac Low. Simulating the Formation of Molecular Clouds. II. Rapid Formation from Turbulent Initial Conditions. ApJ, 659(2):1317–1337, Apr. 2007b. doi: 10.1086/512227.

N. Y. Gnedin, K. Tassis, and A. V. Kravtsov. Modeling Molecular Hydrogen and Star Formation in Cosmological Simulations. ApJ, 697(1):55–67, May 2009. doi: 10.1088/0004-637X/697/1/55.

F. Haardt and P. Madau. Radiative Transfer in a Clumpy Universe. II. The Ultraviolet Extragalactic Background. ApJ, 461:20, Apr. 1996. doi: 10.1086/177035.

L. Haemmerlé, T. E. Woods, R. S. Klessen, A. Heger, and D. J. Whalen. The evolution of supermassive Population III stars. MNRAS, 474:2757–2773, Feb. 2018. doi: 10.1093/mnras/stx2919.

O. Hahn and T. Abel. Multi-scale initial conditions for cosmological simulations. MNRAS, 415(3):2101–2121, Aug. 2011. doi: 10.1111/j.1365-2966.2011.18820.x.

Z. Haiman, M. J. Rees, and A. Loeb. Destruction of Molecular Hydrogen during Cosmological Reionization. ApJ, 476(2):458–463, Feb. 1997. doi: 10.1086/303647.

Z. Haiman, T. Abel, and M. J. Rees. The Radiative Feedback of the First Cosmological Objects. ApJ, 534(1):11–24, May 2000. doi: 10.1086/308723.

C. R. Harris, K. J. Millman, S. J. van der Walt, R. Gommers, P. Virtanen, D. Cournapeau, E. Wieser, J. Taylor, S. Berg, N. J. Smith, R. Kern, M. Picus, S. Hoyer, M. H. van Kerkwijk, M. Brett, A. Haldane, J. F. del Río, M. Wiebe, P. Peterson, P. Gérard-Marchant, K. Sheppard, T. Reddy, W. Weckesser, H. Abbasi, C. Gohlke, and T. E. Oliphant. Array programming with NumPy. *Nature*, 585(7825):357–362, Sept. 2020. doi: 10.1038/s41586-020-2649-2. URL `https://doi.org/10.1038/s41586-020-2649-2`.

T. Hartwig, S. C. O. Glover, R. S. Klessen, M. A. Latif, and M. Volonteri. How an improved implementation of H_2 self-shielding influences the formation of massive stars and black holes. MNRAS, 452(2):1233–1244, Sept. 2015. doi: 10.1093/mnras/stv1368.

T. Hartwig, B. Agarwal, and J. A. Regan. Gravitational wave signals from the first massive black hole seeds. *Monthly Notices of the Royal Astronomical Society: Letters*, 479(1):L23–L27, 05 2018. ISSN 1745-3925. doi: 10.1093/mnrasl/sly091. URL `https://doi.org/10.1093/mnrasl/sly091`.

A. Heger and S. E. Woosley. The Nucleosynthetic Signature of Population III. ApJ, 567(1): 532–543, Mar. 2002. doi: 10.1086/338487.

N. P. Herrington, D. J. Whalen, and T. E. Woods. Modeling Supermassive Primordial Stars with MESA. *arXiv e-prints*, art. arXiv:2208.00008, July 2022.

S. Hirano, T. Hosokawa, N. Yoshida, H. Umeda, K. Omukai, G. Chiaki, and H. W. Yorke. One Hundred First Stars: Protostellar Evolution and the Final Masses. ApJ, 781(2):60, Feb. 2014. doi: 10.1088/0004-637X/781/2/60.

S. Hirano, T. Hosokawa, N. Yoshida, K. Omukai, and H. W. Yorke. Primordial star formation under the influence of far ultraviolet radiation: 1540 cosmological haloes and the stellar mass distribution. MNRAS, 448(1):568–587, Mar. 2015. doi: 10.1093/mnras/stv044.

S. Hirano, T. Hosokawa, N. Yoshida, and R. Kuiper. Supersonic gas streams enhance the formation of massive black holes in the early universe. *Science*, 357:1375–1378, Sept. 2017. doi: 10.1126/science.aai9119.

R. W. Hockney and J. W. Eastwood. *Computer simulation using particles*. 1988.

T. Hosokawa, K. Omukai, and H. W. Yorke. Rapidly Accreting Supergiant Protostars: Embryos of Supermassive Black Holes? ApJ, 756(1):93, Sep 2012. doi: 10.1088/0004-637X/756/1/93.

T. Hosokawa, H. W. Yorke, K. Inayoshi, K. Omukai, and N. Yoshida. Formation of Primordial Supermassive Stars by Rapid Mass Accretion. ApJ, 778:178, Dec. 2013. doi: 10.1088/0004-637X/778/2/178.

J. D. Hunter. Matplotlib: A 2d graphics environment. *Computing in Science & Engineering*, 9(3): 90–95, 2007. doi: 10.1109/MCSE.2007.55.

J. Iben, Icko. Massive Stars in Quasi-Static Equlibrium. ApJ, 138:1090, Nov. 1963. doi: 10.1086/147708.

K. Inayoshi and K. Omukai. Supermassive black hole formation by cold accretion shocks in the first galaxies. MNRAS, 422:2539–2546, May 2012. doi: 10.1111/j.1365-2966.2012.20812.x.

J. L. Johnson and V. Bromm. The aftermath of the first stars: massive black holes. MNRAS, 374: 1557–1568, Feb. 2007. doi: 10.1111/j.1365-2966.2006.11275.x.

J. L. Johnson, V. C. Dalla, and S. Khochfar. The First Billion Years project: the impact of stellar radiation on the co-evolution of Populations II and III. MNRAS, 428:1857–1872, Jan. 2013a. doi: 10.1093/mnras/sts011.

J. L. Johnson, D. J. Whalen, H. Li, and D. E. Holz. Supermassive Seeds for Supermassive Black Holes. ApJ, 771:116, July 2013b. doi: 10.1088/0004-637X/771/2/116.

J. L. Johnson, D. J. Whalen, B. Agarwal, J.-P. Paardekooper, and S. Khochfar. The impact of reionization on the formation of supermassive black hole seeds. MNRAS, 445:686–693, Nov. 2014. doi: 10.1093/mnras/stu1676.

H. Katz, D. Sijacki, and M. G. Haehnelt. Seeding high-redshift QSOs by collisional runaway in primordial star clusters. MNRAS, 451(3):2352–2369, Aug. 2015. doi: 10.1093/mnras/stv1048.

T. Kitayama, N. Yoshida, H. Susa, and M. Umemura. The Structure and Evolution of Early Cosmological H II Regions. ApJ, 613(2):631–645, Oct. 2004. doi: 10.1086/423313.

M. R. Krumholz. Star Formation in Atomic Gas. ApJ, 759(1):9, Nov. 2012. doi: 10.1088/0004-637X/759/1/9.

M. A. Latif and S. Khochfar. Inception of a first quasar at cosmic dawn. MNRAS, 497(3): 3761–3769, Aug. 2020. doi: 10.1093/mnras/staa2218.

M. A. Latif, D. R. G. Schleicher, W. Schmidt, and J. Niemeyer. High-resolution studies of massive primordial haloes. MNRAS, 430(1):588–598, Mar. 2013a. doi: 10.1093/mnras/sts659.

M. A. Latif, D. R. G. Schleicher, W. Schmidt, and J. C. Niemeyer. The characteristic black hole mass resulting from direct collapse in the early Universe. MNRAS, 436(4):2989–2996, Dec. 2013b. doi: 10.1093/mnras/stt1786.

M. A. Latif, S. Bovino, C. Van Borm, T. Grassi, D. R. G. Schleicher, and M. Spaans. A UV flux constraint on the formation of direct collapse black holes. MNRAS, 443(3):1979–1987, Sep 2014a. doi: 10.1093/mnras/stu1230.

M. A. Latif, J. C. Niemeyer, and D. R. G. Schleicher. Impact of baryonic streaming velocities on the formation of supermassive black holes via direct collapse. MNRAS, 440(4):2969–2975, Jun 2014b. doi: 10.1093/mnras/stu489.

M. A. Latif, S. Bovino, T. Grassi, D. R. G. Schleicher, and M. Spaans. How realistic UV spectra and X-rays suppress the abundance of direct collapse black holes. MNRAS, 446:3163–3177, Jan. 2015. doi: 10.1093/mnras/stu2244.

M. A. Latif, K. Omukai, M. Habouzit, D. R. G. Schleicher, and M. Volonteri. Impact of Dust Cooling on Direct-collapse Black Hole Formation. ApJ, 823:40, May 2016. doi: 10.3847/0004-637X/823/1/40.

M. A. Latif, S. Khochfar, and D. Whalen. The Birth of Binary Direct-collapse Black Holes. ApJ, 892(1):L4, Mar. 2020. doi: 10.3847/2041-8213/ab7c61.

M. A. Latif, S. Khochfar, D. Schleicher, and D. J. Whalen. Radiation hydrodynamical simulations of the birth of intermediate-mass black holes in the first galaxies. MNRAS, 508(2):1756–1767, Dec. 2021. doi: 10.1093/mnras/stab2708.

M. A. Latif, D. J. Whalen, S. Khochfar, N. P. Herrington, and T. E. Woods. Turbulent cold flows gave birth to the first quasars. Nature, 607(7917):48–51, July 2022. doi: 10.1038/s41586-022-04813-y.

C. Leitherer, D. Schaerer, J. D. Goldader, R. M. G. Delgado, C. Robert, D. F. Kune, D. F. de Mello, D. Devost, and T. M. Heckman. Starburst99: Synthesis Models for Galaxies with Active Star Formation. ApJS, 123(1):3–40, July 1999. doi: 10.1086/313233.

S. Lepp and J. M. Shull. Molecules in the early universe. ApJ, 280:465–469, May 1984. doi: 10.1086/162013.

A. Loeb. The dark ages of the Universe. *Scientific American*, 295(5):5.46, Nov. 2006. doi: 10.1038/scientificamerican1106-46.

A. Loeb. *How Did the First Stars and Galaxies Form?*, chapter 4, page 64ff. 2010a.

A. Loeb. *How Did the First Stars and Galaxies Form?* 2010b.

M. E. Machacek, G. L. Bryan, and T. Abel. Simulations of Pregalactic Structure Formation with Radiative Feedback. ApJ, 548:509–521, Feb. 2001. doi: 10.1086/319014.

Y. Matsuoka, M. Onoue, N. Kashikawa, M. A. Strauss, K. Iwasawa, C.-H. Lee, M. Imanishi, T. Nagao, M. Akiyama, N. Asami, J. Bosch, H. Furusawa, T. Goto, J. E. Gunn, Y. Harikane, H. Ikeda, T. Izumi, T. Kawaguchi, N. Kato, S. Kikuta, K. Kohno, Y. Komiyama, S. Koyama, R. H. Lupton, T. Minezaki, S. Miyazaki, H. Murayama, M. Niida, A. J. Nishizawa, A. Noboriguchi, M. Oguri, Y. Ono, M. Ouchi, P. A. Price, H. Sameshima, A. Schulze, H. Shirakata, J. D. Silverman, N. Sugiyama, P. J. Tait, M. Takada, T. Takata, M. Tanaka, J.-J. Tang, Y. Toba, Y. Utsumi, S.-Y. Wang, and T. Yamashita. Discovery of the First Low-luminosity Quasar at z > 7. ApJ, 872(1):L2, Feb 2019. doi: 10.3847/2041-8213/ab0216.

M. R. C. McDowell. On the formation of H2 in H I regions. *The Observatory*, 81:240–243, Dec 1961.

I. D. McGreer and G. L. Bryan. The Impact of HD Cooling on the Formation of the First Stars. ApJ, 685(1):8–20, Sept. 2008. doi: 10.1086/590530.

T. Miyoshi and K. Kusano. A multi-state HLL approximate Riemann solver for ideal magnetohydrodynamics. *Journal of Computational Physics*, 208(1):315–344, Sept. 2005. doi: 10.1016/j.jcp.2005.02.017.

H. Mo, F. C. van den Bosch, and S. White. *Galaxy Formation and Evolution*, chapter 14.3, page 640ff. 2010a.

H. Mo, F. C. van den Bosch, and S. White. *Galaxy Formation and Evolution*. 2010b.

D. J. Mortlock, S. J. Warren, B. P. Venemans, M. Patel, P. C. Hewett, R. G. McMahon, C. Simpson, T. Theuns, E. A. Gonzáles-Solares, A. Adamson, S. Dye, N. C. Hambly, P. Hirst, M. J. Irwin, E. Kuiper, A. Lawrence, and H. J. A. Röttgering. A luminous quasar at a redshift of z = 7.085. Nature, 474(7353):616–619, Jun 2011. doi: 10.1038/nature10159.

S. P. Oh and Z. Haiman. Second-Generation Objects in the Universe: Radiative Cooling and Collapse of Halos with Virial Temperatures above 10^4 K. ApJ, 569(2):558–572, Apr. 2002. doi: 10.1086/339393.

K. Omukai. Primordial Star Formation under Far-Ultraviolet Radiation. ApJ, 546(2):635–651, Jan 2001. doi: 10.1086/318296.

K. Omukai and F. Palla. Formation of the First Stars by Accretion. ApJ, 589(2):677–687, June 2003. doi: 10.1086/374810.

B. W. O'Shea and M. L. Norman. Population III Star Formation in a ΛCDM Universe. I. The Effect of Formation Redshift and Environment on Protostellar Accretion Rate. ApJ, 654(1): 66–92, Jan 2007. doi: 10.1086/509250.

F. Pacucci, M. Volonteri, and A. Ferrara. The growth efficiency of high-redshift black holes. MNRAS, 452(2):1922–1933, Sept. 2015. doi: 10.1093/mnras/stv1465.

F. Palla, E. E. Salpeter, and S. W. Stahler. Primordial star formation - The role of molecular hydrogen. ApJ, 271:632–641, Aug 1983. doi: 10.1086/161231.

T. pandas development team. pandas-dev/pandas: Pandas, Feb. 2020. URL `https://doi.org/10.5281/zenodo.3509134`.

S. Patrick, D. J. Whalen, J. S. Elford, and M. Latif. MNRAS, in prep, 2021.

S. J. Patrick, D. J. Whalen, M. A. Latif, and J. S. Elford. The Collapse of Atomically-Cooled Primordial Haloes. I. High Lyman-Werner Backgrounds. *arXiv e-prints*, art. arXiv:2012.11612, Dec. 2020.

P. J. E. Peebles. Recombination of the Primeval Plasma. ApJ, 153:1, July 1968. doi: 10.1086/149628.

P. J. E. Peebles. Origin of the Angular Momentum of Galaxies. ApJ, 155:393, Feb. 1969. doi: 10.1086/149876.

F. I. Pelupessy, T. Di Matteo, and B. Ciardi. How Rapidly Do Supermassive Black Hole “Seeds” Grow at Early Times? ApJ, 665(1):107–119, Aug. 2007. doi: 10.1086/519235.

U.-L. Pen. Generating Cosmological Gaussian Random Fields. ApJ, 490(2):L127–L130, Dec. 1997. doi: 10.1086/311042.

Planck Collaboration. Planck 2015 results. XIII. Cosmological parameters. A&A, 594:A13, Sept. 2016. doi: 10.1051/0004-6361/201525830.

J. A. Regan and T. P. Downes. Rise of the first supermassive stars. MNRAS, 478(4):5037–5049, Aug. 2018a. doi: 10.1093/mnras/sty1289.

J. A. Regan and T. P. Downes. Fragmentation inside atomic cooling haloes exposed to Lyman-Werner radiation. MNRAS, 475:4636–4647, Apr. 2018b. doi: 10.1093/mnras/sty134.

J. A. Regan and M. G. Haehnelt. The formation of compact massive self-gravitating discs in metal-free haloes with virial temperatures of $\sim$13000-30000K. MNRAS, 393(3):858–871, Mar. 2009a. doi: 10.1111/j.1365-2966.2008.14088.x.

J. A. Regan and M. G. Haehnelt. Pathways to massive black holes and compact star clusters in pre-galactic dark matter haloes with virial temperatures $>\sim$10000K. MNRAS, 396(1):343–353, June 2009b. doi: 10.1111/j.1365-2966.2009.14579.x.

J. A. Regan, P. H. Johansson, and M. G. Haehnelt. Numerical resolution effects on simulations of massive black hole seeds. MNRAS, 439(1):1160–1175, Mar 2014. doi: 10.1093/mnras/stu068.

J. A. Regan, E. Visbal, J. H. Wise, Z. Haiman, P. H. Johansson, and G. L. Bryan. Rapid formation of massive black holes in close proximity to embryonic protogalaxies. *Nature Astronomy*, 1: 0075, Mar 2017. doi: 10.1038/s41550-017-0075.

J. A. Regan, J. H. Wise, B. W. O’Shea, and M. L. Norman. The emergence of the first star-free atomic cooling haloes in the Universe. MNRAS, 492(2):3021–3031, Feb. 2020a. doi: 10.1093/mnras/staa035.

J. A. Regan, J. H. Wise, T. E. Woods, T. P. Downes, B. W. O’Shea, and M. L. Norman. The Formation of Very Massive Stars in Early Galaxies and Implications for Intermediate Mass Black Holes. *The Open Journal of Astrophysics*, 3(1):15, Dec. 2020b. doi: 10.21105/astro.2008.08090.

B. Reinoso, D. R. G. Schleicher, M. Fellhauer, R. S. Klessen, and T. C. N. Boekholt. Collisions in primordial star clusters. Formation pathway for intermediate mass black holes. A&A, 614: A14, June 2018. doi: 10.1051/0004-6361/201732224.

A. J. Richings, J. Schaye, and B. D. Oppenheimer. Non-equilibrium chemistry and cooling in the diffuse interstellar medium - II. Shielded gas. MNRAS, 442(3):2780–2796, Aug. 2014. doi: 10.1093/mnras/stu1046.

M. Ricotti, N. Y. Gnedin, and J. M. Shull. Feedback from Galaxy Formation: Production and Photodissociation of Primordial H_2. ApJ, 560(2):580–591, Oct. 2001. doi: 10.1086/323051.

E. Ripamonti and T. Abel. Fragmentation and the formation of primordial protostars: the possible role of collision-induced emission. MNRAS, 348(3):1019–1034, Mar. 2004. doi: 10.1111/j.1365-2966.2004.07422.x.

Y. Sakurai, N. Yoshida, M. S. Fujii, and S. Hirano. Formation of intermediate-mass black holes through runaway collisions in the first star clusters. MNRAS, 472(2):1677–1684, Dec. 2017. doi: 10.1093/mnras/stx2044.

C. L. Sarazin and I. White, Raymond E. Steady State Cooling Flow Models for Normal Elliptical Galaxies. ApJ, 320:32, Sept. 1987. doi: 10.1086/165522.

D. Schaerer. The transition from Population III to normal galaxies: Lyalpha and He II emission and the ionising properties of high redshift starburst galaxies. A&A, 397:527–538, Jan 2003. doi: 10.1051/0004-6361:20021525.

A. T. P. Schauer, D. J. Whalen, S. C. O. Glover, and R. S. Klessen. Lyman-Werner UV escape fractions from primordial haloes. MNRAS, 454(3):2441–2450, Dec. 2015. doi: 10.1093/mnras/stv2117.

A. T. P. Schauer, B. Agarwal, S. C. O. Glover, R. S. Klessen, M. A. Latif, L. Mas-Ribas, C.-E. Rydberg, D. J. Whalen, and E. Zackrisson. Lyman-Werner escape fractions from the first galaxies. MNRAS, 467(2):2288–2300, May 2017. doi: 10.1093/mnras/stx264.

D. R. G. Schleicher, F. Palla, A. Ferrara, D. Galli, and M. Latif. Massive black hole factories: Supermassive and quasi-star formation in primordial halos. A&A, 558:A59, Oct. 2013. doi: 10.1051/0004-6361/201321949.

P. Schneider. *Einführung in die extragalaktische Astronomie und Kosmologie*. 2006.

C. Shang, G. L. Bryan, and Z. Haiman. Supermassive black hole formation by direct collapse: keeping protogalactic gas H_2 free in dark matter haloes with virial temperatures T_{vir} > rsim 10^4 K. MNRAS, 402(2):1249–1262, Feb 2010. doi: 10.1111/j.1365-2966.2009.15960.x.

E. Sirko. Initial Conditions to Cosmological N-Body Simulations, or, How to Run an Ensemble of Simulations. ApJ, 634(2):728–743, Nov. 2005. doi: 10.1086/497090.

J. Smidt, D. J. Whalen, J. L. Johnson, M. Surace, and H. Li. Radiation Hydrodynamical Simulations of the First Quasars. ApJ, 865(2):126, Oct. 2018. doi: 10.3847/1538-4357/aad7b8.

B. Smith and M. Lang. Ytree: Merger-Tree Toolkit. Zenodo, Feb. 2018.

B. D. Smith, J. A. Regan, T. P. Downes, M. L. Norman, B. W. O'Shea, and J. H. Wise. The growth of black holes from Population III remnants in the Renaissance simulations. MNRAS, 480(3):3762–3773, Nov. 2018. doi: 10.1093/mnras/sty2103.

V. V. Sobolev. The Diffusion of Lα Radiation in Nebulae and Stellar Envelopes. Soviet Ast., 1: 678, Oct. 1957.

A. Stacy, V. Bromm, and A. Loeb. Effect of Streaming Motion of Baryons Relative to Dark Matter on the Formation of the First Stars. ApJ, 730(1):L1, Mar 2011. doi: 10.1088/2041-8205/730/1/L1.

S. W. Stahler. The formation of primordial stars. PASP, 98:1081–1087, Nov 1986. doi: 10.1086/131877.

T. P. Stecher and D. A. Williams. Photodestruction of Hydrogen Molecules in H I Regions. ApJ, 149:L29, July 1967. doi: 10.1086/180047.

A. Sternberg, A. Gurman, and S. Bialy. H I-to-H_2 Transitions in Dust-free Interstellar Gas. ApJ, 920(2):83, Oct. 2021. doi: 10.3847/1538-4357/ac167b.

M. Suazo, J. Prieto, A. Escala, and D. R. G. Schleicher. The Role of Gas Fragmentation During the Formation of Supermassive Black Holes. ApJ, 885(2):127, Nov. 2019. doi: 10.3847/1538-4357/ab45eb.

K. Sugimura, K. Omukai, and A. K. Inoue. The critical radiation intensity for direct collapse black hole formation: dependence on the radiation spectral shape. MNRAS, 445(1):544–553, Nov 2014. doi: 10.1093/mnras/stu1778.

M. Surace. *Finding the first quasars at birth*. PhD thesis, University of Portsmouth, July 2020. https://ethos.bl.uk/OrderDetails.do?uin=uk.bl.ethos.813731.

M. Surace, D. J. Whalen, T. Hartwig, E. Zackrisson, S. C. O. Glover, S. Patrick, T. E. Woods, A. Heger, and L. Haemmerlé. On the Detection of Supermassive Primordial Stars. ApJ, 869: L39, Dec. 2018. doi: 10.3847/2041-8213/aaf80d.

M. Surace, E. Zackrisson, D. J. Whalen, T. Hartwig, S. C. O. Glover, T. E. Woods, and A. Heger. On the Detection of Supermassive Primordial Stars. II. Blue Supergiants. *arXiv e-prints*, Mar. 2019.

E. F. Toro. *Riemann Solvers and Numerical Methods for Fluid Dynamics: A Practical Introduction*. Springer Berlin, Heidelberg, 1997. https://doi.org/10.1007/b79761.

E. F. Toro, M. Spruce, and W. Speares. Restoration of the contact surface in the HLL-Riemann solver. *Shock Waves*, 4(1):25–34, July 1994. doi: 10.1007/BF01414629.

J. K. Truelove, R. I. Klein, C. F. McKee, I. Holliman, John H., L. H. Howell, and J. A. Greenough. The Jeans Condition: A New Constraint on Spatial Resolution in Simulations of Isothermal Self-gravitational Hydrodynamics. ApJ, 489(2):L179–L183, Nov. 1997. doi: 10.1086/310975.

D. Tseliakhovich and C. Hirata. Relative velocity of dark matter and baryonic fluids and the formation of the first structures. Phys. Rev. D, 82(8):083520, Oct 2010. doi: 10.1103/PhysRevD.82.083520.

M. J. Turk. *The formation of primordial protostars*. PhD thesis, Stanford University, California, Jan. 2009.

M. J. Turk, T. Abel, and B. O'Shea. The Formation of Population III Binaries from Cosmological Initial Conditions. *Science*, 325(5940):601, July 2009. doi: 10.1126/science.1173540.

M. J. Turk, B. D. Smith, J. S. Oishi, S. Skory, S. W. Skillman, T. Abel, and M. L. Norman. yt: A Multi-code Analysis Toolkit for Astrophysical Simulation Data. *The Astrophysical Journal Supplement Series*, 192:9, Jan. 2011. doi: 10.1088/0067-0049/192/1/9.

H. Umeda, T. Hosokawa, K. Omukai, and N. Yoshida. The Final Fates of Accreting Supermassive Stars. ApJ, 830:L34, Oct. 2016. doi: 10.3847/2041-8205/830/2/L34.

R. Valiante, B. Agarwal, M. Habouzit, and E. Pezzulli. On the Formation of the First Quasars. *Publications of the Astronomical Society of Australia*, 34:e031, July 2017. doi: 10.1017/pasa.2017.25.

A. Vikaeus, E. Zackrisson, D. Schaerer, E. Visbal, E. Fransson, S. Malhotra, J. Rhoads, and M. Sahlén. Conditions for detecting lensed Population III galaxies in blind surveys with the James Webb Space Telescope, the Roman Space Telescope, and Euclid. MNRAS, 512(2): 3030–3044, May 2022. doi: 10.1093/mnras/stac488.

E. Visbal, Z. Haiman, and G. L. Bryan. Direct collapse black hole formation from synchronized pairs of atomic cooling haloes. MNRAS, 445(1):1056–1063, Nov 2014. doi: 10.1093/mnras/stu1794.

F. Wang, J. Yang, X. Fan, J. F. Hennawi, A. J. Barth, E. Banados, F. Bian, K. Boutsia, T. Connor, F. B. Davies, R. Decarli, A.-C. Eilers, E. P. Farina, R. Green, L. Jiang, J.-T. Li, C. Mazzucchelli, R. Nanni, J.-T. Schindler, B. Venemans, F. Walter, X.-B. Wu, and M. Yue. A Luminous Quasar at Redshift 7.642. ApJ, 907(1):L1, Jan. 2021. doi: 10.3847/2041-8213/abd8c6.

A. Weigert, H.-J. Wendker, and L. Wisotzki. *Astronomie und Astrophysik*. WILEY-VCH Verlag GmbH&Co.KGaA, Weinheim, 2010.

Wes McKinney. Data Structures for Statistical Computing in Python. In Stéfan van der Walt and Jarrod Millman, editors, *Proceedings of the 9th Python in Science Conference*, pages 56 – 61, 2010. doi: 10.25080/Majora-92bf1922-00a.

D. Whalen, T. Abel, and M. L. Norman. Radiation Hydrodynamic Evolution of Primordial H II Regions. ApJ, 610:14–22, July 2004. doi: 10.1086/421548.

D. Whalen, B. W. O'Shea, J. Smidt, and M. L. Norman. How the First Stars Regulated Local Star Formation. I. Radiative Feedback. ApJ, 679(2):925–941, Jun 2008. doi: 10.1086/587731.

D. Whalen, R. M. Hueckstaedt, and T. O. McConkie. Radiative and Kinetic Feedback by Low-Mass Primordial Stars. ApJ, 712(1):101–111, Mar 2010. doi: 10.1088/0004-637X/712/1/101.

D. J. Whalen and C. L. Fryer. The Formation of Supermassive Black Holes from Low-mass Pop III Seeds. ApJ, 756:L19, Sept. 2012. doi: 10.1088/2041-8205/756/1/L19.

J. H. Wise and T. Abel. Suppression of H_2 Cooling in the Ultraviolet Background. ApJ, 671(2): 1559–1567, Dec. 2007. doi: 10.1086/522876.

J. H. Wise and T. Abel. ENZO+MORAY: radiation hydrodynamics adaptive mesh refinement simulations with adaptive ray tracing. MNRAS, 414(4):3458–3491, July 2011. doi: 10.1111/j.1365-2966.2011.18646.x.

J. H. Wise, M. J. Turk, and T. Abel. Resolving the Formation of Protogalaxies. II. Central Gravitational Collapse. *The Astrophysical Journal*, 682(2):745–757, Aug 2008. doi: 10.1086/588209.

J. Wolcott-Green, Z. Haiman, and G. L. Bryan. Photodissociation of H_2 in protogalaxies: modelling self-shielding in three-dimensional simulations. MNRAS, 418(2):838–852, Dec. 2011. doi: 10.1111/j.1365-2966.2011.19538.x.

J. Wolcott-Green, Z. Haiman, and G. L. Bryan. Suppression of H_2-cooling in protogalaxies aided by trapped Lyα cooling radiation. MNRAS, 500(1):138–144, Jan. 2021. doi: 10.1093/mnras/staa3057.

T. E. Woods, A. Heger, D. J. Whalen, L. Haemmerlé, and R. S. Klessen. On the Maximum Mass of Accreting Primordial Supermassive Stars. ApJ, 842:L6, June 2017. doi: 10.3847/2041-8213/aa7412.

T.-E. Woods, B. Agarwal, V. Bromm, A. Bunker, K.-J. Chen, S. Chon, A. Ferrara, S.-C.-O. Glover, L. Haemmerle, Z. Haiman, T. Hartwig, A. Heger, S. Hirano, T. Hosokawa, K. Inayoshi, R.-S. Klessen, C. Kobayashi, F. Koliopanos, M.-A. Latif, Y. Li, L. Mayer, M. Mezcua, P. Natarajan, F. Pacucci, M.-J. Rees, J.-A. Regan, Y. Sakurai, S. Salvadori, R. Schneider, M. Surace, T.-L. Tanaka, D.-J. Whalen, and N. Yoshida. Titans of the Early Universe: The Prato Statement on the Origin of the First Supermassive Black Holes. *arXiv e-prints*, Oct. 2018.

T. E. Woods, A. Heger, and L. Haemmerlé. On monolithic supermassive stars. MNRAS, 494(2): 2236–2243, May 2020. doi: 10.1093/mnras/staa763.

T. E. Woods, S. Patrick, J. S. Elford, D. J. Whalen, and A. Heger. On the Evolution of Supermassive Primordial Stars in Cosmological Flows. ApJ, 915(2):110, July 2021. doi: 10.3847/1538-4357/abfaf9.

P. Woodward and P. Colella. The Numerical Stimulation of Two-Dimensional Fluid Flow with Strong Shocks. *Journal of Computational Physics*, 54(1):115–173, Apr. 1984. doi: 10.1016/0021-9991(84)90142-6.

J. Yang, F. Wang, X. Fan, J. F. Hennawi, F. B. Davies, M. Yue, E. Banados, X.-B. Wu, B. Venemans, A. J. Barth, F. Bian, K. Boutsia, R. Decarli, E. P. Farina, R. Green, L. Jiang, J.-T. Li, C. Mazzucchelli, and F. Walter. Pōniuā'ena: A Luminous z = 7.5 Quasar Hosting a 1.5 Billion Solar Mass Black Hole. ApJ, 897(1):L14, July 2020. doi: 10.3847/2041-8213/ab9c26.

N. Yoshida, T. Abel, L. Hernquist, and N. Sugiyama. Simulations of Early Structure Formation: Primordial Gas Clouds. ApJ, 592:645–663, Aug. 2003. doi: 10.1086/375810.

N. Yoshida, S. P. Oh, T. Kitayama, and L. Hernquist. Early Cosmological H II/He III Regions and Their Impact on Second-Generation Star Formation. ApJ, 663(2):687–707, July 2007. doi: 10.1086/518227.

Appendix A

Simulation runs

The following tables, A.1, A.2, A.3, A.4, showcase simulation details for the eight performed runs. Step 1 describes the simulation run starting from the initial parameter file at z=200 and evolves to z=30, where it is stopped and refinement by Jeans-length is manually switched on with *CellFlaggingMethod=2 4 6*. Subsequenlty, in step 2 the simulation runs from z=30 until the onset of atomic cooling which is labeled as t=0.0 and occurs for each halo at a different redshift (see table 4.1). Some simulation parameters are changed at this point, which are

- *dtDataDump = 10* to *0.0013* ,
- *StopFirstTimeAtLevel = 15* to *0* ,
- *ConservativeInterpolation = 1* to *0* ,
- *ParticleSubgridDepositMode = 1* to *0* ,
- *UseMinimumPressureSupport = 0* to *1* ,
- *RiemannSolver = 5* to *4* ,
- *RiemannSolverFallback = 1* to *0* .

Then, in step 3, the simulation is restarted again and proceeds as long as is deemed necessary. Cosmological simulations and especially zoom in simulations, require a certain amount of computational power to run. Therefore simulation were planned to run with 256processors or cores (c; here). However, `SCIAMA` was going through some updates and problems, setting a limit of 5 to 4 nodes (64-100c) per run and otherwise ending in segmentation fault errors. The errors were rather random, occurring more frequently when `SCIAMA` was busy. Another encountered error was a signal 9 kill due to not sufficient memory (halo 8), which was solved by increasing the number of processors. Other than that, simulations proceeded smoothly only requiring resubmitting when processors run out of memory or an inherent calculation yielded a negative value (stop in euler with geslice < 0).
Storage used to be a problem until `lustre2` was installed. The two last rows of the subsequent tables highlight that difficulty, as the runs took up a lot of storage. GB/DD shows the size of a

single directory in GB, whereas the last row displays the total size of the simulation output in TB, culminating in 45.8TB total.

	Halo 1	**Halo 2**
Step 1	01h12m23s (256c)	01h07m16s (256c)
Step 2	18h51m31s (256c)	01d15h27m43s (256c)
Step 3	01d19h36m41s (256c) ⇒ DD0220	11d06h51m03s (256c-352c) ⇒ DD0298
GB/DD	20	22-24
Size (TB)	4.3	6.8

Table A.1: Simulation details for halo 1 and halo 2, where c stands for 'cores' and if not otherwise specified calculations are done on `SCIAMA2`. The last two rows display the size of a single directory (DD) in GB and the total size of the simulation output in TB.

	Halo 8	**Halo 10**
Step 1	04h38m17s (256c)	02h07m36s (64c)
Step 2	18h07m40s (256c)	01d02h13m17s (64c)
Step 3	12d12h00m00s (256c) ⇒ DD0208	07d02h36m08s (64c) ⇒ DD0386
	11d22h50m37s (352c) ⇒ DD0226	03d15h28m26s (64c) ⇒ DD0467
	12d12h00m00s (480c) ⇒ DD0230	
GB/DD	13	16-17
Size (TB)	2.9	7.5

Table A.2: Simulation details for halo 8 and halo 10, where c stands for 'cores' and if not otherwise specified calculations are done on `SCIAMA2`. The last two rows display the size of a single directory (DD) in GB and the total size of the simulation output in TB.

	Halo 12	**Halo 16**
Step 1	01h34m22s (64c)	02h36m07s (64c)
Step 2	23h28m40s (64c)	01d05h27m27s (64c)
Step 3	06d03h50m46s (64c) ⇒ DD0232	06d16h00m00s (64c) ⇒ DD0309
	02d11h22m51s (64c) ⇒ DD0274	03d16h23m29s (64c) ⇒ DD0377
	03d08h54m38s (64c) ⇒ DD0317	
GB/DD	15-16	16-17
Size (TB)	4.8	5.9

Table A.3: Simulation details for halo 12 and halo 16, where c stands for ’cores’ and if not otherwise specified calculations are done on `SCIAMA2`. The last two rows display the size of a single directory (DD) in GB and the total size of the simulation output in TB.

	Halo 19	**Halo 20**
Step 1	01h13m05s (100c sciama3)	01h46m43s (100c sciama3)
Step 2	01d11h41m55s (80c)	01d11h33m25s (80c)
Step 3	06d00h57m29s (80c) ⇒ DD0332	06d00h30m33s (80c) ⇒ DD0191
	05d00h09m06s (80c) ⇒ DD0356	05d00h27m56s (80c) ⇒ DD0240
		12d12h00m09s (128c) ⇒ DD0294
		05d15h49m59s (320c sciama3)
		⇒ DD0324
GB/DD	18-19	22-23
Size (TB)	6.4	7.2

Table A.4: Simulation details for halo 19 and halo 20, where c stands for ’cores’ and if not otherwise specified calculations are done on `SCIAMA2`. The last two rows display the size of a single directory (DD) in GB and the total size of the simulation output in TB.

Appendix B

H2 Evolution

For consistency, the following figures display the calculated H_2 and HII accretion rates, H_2 and HII total accumulated masses, as well as the 1D H_2-fraction profile plots. They offer a good sanity check in comparison to the graphs throughout the main part of this thesis and highlight the formation of molecular hydrogen with time in an otherwise atomically cooled halo. Those results are in agreement with the main findings.

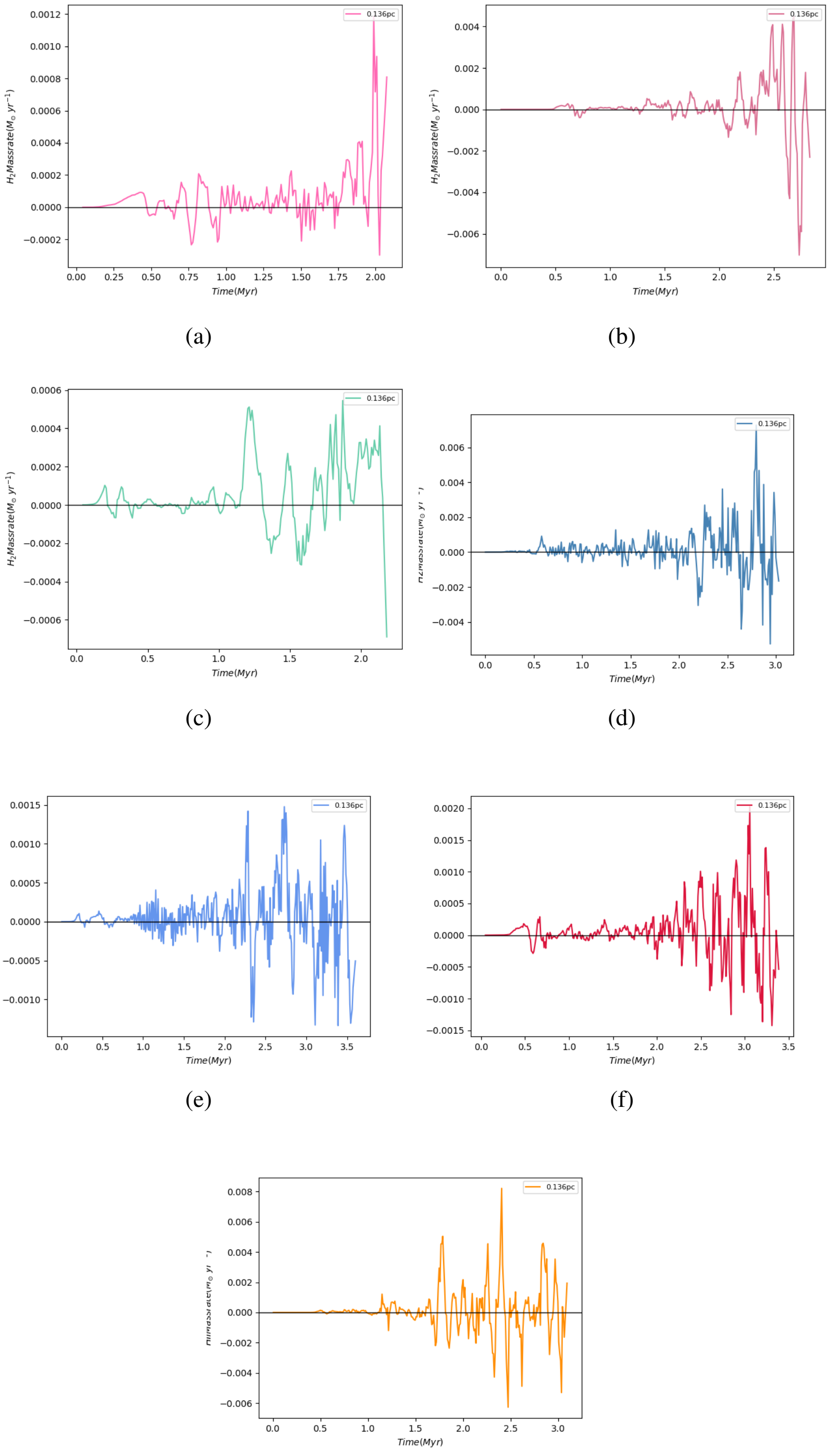

(a) (b)

(c) (d)

(e) (f)

(g)

Figure B.1: H_2 accretion rates for all simulated haloes in a $10^5 J_{21}$ LW background. Rates are calculated with regard to the center of the main disk, displaying halo 1 in (a), halo 2 in (b), halo 8 in (c), halo 12 in (d), halo 16 in (e), halo 19 in (f), and halo 20 in (g).

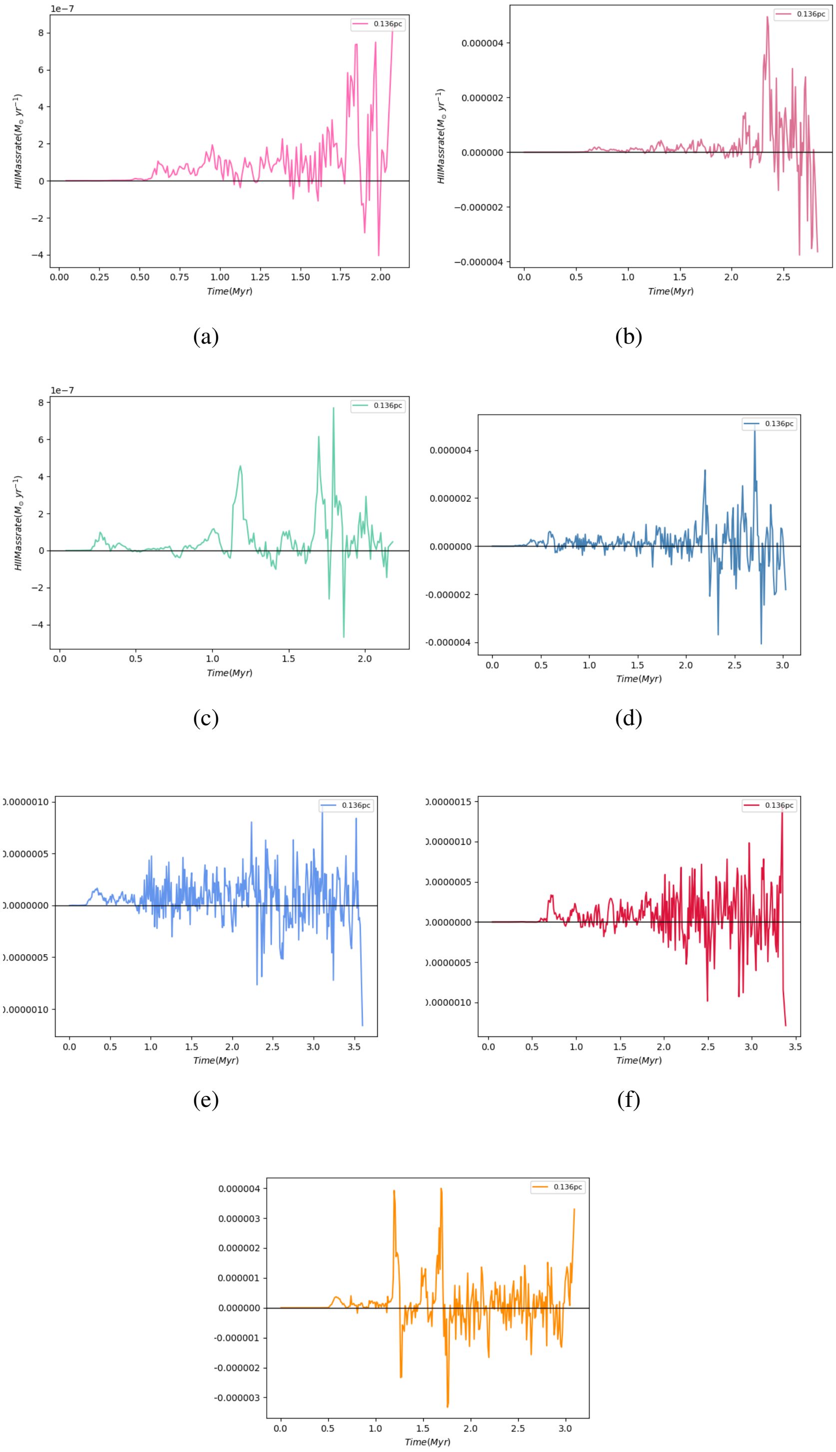

(a) (b)

(c) (d)

(e) (f)

(g)

Figure B.2: *HII* accretion rates for all simulated haloes in a $10^5 J_{21}$ LW background. Rates are calculated with regard to the center of the main disk, displaying halo 1 in (a), halo 2 in (b), halo 8 in (c), halo 12 in (d), halo 16 in (e), halo 19 in (f), and halo 20 in (g).

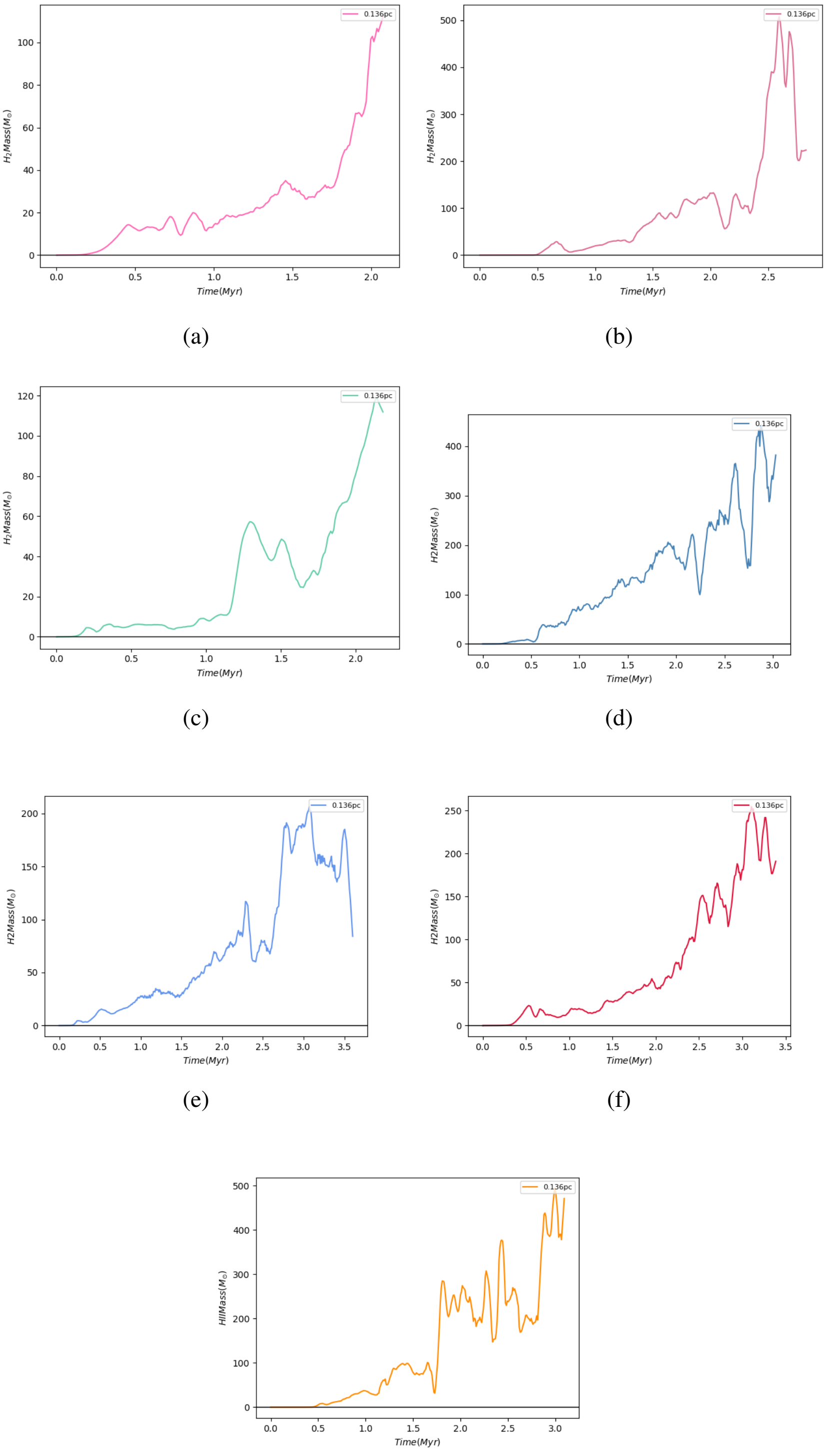

(a) (b) (c) (d) (e) (f) (g)

Figure B.3: H_2 accumulated masses for all simulated haloes in a $10^5 J_{21}$ LW background. Masses are calculated with regard to the center of the main disk (0.136 pc), displaying halo 1 in (a), halo 2 in (b), halo 8 in (c), halo 12 in (d), halo 16 in (e), halo 19 in (f), and halo 20 in (g).

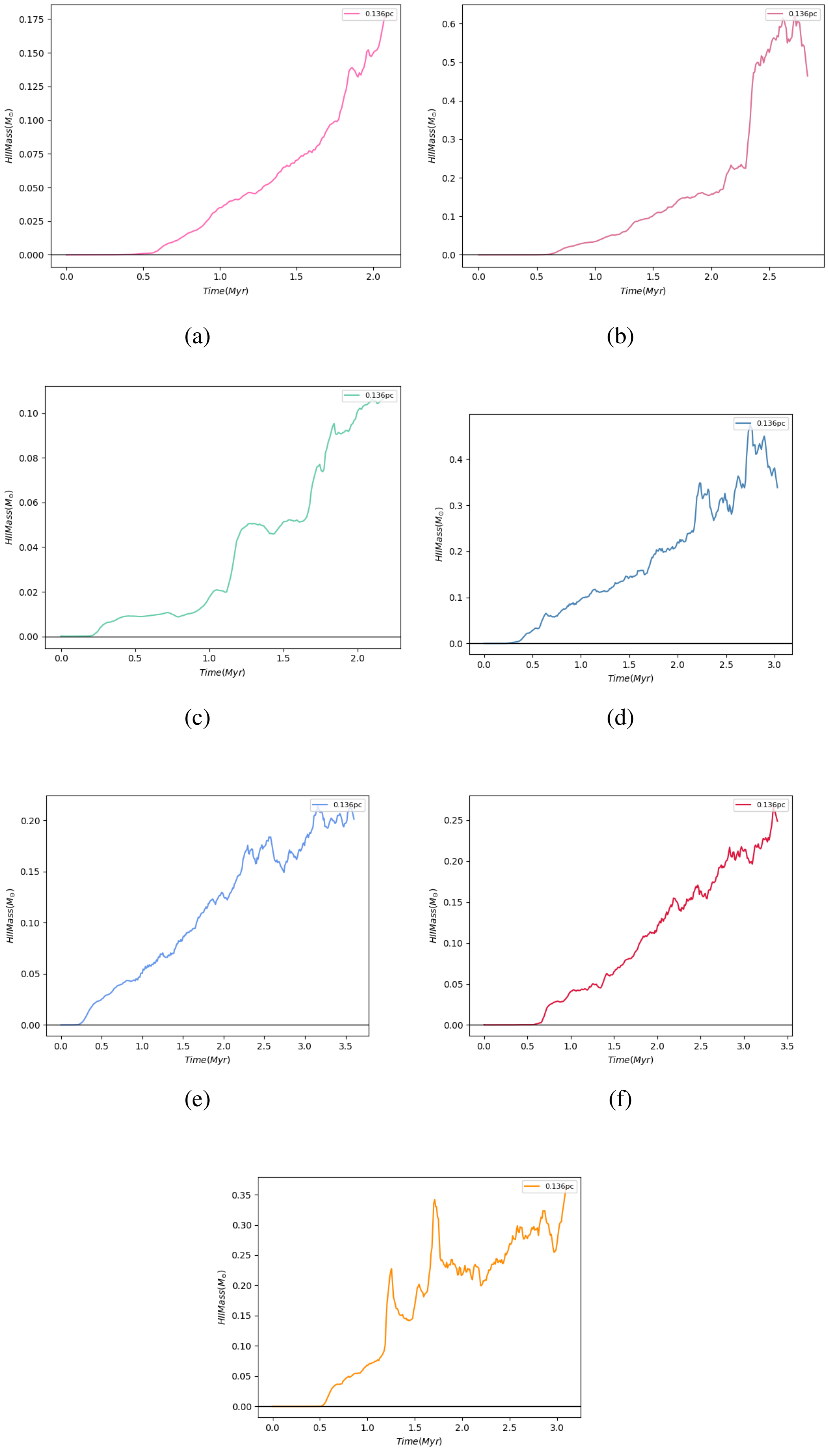

(a)

(b)

(c)

(d)

(e)

(f)

(g)

Figure B.4: *HII* accumulated masses for all simulated haloes in a $10^5 J_{21}$ LW background. Masses are calculated with regard to the center of the main disk (0.136 pc), displaying halo 1 in (a), halo 2 in (b), halo 8 in (c), halo 12 in (d), halo 16 in (e), halo 19 in (f), and halo 20 in (g).

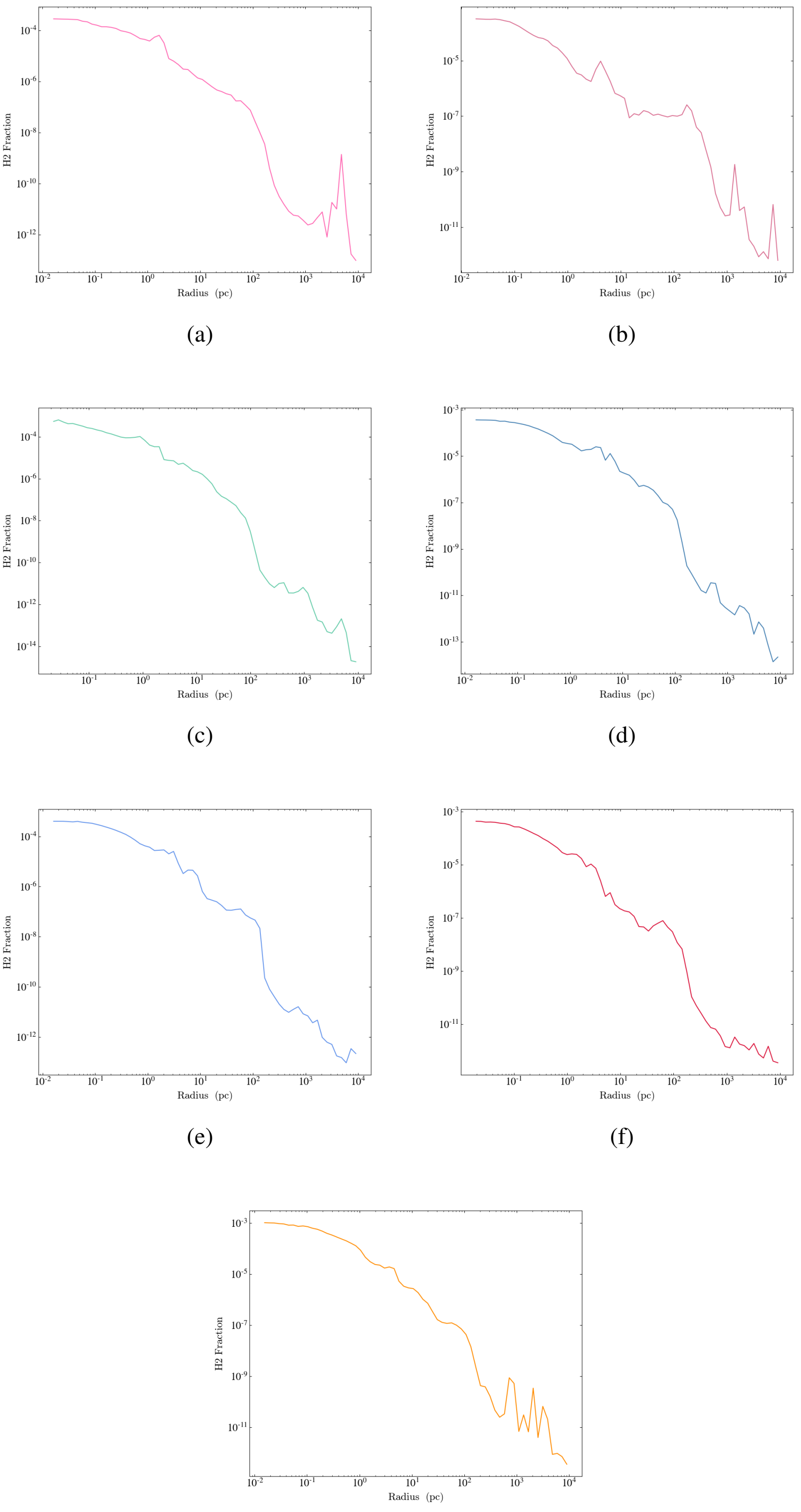

(a) (b)

(c) (d)

(e) (f)

(g)

Figure B.5: 1-D H_2-fraction against radius profiles at the beginning (t=0.0) of catastrophic baryon collapse for the simulated haloes 1, 2, 8, 12, 16, 19, and 20 displayed in subfigures (a), (b), (c), (d), (e), (f), and (g) respectively.

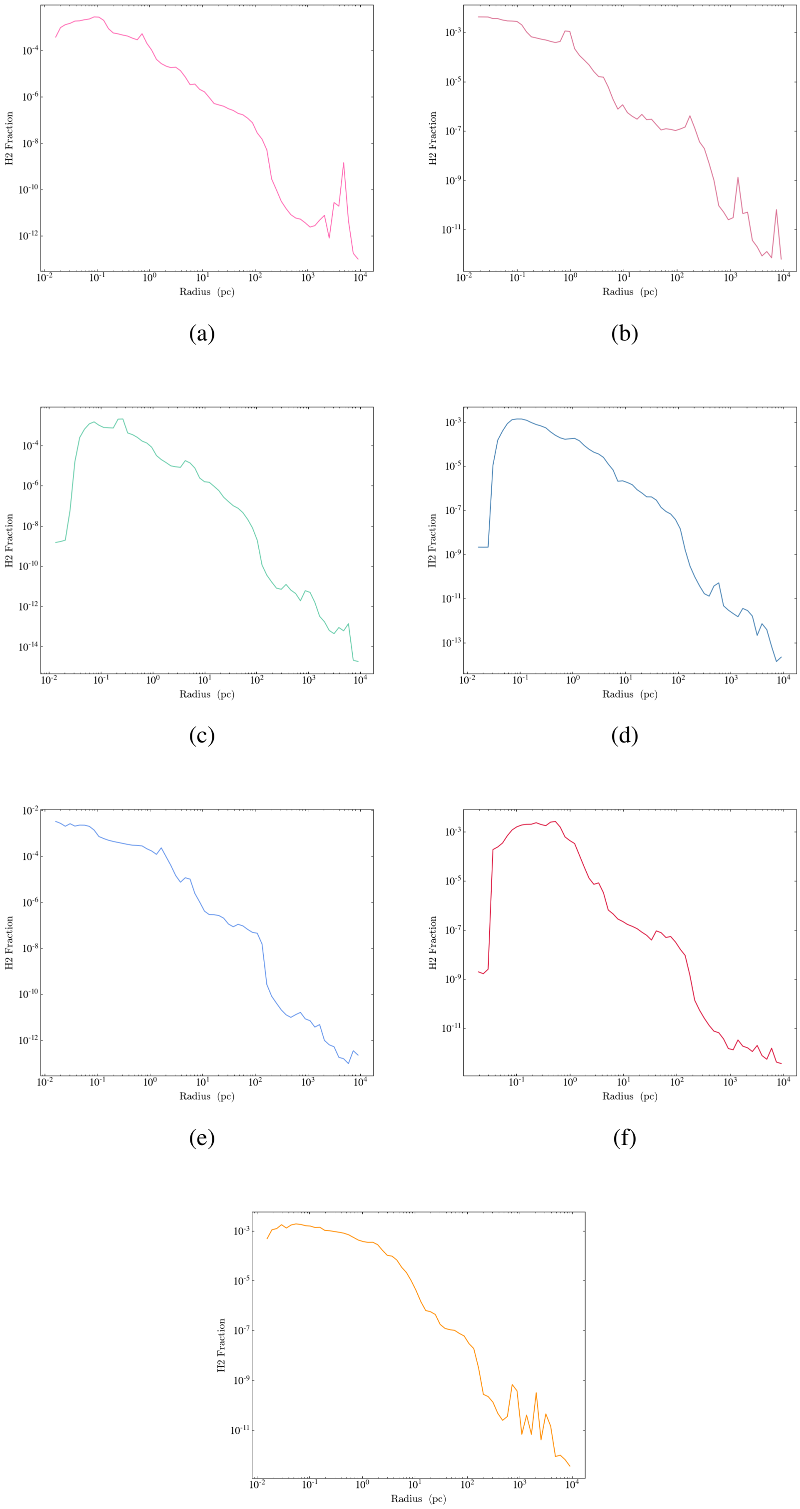

(a)

(b)

(c)

(d)

(e)

(f)

(g)

Figure B.6: 1-D H_2-fraction against radius profiles for the time when central atomic cooling is triggered. We showcase the simulated haloes 1, 2, 8, 12, 16, 19, and 20 in subfigures (a), (b), (c), (d), (e), (f), and (g) respectively.

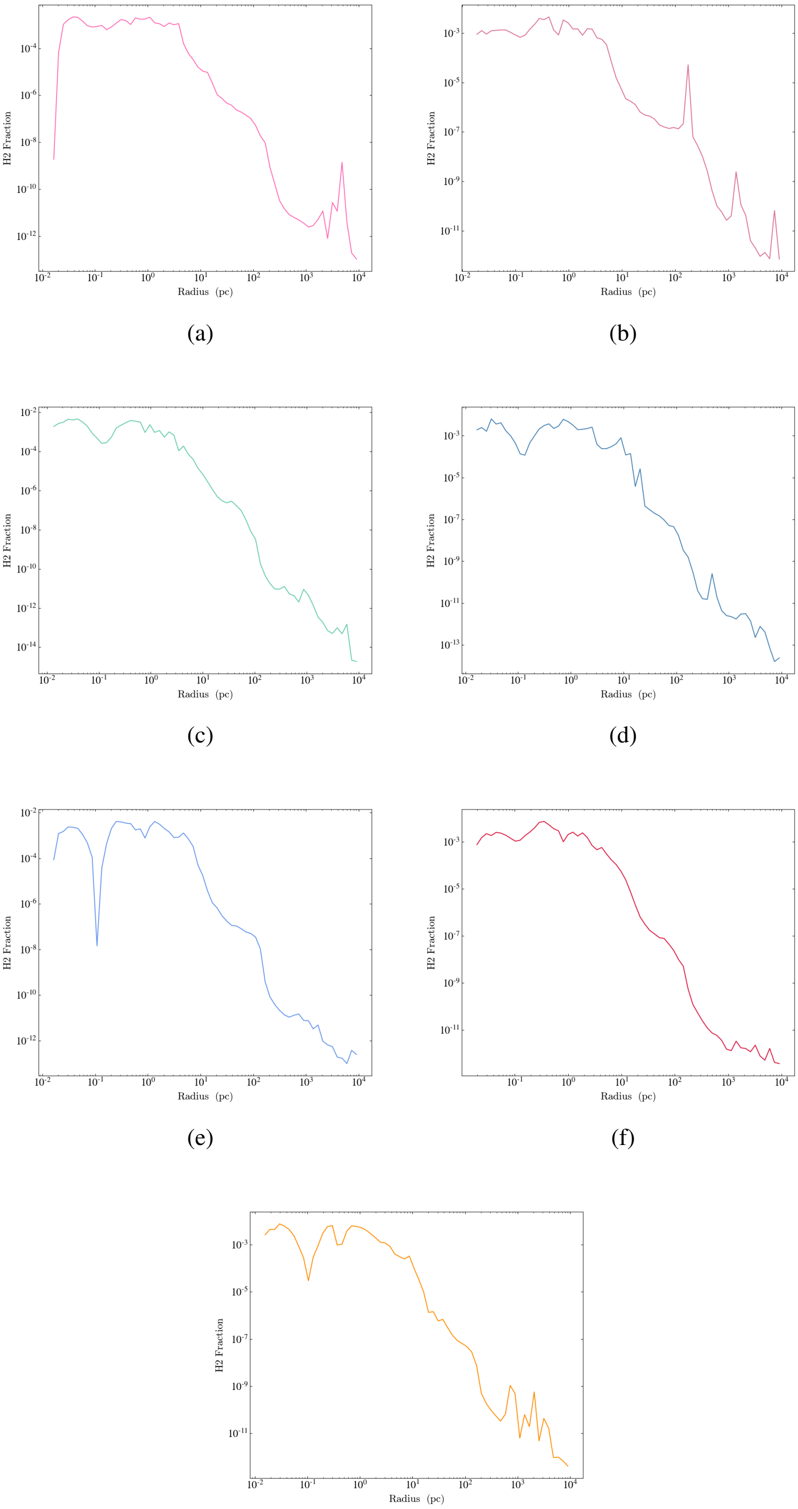

(a) (b) (c) (d) (e) (f) (g)

Figure B.7: 1-D H_2-fraction against radius profiles at the end of each simulation. Simulated haloes 1, 2, 8, 12, 16, 19, and 20 are displayed in subfigures (a), (b), (c), (d), (e), (f), and (g) respectively.

Appendix C

Additional pictures

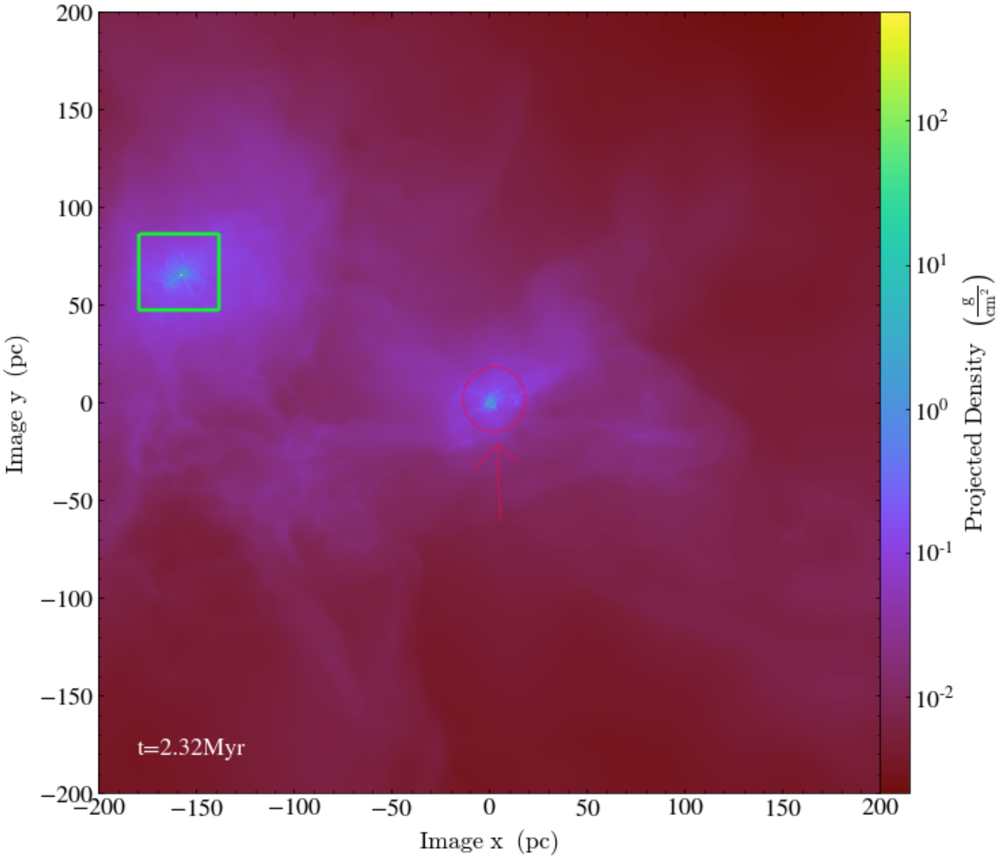

Figure C.1: Halo 2 in the middle of a 400pc diameter box, marked with a red circle and arrow, next to its neighbour, green square, at ~200pc distance and a timestep of 2.32Myr.

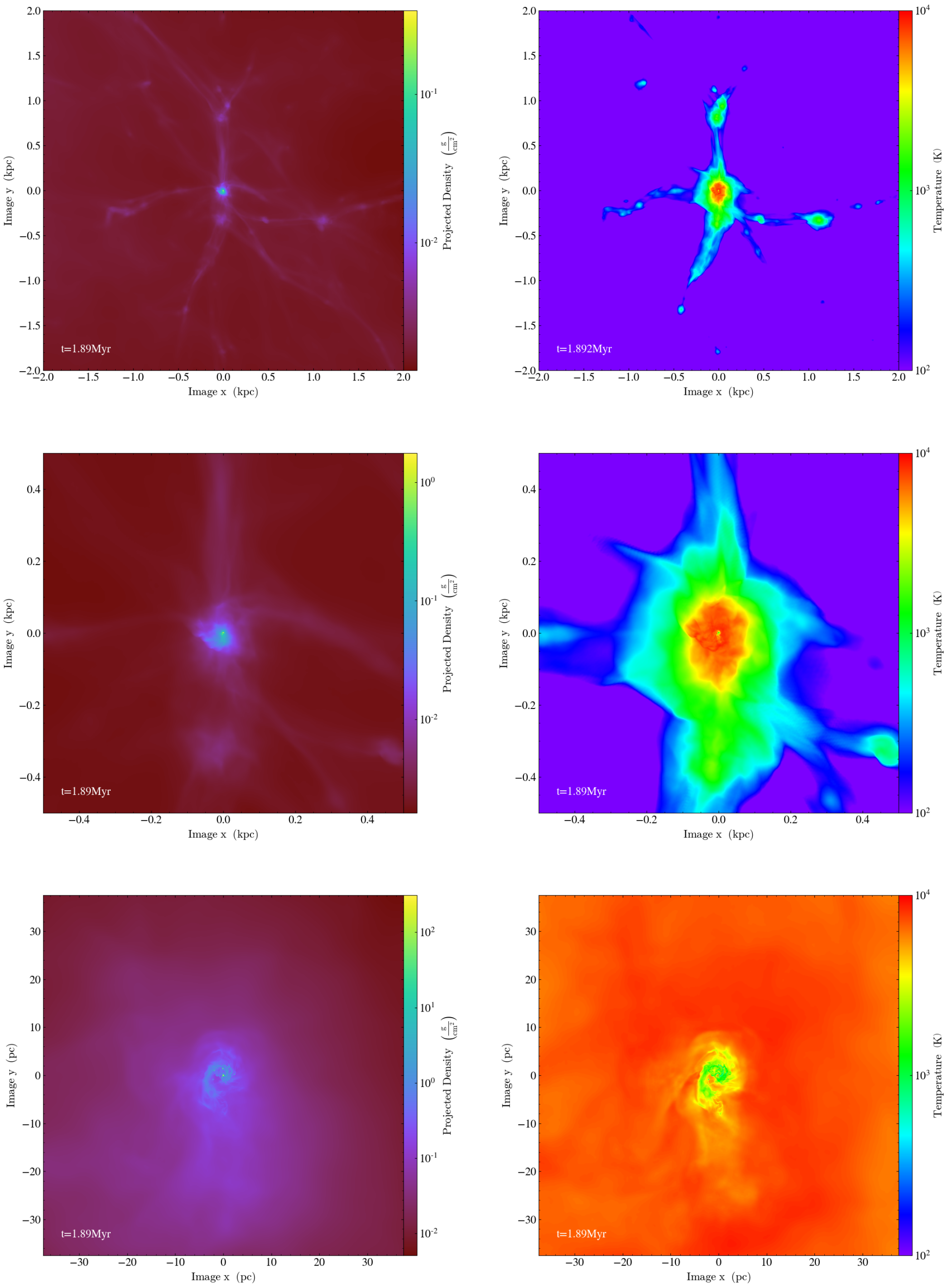

Figure C.2: For the interested reader, density(left column) and temperature(right column) snapshots of halo 8 at 1.89Myr in different scales. From top to bottom: in a 4kpc diameter box, 1kpc in diameter, and 75pc in diamter.

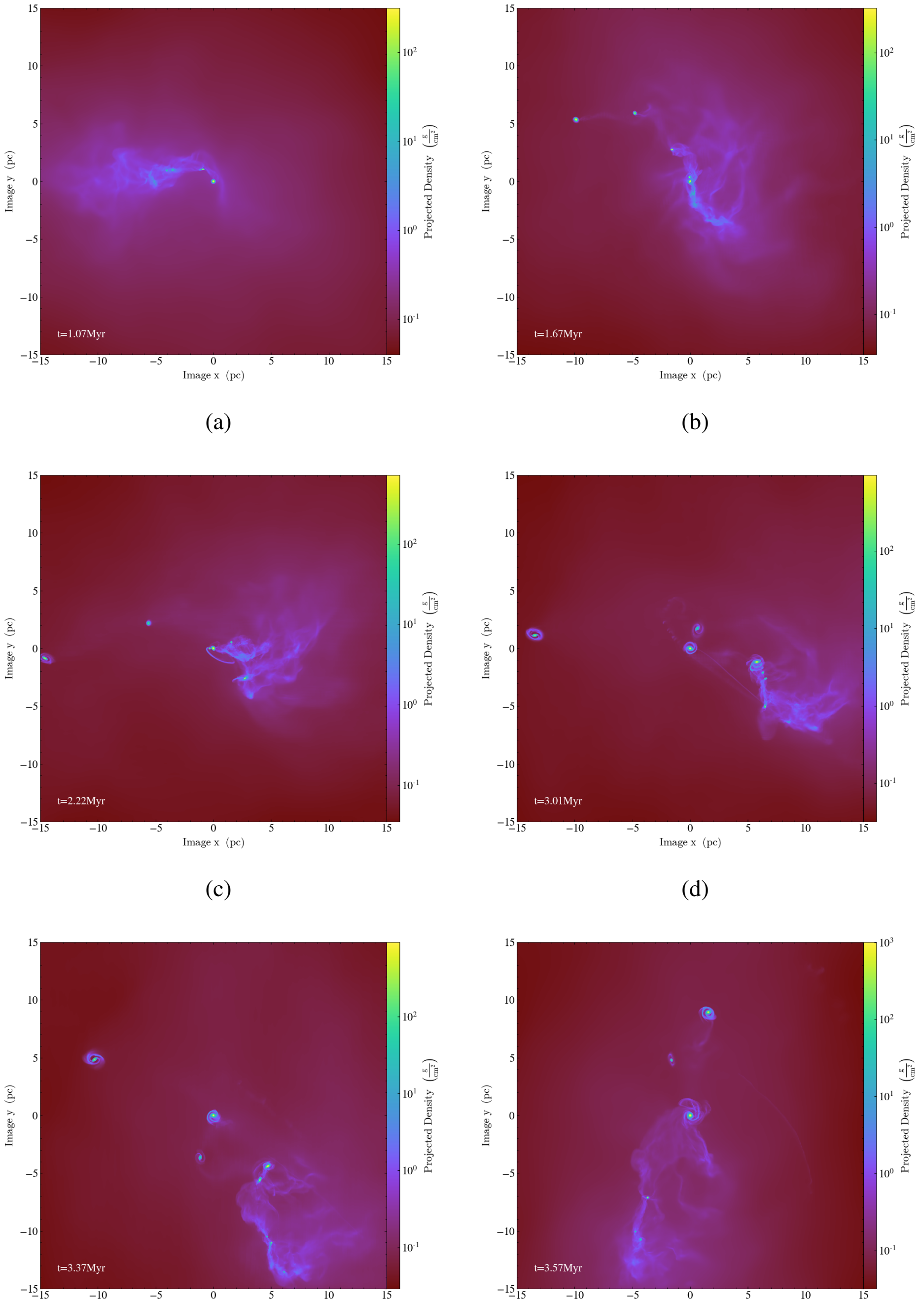

(a) (b)

(c) (d)

(e) (f)

Figure C.3: Multiple dense objects forming in the center of halo 10 displayed in 30pc boxes and at various timesteps. They dispaly the halo through its evolution at t=1.07Myr in (a), at t=1.67Myr in (b), t=2.22Myr in (c), t=3.01Myr in (d), t=3.37Myr in (e), and at t=3.57Myr in (f).

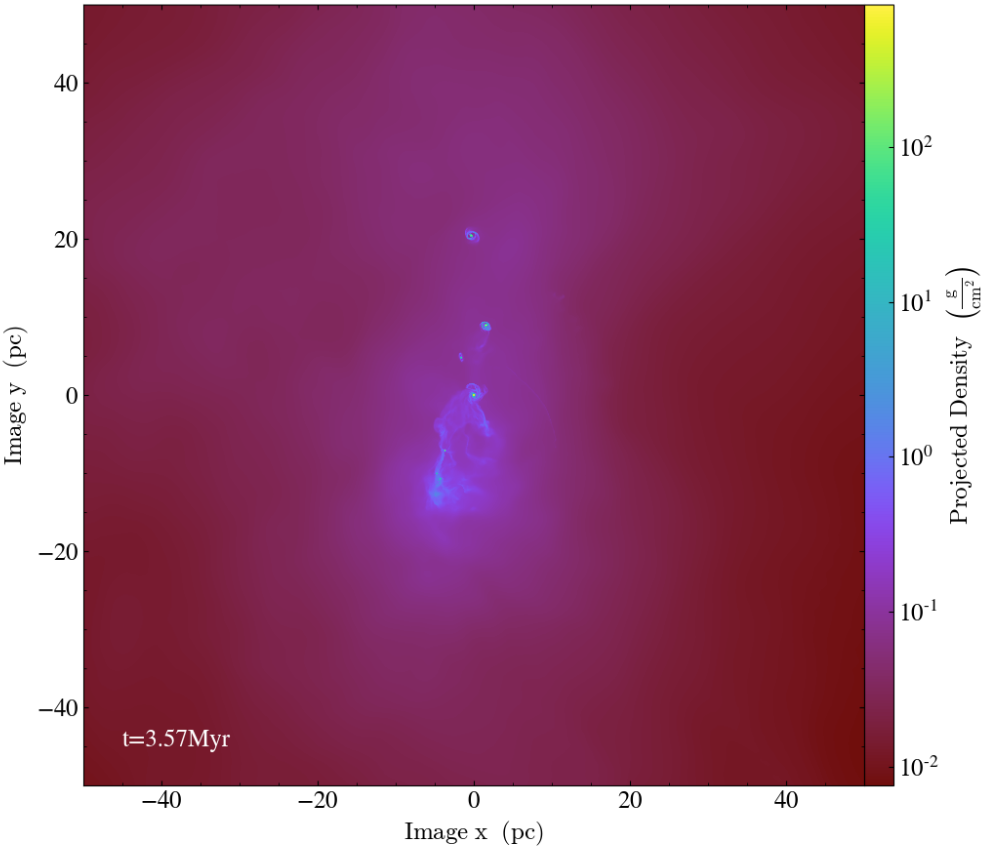

Figure C.4: Multiple dense objects in halo 10 displayed as a 100pc box at an evolution timestep of t=3.57Myr.